

**Ag AND MCM-41 DOPED TiO<sub>2</sub> THIN FILM AND ITS APPLICATIONS  
TO INDOOR AIR TREATMENT**

**MS. WARAPORN TONGON  
ID: 51920113**

**A THESIS SUBMITTED AS A PART OF THE REQUIREMENTS  
FOR THE DEGREE OF DOCTOR OF PHILOSOPHY  
IN ENVIRONMENTAL TECHNOLOGY**

**THE JOINT GRADUATE SCHOOL OF ENERGY AND ENVIRONMENT  
AT KING MONGKUT'S UNIVERSITY OF TECHNOLOGY THONBURI**

**2<sup>ND</sup> SEMESTER 2013**

**COPYRIGHT OF THE JOINT GRADUATE SCHOOL OF ENERGY AND ENVIRONMENT**

Ag and MCM-41 Doped TiO<sub>2</sub> Thin Film and Its Applications to Indoor Air Treatment


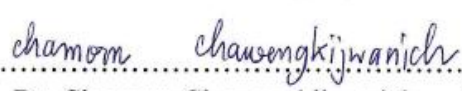


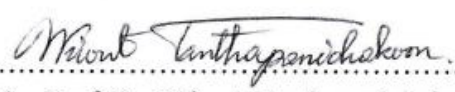
Ms. Waraporn Tongon  
ID: 51920113

A Thesis Submitted as a Part of the Requirements  
for the Degree of Doctor of Philosophy  
in Environmental Technology

The Joint Graduate School of Energy and Environment  
at King Mongkut's University of Technology Thonburi

2<sup>nd</sup> Semester 2013

Thesis Committee

 ..... ( Asst. Prof. Dr. Siriluk Chiarakorn )	Advisor
 ..... ( Dr. Chamorn Chawengkijwanich )	Co-Advisor
 ..... ( Assoc. Prof. Dr. Navadol Laosiripojana )	Member
 ..... ( Asst. Prof. Dr. Wandee Onreabroy )	Member
 ..... ( Prof. Dr. Wiwut Tanthapanichakoon )	External Examiner

**Thesis Title:** Ag and MCM-41 Doped TiO<sub>2</sub> Thin Film and Its Applications to Indoor Air Treatment

**Student's name, organization and telephone/fax numbers/email**

Ms. Waraporn Tongon

The Joint Graduate School of Energy and Environment (JGSEE)

King Mongkut's University of Technology Thonburi (KMUTT)

126 Pracha Uthit Rd., Bangmod, Tungkru, Bangkok 10140 Thailand

Telephone: 0814-3883-04

E-Mail: [nanwaraporn@gmail.com](mailto:nanwaraporn@gmail.com)

**Supervisor's name, organization and telephone/fax numbers/email**

Asst. Prof. Dr. Siriluk Chiarakorn

Division of Environmental Technology, School of Energy, Environments and Materials

King Mongkut's University of Technology Thonburi (KMUTT)

126 Pracha Uthit Rd., Bangmod, Tungkru, Bangkok 10140 Thailand

Telephone: 02-470-8654

E-Mail: [siriluk.chi@kmutt.ac.th](mailto:siriluk.chi@kmutt.ac.th)

**Topic:** Ag and MCM-41 Doped TiO<sub>2</sub> Thin Film and Its Applications to Indoor Air Treatment

**Name of Student:** Waraporn Tongon

**Name of Supervisor:** Asst. Prof. Dr. Siriluk Chiarakorn

## **ABSTRACT**

Silver doped TiO<sub>2</sub> was incorporated into as-synthesized MCM-41 via a microwave assisted sol-gel technique and coated on a glass substrate. The characterization results displayed high adsorbability and photocatalytic reactivity of the Ag/TiO<sub>2</sub>/MCM-41 nanocomposite film. Results from UV-visible spectroscopy revealed a significant increase in both UV and visible light absorption when Ag and MCM-41 were incorporated in TiO<sub>2</sub> film. The water contact angle measurements showed that the surface of the nanocomposite film exhibited a superhydrophilicity which is a desirable property for self-cleaning application. The performance of the photocatalyst films was tested by photocatalytic decolorization of MB dye, under UV and visible light irradiation. The kinetic rate constants were arranged in the order of Ag/Ti/Si (0.1/1/2) > Ag/Ti/Si (0.1/1/1) > Ag/Ti/Si (0.1/1/0.5) > Ag/Ti/Si (0.1/1/0) > TiO<sub>2</sub>. The application of the Ag/TiO<sub>2</sub>/MCM-41 nanocomposite film for gaseous benzene treatment was carried out in the simulated indoor air system. The kinetic reaction of all photocatalyst films fit well with pseudo first-order model. The photodegradation efficiencies of gaseous benzene under visible light irradiation were arranged in the order of Ag/Ti/Si (0.1/1/2) (55%) > Ag/Ti/Si (0.1/1/0) (28%) > TiO<sub>2</sub> (15%). Under UV and visible light irradiation, the kinetic rate constants on photodegradation of gaseous benzene by Ag/Ti/Si (0.1/1/2) films were 0.263 h<sup>-1</sup> and 0.135 h<sup>-1</sup>, respectively. The antimicrobial activity of the Ag/Ti/Si (0.1/1/2) film against gram-negative *E. coli* was evaluated under visible light irradiation. The percentage reduction of viable *E. coli* (%R) on Ag/Ti/Si (0.1/1/2) film was approximately up to 98% within 2 h.

**Keywords:** Ag/TiO<sub>2</sub>/MCM-41; microwave, nanocomposite film; benzene; antimicrobial, indoor air

## **ACKNOWLEDGEMENTS**

This work was financially supported by the Center for Energy Technology and Environment, and the Ministry of Education, Thailand. The author would like to express her gratitude to the Thailand Graduate Institute of Science and Technology (TGIST) scholarship TGIST 01-53-019, Petchra Pra Jom Klao Scholarship of King Mongkut's University of Technology Thonburi (KMUTT), the Nanotechnology Center (NANOTEC), the National Science and Technology Development Agency (NSTDA), Ministry of Science and Technology, Thailand through its program of the Center of Excellence Network. Finally, I would like to thank my parents for supporting me and encouraging me with their best wishes.

## CONTENTS

CHAPTER	TITLE	PAGE
	ABSTRACT	i
	ACKNOWLEDGEMENT	ii
	CONTENTS	iii
	LIST OF TABLES	vii
	LIST OF FIGURES	viii
	NOMENCLATURES	xii
1	INTRODUCTION	
	1.1 Rotational/problem statement	1
	1.2 Literature reviews	4
	1.2.1 Preparation of photocatalyst	4
	1.2.2 Environmental applications of photocatalyst	6
	1.3 Research objectives	7
	1.4 Scope of work	7
2	THEORIES	
	2.1 Indoor air pollution (IAQ)	8
	2.1.1 Sources of indoor air pollution	9
	2.1.2 Effects of indoor air pollutants on human health	11
	2.1.3 Indoor air treatment	12
	2.2 Photocatalysis	14
	2.2.1 Mechanism of photocatalyst	14
	2.2.2 Titanium dioxide	16
	2.2.3 Silver doped titanium dioxide	18
	2.2.4 Photocatalytic oxidation	22
	2.3 Thin film deposition technique	24
	2.3.1 Physical vapor deposition (PVD)	24
	2.3.2 Chemical vapor deposition (CVD)	25
	2.4 Synthesis of TiO <sub>2</sub> by microwave assisted sol-gel technique	26
	2.5 Mesoporous molecular sieve MCM-41	28

## CONTENTS (Cont')

CHAPTER	TITLE	PAGE
	2.5.1 History of MCM-41	29
	2.5.2 Characterizations of MCM-41	30
	2.6 Crystal size	32
	2.7 Adsorption	33
	2.7.1 Adsorption mechanisms	33
	2.7.2 Type of adsorption isotherms	34
	2.8 Contact angle and wetting property	36
3	METHODOLOGY	
	3.1 Materials and instruments	39
	3.1.1 Rice husk	39
	3.1.2 Glass slide plates	39
	3.1.3 Lamps	39
	3.1.4 <i>Escherichia coli</i>	39
	3.1.5 Chemical agents	40
	3.1.6 Apparatuses	40
	3.1.7 Analytical instruments	40
	3.2 Experimental procedures	42
	3.2.1 Preparation of extracted silica	43
	3.2.2 Preparation of MCM-41	43
	3.2.3 Preparation of TiO <sub>2</sub> /MCM-41	43
	3.2.4 Preparation of Ag doped TiO <sub>2</sub>	45
	3.2.5 Preparation of Ag/TiO <sub>2</sub> /MCM-41	45
	3.2.6 Characterizations	46
	3.2.7 Photocatalytic treatment of benzene	48
	3.2.8 Antibacterial activity	51
4	PREPARATION OF TiO <sub>2</sub> /MCM-41 NANOCOMPOSITE POWDER BY MICROWAVE-ASSISTED SOL-GEL TECHNIQUE	
	4.1 Introduction	53
	4.2 Research objectives	54

## CONTENTS (Cont')

CHAPTER	TITLE	PAGE
	4.3 Experimental procedure	54
	4.3.1 Preparation of TiO <sub>2</sub> /MCM-41 from rice husk	54
	4.3.2 Characterizations	56
	4.3.3 Photocatalytic measurement of TiO <sub>2</sub> /MCM-41	57
	4.4 Results and discussion	57
	4.4.1 TiO <sub>2</sub> /MCM-41 characterizations	57
	4.4.2 Photocatalytic testing of TiO <sub>2</sub> /MCM-41	69
	4.5 Conclusions	70
5	PREPARATION OF Ag/TiO <sub>2</sub> /MCM-41 NANOCOMPOSITE POWDER AND FILM BY MICROWAVE ASSISTED SOL-GEL TECHNIQUE	
	5.1 Introduction	72
	5.2 Research objectives	72
	5.3 Experimental procedure	73
	5.3.1 Preparation of Ag/TiO <sub>2</sub> /MCM-41 nanocomposite films	73
	5.3.2 Characterizations	73
	5.3.3 Photocatalytic measurements	74
	5.4 Results and discussion	75
	5.4.1 Crystallinity	75
	5.4.2 Porosity	80
	5.4.3 UV/Vis/DR	81
	5.4.4 Morphology and surface structure	83
	5.4.5 Chemical composition and state	88
	5.4.6 Hydrophilic property of the nanocomposite films	92
	5.4.7 Photocatalytic testing of nanocomposite films	93
	5.5 Conclusions	98



## CONTENTS (Cont')

CHAPTER	TITLE	PAGE
6	PHOTOCATALYTIC ACTIVITY OF Ag/TiO <sub>2</sub> /MCM-41 NANOCOMPOSITE FILMS TO INDOOR AIR TREATMENT	
6.1	Introduction	99
6.2	Research objectives	99
6.3	Experimental procedure	99
6.3.1	Benzene gas treatment in batch system	99
6.3.2	Photocatalytic measurement of benzene gas in simulated indoor air system	100
6.3.3	Antibacterial activity measurement	100
6.4	Results and discussion	101
6.4.1	Photodegradation of benzene in batch system	101
6.4.2	Photodegradation of benzene in simulated indoor air process	103
6.4.3	Antimicrobial activity	108
6.5	Conclusions	109
7	CONCLUSIONS AND RECOMMENDATIONS FOR FUTURE WORKS	
7.1	Conclusions	111
7.1.1	Visible-light responsive Ag/TiO <sub>2</sub> /MCM-41 nanocomposite films	111
7.1.2	Environmental applications of Ag/TiO <sub>2</sub> /MCM-41 nanocomposite films	111
7.2	Recommendations	112
	REFERENCES	113
	APPENDIXES	124
	APPENDIX A	125
	APPENDIX B	127
	APPENDIX C	128

## LIST OF TABLES

<b>TABLE</b>	<b>TITLE</b>	<b>PAGE</b>
2.1	Summary of indoor air quality guidelines for selected pollutants	8
2.2	VOCs in ambient air standards of Thailand determined from continuous 24 hour sampling	10
2.3	Current and emerging indoor air treatment methods	13
2.4	Characteristics of TiO <sub>2</sub> crystal structure	17
4.1	Chemical composition of B sample analyzed from EDX	59
4.2	Chemical composition (% atom) of S-100W sample analyzed from EDX	62
4.3	Porosity of TiO <sub>2</sub> , B, S and MCM-41 studied from BET analysis	65
4.4	Band gap energy of photocatalysts	69
5.1	BET analysis of porosity of MCM-41, TiO <sub>2</sub> and Ag/TiO <sub>2</sub> /MCM-41 powders with various Ag and Si molar ratio	81
5.2	Reaction rate constants ( $k$ ) and the coefficient of determination ( $R^2$ ) of all photocatalyst films under UV and visible light irradiation	96
6.1	Kinetic parameters determined from the pseudo-first-order models of gaseous benzene photodegradation by different photocatalyst films under UV and visible light irradiation.	108
6.2	Results of antibacterial testing for <i>E. coli</i> reduction by different photocatalytic films after incubated with fluorescent light for 2 h	109
B-1	Summary of the contact angle measurement on TiO <sub>2</sub> , Ag/Ti/Si (0.1/1/0) and Ag/Ti/Si (0.1/1/2) photocatalyst films	126

## LIST OF FIGURES

FIGURES	TITLE	PAGE
2.1	Primary mechanism of photocatalytic reaction	15
2.2	Bulk structures of rutile and anatase	16
2.3	Photocatalytic pathways for the RB photodegradation on Ag-TiO <sub>2</sub> particles under (A) visible and (B) UV irradiation	20
2.4	FESEM of <i>E. coli</i> before (A) and after (B) being damage on the mesoporous Ag doped TiO <sub>2</sub> film	22
2.5	Elemental mass transfer process involved in the photocatalytic oxidation of VOCs with a catalyst	23
2.6	Thin film preparation by sol-gel method	27
2.7	Mechanistic pathway of MCM-41: (1) liquid crystal phase, (2) silicate anion	30
2.8	Surface analysis of MCM-41 for XRD pattern	30
2.9	Proposed structure of spherical MCM-41	31
2.10	Adsorption isotherm types defined by Brunauer	34
2.11	The first four types of hysteresis	36
2.12	Contact angles formed by sessile liquid drops on a solid surface	37
3.1	Experimental diagram	42
3.2	Schematic diagram of the batch reactor	49
3.3	Schematic diagram of the simulated indoor air system	51
3.4	Schematic diagram of antibacterial testing on photocatalyst films using modified method from JIS Z 2801: 2000 standard	52
4.1	Schematic representation of TiO <sub>2</sub> /MCM-41 prepared by batch method (B)	55
4.2	Schematic diagram of TiO <sub>2</sub> /MCM-41 prepared by sequence method (S)	56
4.3	XRD patterns of TiO <sub>2</sub> /MCM-41 synthesized by batch (B) method with the different heating process: hydrothermal reflux and microwave irradiation	58

### LIST OF FIGURES (Cont')

FIGURES	TITLE	PAGE
4.4	(a) TEM image (magnification $\times 40,000$ ) and (b) SEM-EDS image of Na cubic particles on B-100W sample	58
4.5	XRD patterns of $\text{TiO}_2/\text{MCM-41}$ nanoparticles synthesized by S method with different heating processes	60
4.6	XRD patterns of different photocatalysts prepared by microwave technique	61
4.7	SEM image of S-100W sample	62
4.8	TEM images of $\text{TiO}_2$ , B-100W and S-100W samples with magnification $\times 40,000$ and $\times 300,000$	63
4.9	Nitrogen adsorption-desorption isotherm of $\text{TiO}_2$ , B-100W, S-100W and MCM-41	65
4.10	FTIR spectra of $\text{TiO}_2$ , B-100W, S-100W and MCM-41	67
4.11	UV-visible diffuse reflectance spectra of $\text{TiO}_2$ , B-100W and S-100W samples	68
4.12	MB decolorization of MB dye by $\text{TiO}_2$ , B-100W, S-100W and MCM-41 under UV light irradiation	70
5.1	XRD patterns of $\text{TiO}_2$ and $\text{Ag}/\text{TiO}_2/\text{MCM-41}$ powder samples with various Ag content	76
5.2	XRD patterns of $\text{TiO}_2$ and nanocomposite $\text{Ag}/\text{TiO}_2/\text{MCM-41}$ powder samples with various Si content	77
5.3	Effect of calcination temperatures on crystallinity of $\text{Ag}/\text{Ti}/\text{Si}$ (0.1/1/2) powder	78
5.4	XRD patterns of photocatalyst films	79
5.5	Diffuse reflectance UV-visible absorption spectra of (a) MCM-41, (b) P25, (c) $\text{TiO}_2$ , (d) $\text{Ag}/\text{Ti}/\text{Si}$ (0.1/1/2), (e) $\text{Ag}/\text{Ti}/\text{Si}$ (0.1/1/1), (f) $\text{Ag}/\text{Ti}/\text{Si}$ (0.1/1/0.5), and (g) $\text{Ag}/\text{Ti}/\text{Si}$ (0.1/1/0) powder.	82

## LIST OF FIGURES (Cont')

FIGURES	TITLE	PAGE
5.6	Diffuse reflectance UV-visible absorption spectra of Ag/Ti/Si (0.1/1/0) and (c) Ag/Ti/Si (0.1/1/2) nanocomposite films	83
5.7	TEM images of (a) TiO <sub>2</sub> , Ag/Ti/Si (0.1/1/0) and (c) Ag/Ti/Si (0.1/1/2) nanoparticles (40,000 × magnification)	85
5.8	FESEM images of (a) TiO <sub>2</sub> , (b) Ag/Ti/Si (0.1/1/0), (c) Ag/Ti/Si (0.1/1/2) films and (d) thickness of Ag/Ti/Si (0.1/1/2) films	86
5.9	AFM images of (a) TiO <sub>2</sub> , (b) Ag/Ti/Si (0.1/1/0) and (c) Ag/Ti/Si (0.1/1/2) films	87
5.10	XPS survey spectra of (a) TiO <sub>2</sub> , (b) Ag/Ti/Si (0.1/1/0) and (c) Ag/Ti/Si (0.1/1/2) films	88
5.11	High resolution XPS spectra of Ti 2p on Ag/Ti/Si (0.1/1/2) film	89
5.12	High resolution XPS spectra of O 1s on Ag/Ti/Si (0.1/1/2) film	89
5.13	High resolution XPS spectra of Si 2p on Ag/Ti/Si (0.1/1/2) film	90
5.14	High resolution XPS spectra of Ag 3d on Ag/Ti/Si (0.1/1/2) film	90
5.15	Contact angle of water droplet on glass substrate, TiO <sub>2</sub> , Ag/Ti/Si (0.1/1/0) and Ag/Ti/Si (0.1/1/2) films	92
5.16	Contact angles of TiO <sub>2</sub> , Ag/Ti/Si (0.1/1/0) and Ag/Ti/Si (0.1/1/2) films at different time intervals.	93
5.17	Adsorption of MB dye on different photocatalyst flms in the dark	94
5.18	Photocatalytic degradation of MB dye on different films with various MCM-41 content under UV light irradiation	95
5.19	Photocatalytic degradation of MB dye on different films with various MCM-41 content under visible light irradiation	95

### LIST OF FIGURES (Cont')

FIGURES	TITLE	PAGE
5.20	Mechanisms of Ag/TiO <sub>2</sub> /MCM-41 nanocomposite on MB degradation irradiated under visible light	97
6.1	Photocatalytic degradation rate of benzene on different films under visible light irradiation for 6 h in batch system	102
6.2	Degradation rate of gaseous benzene on TiO <sub>2</sub> and Ag/Ti/Si (0.1/1/2) films under dark and visible light irradiation in a batch system	103
6.3	Photocatalytic degradation rates of gaseous benzene by different films under visible light irradiation	104
6.4	Removal of gaseous benzene by adsorption (in the dark) and photocatalytic activity of Ag/Ti/Si (0.1/1/2) films under UV and visible light irradiation	105
6.5	Kinetic pseudo-first-order models of gaseous benzene photodegradation by different photocatalyst films under visible light irradiation.	106
6.6	Kinetic pseudo-first-order models of gaseous benzene photodegradation on Ag/Ti/Si (0.1/1/2) films under UV and visible light irradiation.	107
A-1	Linear calibration curve of methylene blue dye	125
C-1	Linear calibration curve of gaseous benzene	127

## NOMENCLATURES

PCO	=	Photocatalytic oxidation
MCM-41	=	Mobil Catalytic Material of number 41
RH	=	Rice Husk
CTAB	=	Cetyltrimethylammonium Bromide
SiO <sub>2</sub>	=	Silica
MPS	=	Mesoporous silica
NaOH	=	Sodium hydroxide
TiO <sub>2</sub>	=	Titanium dioxide
TiO <sub>2</sub> /MCM-41	=	Titanium containing mesoporous MCM-41
B	=	Batch method
S	=	Sequence method
Ag/TiO <sub>2</sub>	=	Silver doped titanium dioxide
Ag/TiO <sub>2</sub> /MCM-41	=	Silver doped titanium dioxide containing in Mesoporous MCM-41
UV	=	Ultraviolet
VB	=	Valence band
CB	=	Conduction band
BTEX	=	Benzene, toluene, ethylbenzene and xylene
CVD	=	Chemical vapor deposition
PVC	=	Physical vapor deposition
VOCs	=	Volatile organic compounds
<i>E. coli</i>	=	<i>Escherichia coli</i>
CFU	=	Colony forming unit
MB	=	Methylene blue
IAQ	=	Indoor air quality
IUPAC	=	International Union of Pure and Applied Chemistry
JIS	=	Japanese Industrial Standards
JCPDS	=	Joint Committee on Powder Diffraction Standards
U.S.EPA	=	United States Environmental Protection Agency

WHO	=	World Health Organization
ATCC	=	American Type Culture Collection
PCD	=	Pollution Control Department
XRD	=	X-ray diffraction
UV-Vis-DR	=	UV-visible diffuse reflectance spectrometer
AFM	=	Atomic force microscope
XRF	=	X-ray fluorescence
BET	=	Brunaure-emmett-teller
TEM	=	Transmission electron microscopy
FESEM	=	Field emission scanning electron microscopy
SEM-EDX	=	Scanning electron microscopy-energy dispersive X-ray spectrometer
FTIR	=	Fourier transform infrared Spectrometer
XPS	=	X-ray photoelectron spectroscopy
GC/FID	=	Gas chromatography with flame ionize detector
RMS	=	Root mean square
%	=	Percent
e <sup>-</sup>	=	Electron
h <sup>+</sup>	=	Hole
eV	=	Electron volt
°C	=	Degree celsius
K	=	Kelvin
h	=	Hour
W	=	Watt
E <sub>g</sub>	=	Band gap energy
$\lambda$	=	Wavelength
$h$	=	Planck constant
$\nu$	=	Electromagnetic wave
c	=	Speed of light
L	=	Liter
m <sup>3</sup>	=	Cubic meter
m <sup>2</sup>	=	Square meter
atm	=	atmosphere



g	=	Gram
μg	=	Microgram
nm	=	Nanometer
μm	=	Micrometer
ppm	=	Part per million
Å	=	Angstrom
V	=	Volume
C	=	Concentration
MW	=	Molecular weight
D	=	Density

# CHAPTER 1

## INTRODUCTION

### 1.1 Rational/problem statement

Titanium dioxide ( $\text{TiO}_2$ ) photocatalyst has been widely used for various environmental applications, such as air purification [1], self-cleaning [2], self-disinfecting [3], and degradation of organic pollutants [4, 5]. At present, indoor air pollution has become serious environmental health concerns. The United States Environmental Protection Agency (U.S.EPA) estimates that people in USA spend more than 90% of their time indoors. However, indoor air is typically 5-10 times worse than the outdoor air [6]. Indoor air pollutants in general residential buildings are emitted from building materials and human activities, which directly impact to the human health and cause acute symptoms, long-term health risks or odor [7].

Indoor air pollutants listed by the World Health Organization (WHO) are benzene, carbon monoxide, formaldehyde, naphthalene, particulate matter, trichloroethylene, etc. Among these pollutants, benzene is commonly found in residential and office buildings. Benzene exposure can occur occupationally and domestically as a result of the ubiquitous use of benzene-containing petroleum products, including motor fuels and solvents. The emission of benzene sources is also from some household products such as, glues, paints, furniture wax, and lubricants [8]. Benzene is a genotoxic carcinogen in humans and no safe level of exposure can be recommended. For the concentration of airborne benzene associated with an excess lifetime risk of 1/10,000, 1/100,000 and 1/1,000,000 are 17, 1.7 and  $0.17 \mu\text{g m}^{-3}$ , respectively. Benzene can cause acute and chronic lymphocytic leukaemia, non-Hodgkin's lymphoma and multiple myeloma. Acute benzene poisoning affects the central nervous system, vomiting symptoms, and even death [9, 10].

In Thailand, the average concentration of benzene found in office buildings was about  $3.7 \mu\text{g m}^{-3}$ , mainly emitted from paintings and furniture inside the buildings [11]. However, outdoor benzene emissions are also considered a significant source contributing to indoor benzene accumulation. It was reported that the highest average 24-hour concentration of benzene found in Bangkok was up to  $6.5 \mu\text{g m}^{-3}$ . In Map Tha Phut Industrial estate, the average 24-hour concentration of benzene was in the range of 1.8 to  $5.3 \mu\text{g m}^{-3}$ . While Thailand's National Ambient Air Quality Standards for benzene is

limited as  $1.7 \mu\text{g m}^{-3}$  [12]. Currently, no indoor air quality standard is established in Thailand. The ways to relieve the adverse effects of indoor benzene exposure are avoid benzene emission, increasing ventilation rate and exploring new treatment technologies for benzene removal.

At present, the development technology for gaseous benzene removal is being widely studied. Photocatalytic oxidation (PCO) is one of the most feasible technologies to improve indoor air quality because organic pollutants can be broken down and converted to harmless substrates, such as  $\text{CO}_2$  and  $\text{H}_2\text{O}$ . In Thailand, the PCO process has been used to solve the problem of industrial odor that has an effective against off gassing, chemical contaminants, ethylene gas and more [13]. In addition, the PCO process can be applied to low concentration level of pollutants in ppb that is suitable for indoor air purification [14]. Many studies recommend titanium dioxide ( $\text{TiO}_2$ ) as a promising catalyst for PCO process because of its extensive characteristics such as relatively inexpensive, safe, chemically stable and high photocatalytic activity in ambient atmospheric environment [15]. Nevertheless, the applications of  $\text{TiO}_2$  for PCO process are restricted by its low specific surface area, charge recombination effect and the limitation of its band gap energy in UV-light region ( $\lambda < 388 \text{ nm}$ ). As a result, the application of  $\text{TiO}_2$  for indoor air treatment under visible light is practically limited.

To improve the photocatalytic reactivity of  $\text{TiO}_2$  under visible light and to reduce charge recombination, silver (Ag) is recommended as a good co-dopant of  $\text{TiO}_2$  to reduce the band gap energy and increase the lifetime of  $\text{e}^-/\text{h}^+$  pairs by capturing the photogenerated electrons. Silver nanoparticles on the surface of  $\text{TiO}_2$  can absorb the visible light and exhibit optical properties by surface plasmon resonance [16-18]. Not only for improving the photocatalytic reactivity of  $\text{TiO}_2$ , Ag can be applied for antimicrobial activity. Ag nanoparticles can inhibit the DNA synthesis with direct binding on the bacterial DNA and also reacts with the protein on the bacterial membrane forming S-Ag bonds [19-21]. Thus, Ag doped  $\text{TiO}_2$  photocatalyst possesses a dominant property for removal of airborne organic pollutants and microorganisms. The photocatalytic reactivity of Ag doped  $\text{TiO}_2$  also relies on its specific surface area. It was reported that doping Ag in to  $\text{TiO}_2$  caused a significant decrease in catalyst surface area. To solve this drawback, porous silica and mesoporous silica (MCM-41) were embedded in Ag doped  $\text{TiO}_2$  photocatalyst to increase the porosity of the photocatalyst [22].

Moreover,  $\text{TiO}_2$  has a low surface area (only  $200 \text{ m}^2 \text{ g}^{-1}$ ) when metal loading in  $\text{TiO}_2$  decreases the surface area, which can result in low photocatalytic performance. Mesoporous silica (MPS) is one of attractive method to enhance photocatalytic reactivity of  $\text{TiO}_2$ , due to high surface area and abundant of hydroxyl groups (OH) in MPS. The promoted hydroxyl radicals ( $\cdot\text{OH}$ ) behave as oxidizing agent which can destroy organic pollutants [23]. It was reported that  $\text{TiO}_2$  embedded in  $\text{SiO}_2$  catalyst had higher adsorptive capacity leading to a positive effect to photocatalytic reaction. One of nanosilica materials is Si-MCM-41, a mesoporous molecular sieve, which has uniform hexagonal crystalline and high surface area ( $> 800 \text{ m}^2 \text{ g}^{-1}$ ). Thus, this material can be used as a support of  $\text{TiO}_2$  to enhance the specific surface area of  $\text{TiO}_2$  thin film. Moreover, the functional groups of silanol (Si-OH) found in the MCM-41 structure can generate active hydroxyl radicals ( $\cdot\text{OH}$ ), which can oxidize organic pollutants during photocatalytic reactions [24, 25].

There are several methods, such as hydrothermal, ultrasound and sol-gel processes to synthesize  $\text{TiO}_2$  photocatalysts. However, a  $\text{TiO}_2$  photocatalyst is usually prepared by sol-gel method because it is easy to control the composition, does not need complicated equipment, inexpensive and appropriate for film coating. The optimal crystal sizes and structures as well as the phase compositions of  $\text{TiO}_2$  nanoparticles can be obtained by this method. However, sol-gel method usually involves long reaction time to promote the nucleation and requires high temperature for organic removal [26]. New promising method to assist sol-gel process is microwave technique. This technique has many advantaged such as convenient, fast, low temperature and no pollutants from combustion [27, 28]. Microwave irradiation can promote nucleation of titania crystals, by providing homogeneous heating in a short time, and thus reduce energy costs. Within the concept of green chemistry, a microwave assisted sol-gel has proven to be a promising method for  $\text{TiO}_2$  synthesis.

Although many studies dealing with the preparation of titanium dioxide co-doped with metal and there are composite materials, the synthesis of Ag doped  $\text{TiO}_2$  with MCM-41 film through a microwave technique has not yet been done. This research aims to investigate the optimal condition of Ag/ $\text{TiO}_2$ /MCM-41 synthesis by batch and sequence methods, using microwave assisted sol-gel and hydrothermal processes. The effective photocatalysts were further studied for environmental applications by gaseous benzene treatment in a simulated indoor air system and antibacterial activity under visible light irradiation.

## 1.2 Literature reviews

### 1.2.1 Preparation of photocatalyst

At present, attempts to reduce the wide band gap energy of  $\text{TiO}_2$  are by element doping and increase the adsorbability by a composite with silica. In preparation of Ag doped  $\text{TiO}_2$ , most researchers have used  $\text{AgNO}_3$  as a silver precursor and  $\text{TiCl}_4$ ,  $\text{Ti}(\text{OPr})_4$  or  $\text{Ti}(\text{OBu}_4)$  as titanium precursor.  $\text{TiCl}_4$  is an inorganic form which hydrolyzed easily with water, including in air, so that handling is difficult. Titanium in the organic forms is much more stable, organic solvent is then required. Therefore, heating treatment is necessary for a synthesis process and removing some organic remaining. Many preparation techniques have been employed to prepare titanium dioxide such as vapor-phase method, hydrothermal synthesis, magnetron sputtering, and sol-gel methods [26, 27].

Chemical preparation in one-step or sol-gel technique is very popular for synthesis of titania. This is due to its advantages of the perfectly controlled composition, no complicated equipment required and inexpensive. Nevertheless, this technique requires heating to high temperatures and so the processes are time consuming. Recently, the sol-gel method has been developed by using microwave assisted heating process to prepare  $\text{TiO}_2$  photocatalyst. The microwave technique generates very fast nucleation sites in the solution, which significantly enhances the reaction rates. Zhang *et al.* (2009) have studied the preparation of  $\text{TiO}_2$  samples from a microwave assisted hydrothermal reaction at  $190\text{ }^\circ\text{C}$  for 90 min. Using microwave provided a rapid heating rate, molecular homogeneity and selective heating of reaction solutions in comparison with the conventional hydrothermal method. In addition, microwave-assisted hydrothermal treatment could reduce the energy and time consuming. Moreover, no organic solvents were employed throughout the synthesis which can reduce the effect of pollution on the environment [27].

Generally, the photocatalytic process of  $\text{TiO}_2$  requires energy in the range of UV light ( $\lambda < 387\text{ nm}$ ), leading to limitations of  $\text{TiO}_2$  when applied under visible light ( $\lambda > 400\text{ nm}$ ). Doping  $\text{TiO}_2$  with noble metals, such as Ni, Fe, Au, Ag, and Pt, to create a  $\text{TiO}_2$  photocatalyst are a popular method to decrease band gap energy. These metals can produce traps to capture the photogenerated electrons or holes, leading to the reduction of electron-hole recombination and improving the light absorption capability for visible light. Doping of  $\text{TiO}_2$  with Ag is an attractive method to reduce the band gap energy of  $\text{TiO}_2$ , and prevent  $\text{e}^- \text{-h}^+$  recombination. Suwarnkar *et al.* (2013) prepared Ag doped  $\text{TiO}_2$

nanoparticles (concentration of Ag as 0.12-0.5 mol%) by microwave irradiation at 900 W for 20 min. 0.25% of Ag/TiO<sub>2</sub> provided the highest degradation efficiency on methyl orange. They reported that Ag doped TiO<sub>2</sub> can effectively capture the photoinduced electrons which immediately transfer to oxygen, resulting in the increase of surface hydroxyls [29]. Yu *et al.* (2013) have reported that Ag doped TiO<sub>2</sub> exhibited high adsorption rates in visible light. This is a result of the surface plasmon resonance of Ag nanoparticles, in which the electrons migrate to the conduction band of TiO<sub>2</sub> and are further trapped by O<sub>2</sub>, producing oxidative species, resulting in the oxidation of organic pollutants [30].

Recently, TiO<sub>2</sub> thin films have been modified with a mesoporous silica in order to improve the adsorbability of the film. The composite of TiO<sub>2</sub> and porous materials can enhance the photocatalytic activity of TiO<sub>2</sub>. It was reported that the photocatalytic activity of TiO<sub>2</sub> increases because mesoporous silica increases its surface area [31]. The mechanism of photocatalytic activity of TiO<sub>2</sub> on mesoporous silica (MPS) has been studied. The suggestion is that TiO<sub>2</sub> hybrid with MPS with low Ti amounts is suitable for selective polar substrates production.

The advantages of TiO<sub>2</sub> doped in MPS are (i) additive free, (ii) cheap source of oxidant, and (iii) mild reaction condition [32]. Klankaw *et al.* (2011) concluded that mesoporous MCM-41 which has a highly ordered hexagonal structure and large surface area (> 800 m<sup>2</sup> g<sup>-1</sup>), can enhance the specific surface area of TiO<sub>2</sub> thin film. Moreover, the functional groups of silanol (Si-OH) found in the MCM-41 structure can generate active hydroxyl radicals (<sup>•</sup>OH) to TiO<sub>2</sub> photocatalyst, which behave as an oxidizing agent and destroy organic pollutants [33].

Wang *et al.* (2012) was successfully prepared TiO<sub>2</sub>/MCM-41 by microwave irradiation which could provide an efficient way for rapid and uniform crystallization heating. Titanium atoms are entirely incorporated into the MCM-41 framework and mainly in tetrahedral coordination. The rich Ti(IV) sites in framework are significantly advantageous to enhance the catalytic properties of TiO<sub>2</sub>/MCM-41 materials [34]. The effect of Ag, TiO<sub>2</sub> and MCM-41 can enhance the overall photocatalytic reactivity under both UV and visible light. This is because Ag plays an important role in the improvement of visible light absorption and MCM-41 can increase the adsorbability of the catalyst [28].

Chen *et al.* (2011) studied the photocatalytic performance of the co-doped Ag-Si/TiO<sub>2</sub> photocatalyst in visible light. The high thermal stability and the phase

transformation were retarded to about 900 °C. The particle size has become smaller which enlarge its surface area and UV-vis light absorption is shifted to visible region after doping. The photocatalytic performance of Rhodamine B degradation increases with the obtained Ag–Si/TiO<sub>2</sub> sample, reaching the maximum at the Ag and Si content of 0.5 mol% and 20.0 mol%, respectively [31]. It could be attributed to the synergistic effect that occurred from co-doping by silver and silicon.

### 1.2.2 Environmental applications of photocatalyst

Photocatalytic oxidation of TiO<sub>2</sub> photocatalyst is the most frequently used for environmental applications, because TiO<sub>2</sub> is stable, non-toxic and is capable of degrading a wide range of organic pollutants. Most researches have employed the photocatalytic reactivity of Ag/TiO<sub>2</sub> with gaseous VOCs by using the high wattage of light source lamps such as under 300 W Xe lamp [17], which is not suitable for indoor application. As a result, the improvement of photocatalytic reactivity under visible light has been more attractive for indoor applications. Recently, the visible light responsive of TiO<sub>2</sub> photocatalyst has been developed by doping silver (Ag). Peerakiatkhajorn *et al.* (2012) have studied the treatment of benzene, toluene, ethylbenzene and xylene (BTEX) by Ag doped TiO<sub>2</sub> coated onto a plastic substrate irradiated with two 8 watts fluorescence lamps. The results showed that the maximum degradation efficiency of benzene on 10% mol Ag doped TiO<sub>2</sub> thin film was 79% within 4 h, better than that of pure TiO<sub>2</sub> thin film for four times [18].

The application of Ag doped TiO<sub>2</sub> has also given another benefit in antibacterial activity. Dunnill and co-workers (2011) revealed that Ag doped to TiO<sub>2</sub> film can apply for antimicrobial activity of *Escherichia coli* bacteria under visible light. The result showed a 99.99% reduction in the number of viable bacteria due to the synergistic relationship between the photocatalyst (TiO<sub>2</sub>) and the surface bound silver nanoparticles [35]. The effect result from antibacterial testing of silver had implied from a previous research that silver nanoparticles at concentrations of 60 µg mL<sup>-1</sup> was attributed to reduce growth of bacterial cells until virtually nonexistent. Also the both ionic silver and silver nanoparticle have strongly interact with *E. coli* and found to be effective bactericides. Ag can penetrate inside the bacteria and caused damage by interacting with phosphorus and sulfur containing compounds such as DNA and enzyme [20]. Thus, it is interesting that doped Ag and mesoporous MCM-41 on to TiO<sub>2</sub> can improve photocatalytic performance in visible light and applied for indoor air treatment.

### 1.3 Research objectives

1. To synthesize visible light-responsive Ag/TiO<sub>2</sub>/MCM-41 nanocomposite film by microwave-assisted sol-gel technique.
2. To study the physical and chemical properties of Ag/TiO<sub>2</sub>/MCM-41 nanocomposite film and its synergistic effects in photocatalysis.
3. To study the photocatalytic activity of Ag/TiO<sub>2</sub>/MCM-41 nanocomposite film for the degradation of benzene gas and for an antibacterial application.

### 1.4 Scope of work

1. MCM-41 used in this study was prepared from extracted rice husk silica following Chiarakorn (2003).
2. The preparation of TiO<sub>2</sub>/MCM-41 powder was studied by batch (B) and sequence (S) methods with microwave-assisted sol-gel technique
3. Ag/TiO<sub>2</sub>/MCM-41 powder was prepared in the form of powder and film by varying Ag molar ratios as 0, 0.01, 1 and 2 and Si molar ratios as 0, 0.5, 1 and 2.
4. The photocatalyst films were fixed on a glass substrate by dip-coating and calcination at 550 °C.
5. The photocatalytic activity of photocatalyst films was tested with methylene blue dye under UV and visible light irradiation.
6. The photocatalyst films were applied for the phodegradation of gaseous benzene in a simulated indoor air system and for antibacterial activity of *E. coli* under visible light irradiation.



## CHAPTER 2

### THEORIES

#### 2.1 Indoor air pollution (IAQ)

Indoor air pollutants mainly include nitrogen oxide, volatile organic compounds (VOCs), particulates and biological pollutants. Every year, indoor air pollution is responsible for the death of 1.6 million people around the world – that is one death every 20 seconds. Many people spend large portion of time indoors - as much as 90% of their lives [36]. For these reasons, some experts feel that more people suffer from the effects of indoor air pollution than outdoor pollution. World Health Organization (WHO) has established list of priority indoor air pollutants, based on the ubiquity, concentration and toxic effect of the substances involved as shown in Table 2.1. These priority lists will most likely evolve upon new analytical and toxicological findings more relevant to IAQ such as the health effects of chronic exposure to multiple pollutants at low concentration.

**Table 2.1** Summary of indoor air quality guidelines for selected pollutants [8].

Pollutants	Critical outcomes for guideline definition
Benzene	- Acute myeloid leukaemia (sufficient evidence on causality) - Genotoxicity
Carbon monoxide	- Acute exposure-related reduction of exercise tolerance and increase in symptoms of ischaemic heart disease
Formaldehyde	- Sensory irritation
Naphthalene	- Respiratory tract lesions leading to inflammation and malignancy in animal studies
Nitrogen dioxide	- Respiratory symptoms, bronchoconstriction, increased bronchial reactivity, airway inflammation and decreases in immune defence, leading to increased susceptibility to respiratory infection
Aromatic hydrocarbons	- Lung cancer
Radon	- Lung cancer - Suggestive evidence of an association with other cancers, in particular leukaemia and cancers of the extrathoracic airways
Trichloroethylene	- Carcinogenicity (liver, kidney, bile duct and non-Hodgkin's lymphoma), with the assumption of genotoxicity
Tetrachloroethylene	- Effects in the kidney indicative of early renal disease and impaired performance

In fact, some buildings contain such high levels of contaminants that they are qualified as “sick” because exposure to them results in multiple sickness symptoms (e.g. headaches, fatigue, skin and eye irritations, or respiratory illnesses), commonly described as the “sick building syndrome” (SBS). Indoor air pollutants with significant indoor sources can be generally divided into three classes, i.e., combustion by-products, volatile organic compounds (VOCs), and biogenic particles [37].

#### 2.1.1 Sources of indoor air pollution

##### 2.1.1.1 Volatile organic compounds (VOCs)

Indoor VOCs (together with CO, CO<sub>2</sub>, CH<sub>4</sub>) come from a variety of chemicals such as tobacco smoke, vehicular emissions from nearby roadsides, and the use of liquefied petroleum gas cooking stoves. VOCs are emitted by a wide array of products numbering in the thousands. Examples include: paints and lacquers, paint strippers, cleaning supplies, pesticides, building materials and furnishings, office equipment such as copiers and printers, correction fluids and carbonless copy paper, graphics and craft materials including glues and adhesives, permanent markers, and photographic solutions. All of these products can release organic compounds while you are using them, and, to some degree, when they are stored. Among numerous compounds which belong to indoor VOCs, benzene or some polycyclic aromatic hydrocarbons are recognized as human carcinogens, a direct association between exposure to VOCs and SBS symptoms or cancer has not been fully established at typical indoor air concentrations are the major VOCs found in an indoor environment at the highest concentration [36].

In Thailand, the activity pattern of people living in the cities is similar to those of western people. A survey of time used by Thai people living in the municipal area indicates that the average time spent indoors was 87% of which working or studying time accounted for 9 h. However, the indoor air VOCs in Thailand has been less investigated. The monitoring of outdoor VOCs has been received greater attention than that of indoor due to large emissions from industrial and transportation sectors [37]. The Pollution Control Department (PCD) regularly monitors ambient VOCs determined the national standard of 9 VOCs in the ambient air from continuously 24 hour ambient air sampling as summarized in Table 2.2.

**Table 2.2** VOCs in ambient air standards of Thailand determined from continuous 24-hour sampling [12].

Pollutants	Standard
Benzene	Not exceed $1.7 \mu\text{g m}^{-3}$
Vinyl Chloride	Not exceed $10 \mu\text{g m}^{-3}$
1,2-Dichloroethane	Not exceed $0.4 \mu\text{g m}^{-3}$
Trichloroethylene	Not exceed $23 \mu\text{g m}^{-3}$
Dichloromethane	Not exceed $22 \mu\text{g m}^{-3}$
1,2-Dichloropropane	Not exceed $4 \mu\text{g m}^{-3}$
Tetrachloroethylene	Not exceed $200 \mu\text{g m}^{-3}$
Chloroform	Not exceed $0.43 \mu\text{g m}^{-3}$
1,3-Butadiene	Not exceed $0.33 \mu\text{g m}^{-3}$

#### 2.1.1.2 Microbial

There are three major types of indoor air contaminants, i.e. chemical, physical and biological. In the past, many studies only focused on the chemical pollutants in the indoor environments. Recently, biological pollutants including bacteria, fungi and viruses play an important role on defining the IAQ in which fungi are usually considered to be the major sources of microbial contamination in the indoor environments. It is supposed that about 30% of health problems relevant to the indoor air quality is the result of a human organisms reaction to molds [38]. Many studies focused on the concentration of bacteria in the indoor environments and they just made use of those data as the indoor air quality indicator. The bacteria that come from human are mainly from the skin and respiratory tract, and were released by occupants into the sites through shedding off from skin, sneezing or talking; whereas the soil bacteria were usually dispersed in the air by dust. Therefore, the bacteria isolated from the sampling sites were contributed by human and the outdoor environment. Finally, the majority of the bacteria was either opportunistic pathogens or non-pathogenic, and they would cause diseases only in sensitized or grossly immuno-compromised individuals, with the exception of *Moraxella catarrhalis* which is usually considered pathogenic [39].

Microorganisms and/or their reproductive structures are almost always found in outdoor air. Their types and populations will vary depending on local environmental conditions. Doors, windows, and fresh air intakes provide easy access for microorganisms to enter the interiors of buildings. Microorganisms break down dead material into its

constituent components and as such, are important participants in the earth's continuing life cycle. However, if these microorganisms proliferate in buildings, they can adversely impact indoor air quality (IAQ), create hazardous health conditions for the occupants and contribute to the deterioration of building components. Mold and bacteria can release microscopic particles into the air. The metabolism of mold and bacteria can create microbiological volatile organic compounds (MVOCs), including a wide range of alcohols, ketones, aldehyde, esters, carboxylic acids, lactones, terpenes, aromatic hydrocarbons, sulfur and nitrogen compounds, that adversely affect air quality inside the building [40]. These particles may settle on indoor surfaces and then be resuspended by human activities or by air movement. The particles may contain allergens, chemicals that can cause inflammation in respiratory tissues, or toxic chemicals with the theoretical potential to cause other health effects such as inhibited immune system function or effects on the central nervous system.

#### 2.1.2 Effects of indoor air pollutants on human health

There is consistent evidence that exposure to indoor air pollution increases the risk of pneumonia among children under five years, as well as chronic respiratory disease and lung cancer (in relation to the use of coal) among adults over 30 years old. The evidence for a link with lung cancer from exposure to biomass smoke, and for a link with asthma, cataracts and tuberculosis was considered moderate. The extent to which an individual is harmed by air pollution usually depends on the total exposure to the damaging chemicals, i.e., the duration of exposure and the concentration of the chemicals must be taken into account. Air pollution can affect our health in many ways with both *short-term* and *long-term* effects [40].

**Short-term effects** include irritation to the eyes, nose and throat, and upper respiratory infections, such as bronchitis and pneumonia. Other symptoms can include headaches, nausea, and allergic reactions. Short-term air pollution can aggravate the medical conditions of individuals with asthma and emphysema. In the great "Smog Disaster" in London in 1952, four thousand people died in a few days due to the high concentrations of pollution.

**Long-term health effects** can include chronic respiratory disease, lung cancer, heart disease, and even damage to the brain, nerves, liver, or kidneys. Continual exposure to air pollution affects the lungs of growing children, and may aggravate or complicate medical conditions in the elderly. It is estimated that half a million people die prematurely

every year in the United States as a result of smoking cigarettes. As concern about indoor air quality (IAQ) has grown in recent years, understanding indoor aerosols has become increasingly important so that control techniques may be implemented to reduce damaging health effects.

Some biological contaminants trigger allergic reactions, including hypersensitivity pneumonitis, allergic rhinitis, and some types of asthma. Infectious illnesses, such as influenza, measles, and chicken pox, are transmitted through the air. Molds and mildews release disease-causing toxins. Symptoms of health problems caused by biological pollutants include sneezing, watery eyes, coughing, shortness of breath, dizziness, lethargy, fever, and digestive problems. Allergic reactions occur only after repeated exposure to a specific biological allergen. However, that reaction may occur immediately upon re-exposure or after multiple exposures over time. As a result, people who have noticed only mild allergic reactions, or no reactions at all, may suddenly find themselves very sensitive to particular allergens. Some diseases, such as humidifier fever, are associated with exposure to toxins from microorganisms that can grow in large building ventilation systems. However, these diseases can also be traced to microorganisms that grow in home heating and cooling systems and humidifiers. Children, elderly people, and people with breathing problems, allergies, and lung diseases are particularly susceptible to disease-causing biological agents in the indoor air. Mold, dust mites, pet dander, and pest droppings or body parts can trigger asthma. Biological contaminants, including molds and pollens can cause allergic reactions for a significant portion of the population. Tuberculosis, measles, staphylococcus infections, *Legionella* and influenza are known to be transmitted by air [41].

### 2.1.3 Indoor air treatment

Existing solutions to poor indoor air quality include the combination of actions such as removing the pollutant sources, increasing ventilation rates and improving air distribution, and cleaning the indoor air. Although certain furniture or appliance-manufacturers are already phasing out the use of formaldehyde, removing the pollutant sources is only possible when these are known and control is technically or economically feasible, which is seldom the case. New substances are constantly detected and classified as hazardous and many sources can release compounds for years. In addition, there are fears that many air pollutants are yet to be discovered and preventive approaches might therefore be needed to ensure indoor air contaminants are maintained below satisfactory

levels at all times. Natural aeration is the easiest alternative, but it is often not possible because of outdoor weather, external pollution conditions or issues of security, safety in high buildings, climate control, or noise. Periodical air refreshing is often not efficient, because many indoor air pollutants are constantly released. Hence, forced ventilation is still one the most common methods used for air treatment.

**Table 2.3** Current and emerging indoor air treatment methods [36].

Method	Principle
Filtration	Air is passed through a fibrous material (often coated with a viscous substance), which is efficient for particle removal but not gases. Filters are compact and commonly used but their efficiency decreases as they become saturated (fouling). Microorganisms can also develop in filters and particle reemission might occur.
Electrostatic precipitator with ionization	An electric field is generated to trap charged particles. Electrostatic precipitators are often combined with ion generator that charge particles can be removed efficiently but it can generate hazardous charged particles.
Adsorption	Air pollutants are adsorbed onto activated carbon or zeolites, often as filtration post-treatment. The adsorbent might be too specific and might saturate fast because the pollutants are not destroyed. Therefore, there is a potential risk of pollutant reemission.
Ozonation	Ozone is generated to oxidize pollutants. Only removes some fumes and certain gaseous pollutants and might generate unhealthy ozone and degradation products. Ozone-based purifiers are not recommended by the American Lung Association.
Photolysis	High-energy ultraviolet radiation oxidizes air pollutants and kills pathogens. However, it can however only remove some fumes and some gaseous pollutants and might release toxic photoproducts. Accidental exposure to UV light is harmful. UV irradiation energy consumes.
Photocatalysis	High-energy ultraviolet radiation is used in combination with a photocatalyst ( $\text{TiO}_2$ ) to generate highly reactive hydroxyl radicals that can oxidize most pollutants and kill pathogens. This energy-intensive method is increasingly popular and suitable for a broad range of organic pollutants.

Current methods for air purification include air filtration, ionization, activated carbon adsorption, ozonation, and photocatalysis (Table 2.3). These processes can be integrated into central ventilation systems (in ducts) or used in portable air purifiers (or air cleaners) designed for limited spaces. Efficient strategies for particle removal are now well established and include combinations of filtration and electrostatic precipitation. However

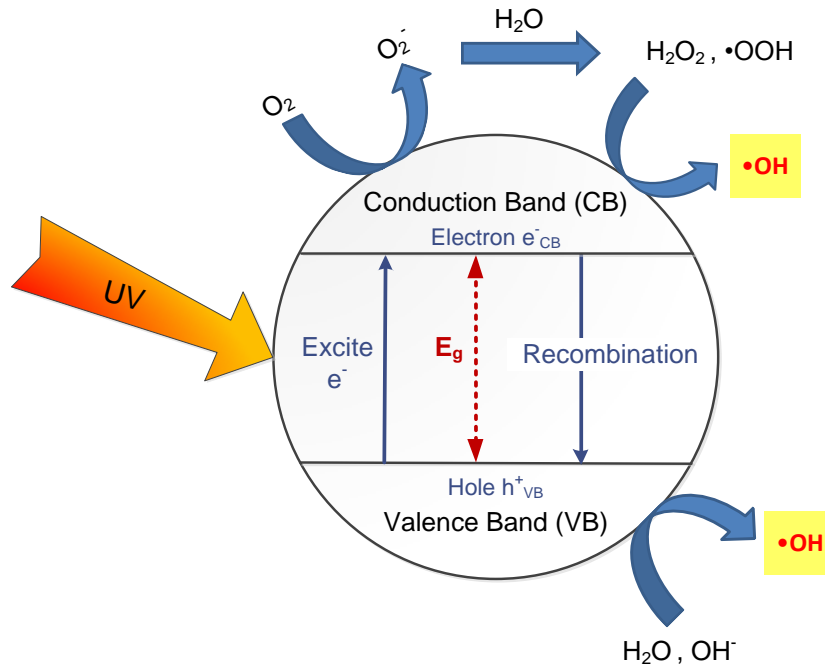
these technologies are very difficult for VOC removal. Although high efficiency particles air filters and electrostatic precipitators were highly efficient for particle removal, none of the techniques tested (filtration, electrostatic precipitation, ionization, ozonation, activated carbon adsorption) could significantly remove organic gases [36]. Almost all studies have focused on the photodegradation of pollutants and no deactivation was found. Among these techniques, photocatalysis is a feasible technology for the removal of VOCs gases at typical indoor air level.

## 2.2 Photocatalysis

The definition of photocatalysis was defined by one of the IUPAC Commissions in the past as “a catalytic reaction involving light absorption by a catalyst or a substrate”. The catalyst may accelerate the photoreaction by interacting with the substrate(s) either in its ground state or in its excited state, or with the primary product (of the catalyst), depending on the mechanism of the photoreaction.

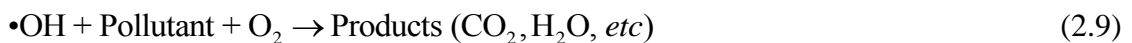
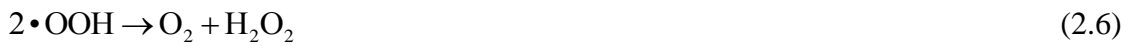
### 2.2.1 Mechanism of photocatalyst

In a semiconductor, the energy width of the forbidden band between the valence band and the conduction band is referred to band gap energy ( $E_g$ ), which determines the optical absorption wavelength of light. It is as known that with a large band gap, electrons in the valence band (VB) cannot jump up to the conduction band (CB). However, when energy is applied by photons illumination whose energy is equal or greater than the band-gap energy, electrons that were initially located in the valence band all jump up to the conduction band. This is equivalent to the movement of electrons from the bonding orbital to the anti-bonding orbital which generally unstable and can easily breakdown. These creative electron-hole ( $e^-_{CB}/h^+_{VB}$ ) pairs can either recombine to produce heat, or be used to reduce or oxidize species at the semiconductor's surface. The positive holes react with adsorbed water to form highly reactive hydroxyl radicals ( $\bullet OH$ ), which can initiate the oxidation of the adsorbed organic compounds [42]. Under optimal reaction conditions, organic pollutants can be completely oxidized to form carbon dioxide, water and final products.



**Figure 2.1** Primary mechanism of photocatalytic reaction [42].

A possible reaction pathway can be described from titanium dioxide ( $\text{TiO}_2$ ) photocatalyst in Equations (2.1-2.9).



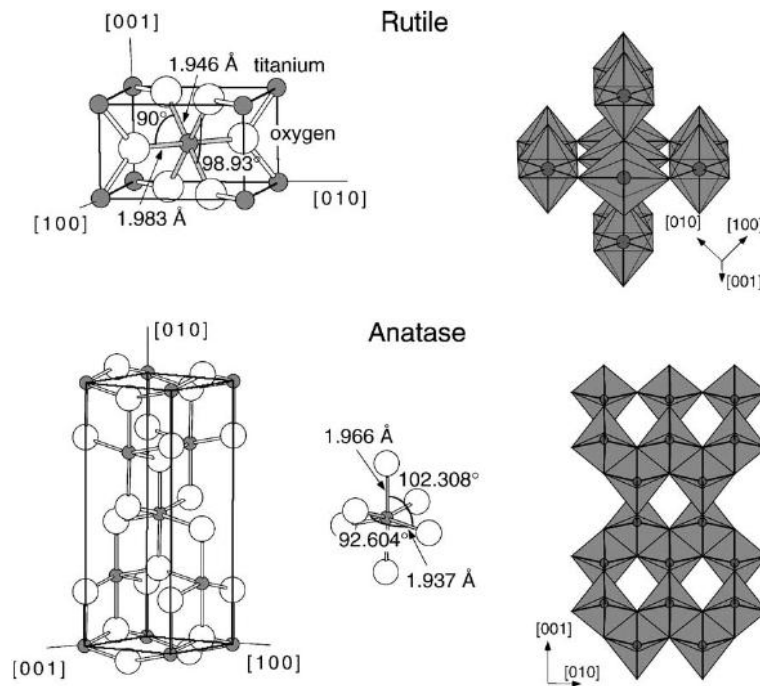
$\text{TiO}_2$ -based catalysts are one of the most efficient photocatalysts used for the photocatalytic degradation of organic pollutants, due to their high activity and high



stability. The performance of a catalyst depends on many factors, such as particle size, preparation method, co-catalyst, etc.

### 2.2.2 Titanium dioxide

Titanium dioxide ( $\text{TiO}_2$ ) crystal exists in three main different structures: anatase (tetragonal), rutile (tetragonal) and brookite (rhombohedral), but the first two are considered. Their unit cells are shown in Figure 2.2. In both structures, the basic building block consists of a titanium atom surrounded by six oxygen atoms in a more or less distorted octahedral configuration. In each structure, the two bonds between the titanium and the oxygen atoms at the aspics of the octahedron are slightly longer. A sizable deviation from a  $90^\circ$  bond angle is observed in anatase. For rutile, the  $(110)$ ,  $(001)$  and  $(100)$  surfaces have been studied, with  $(110)$  being the most stable one [43].



**Figure 2.2** Bulk structures of rutile and anatase [43].

In a photocatalytic process, the anatase structure is more potential than the rutile form despite the band-gap value of anatase (3.2 eV) being higher than rutile (3.0 eV) due to the excited UV wavelength. Therefore, the  $\text{TiO}_2$  in anatase form is widely introduced for degradation of some contaminant substances. The comparison of characteristics between  $\text{TiO}_2$  in rutile and anatase form, was shown in Table 2.4.

**Table 2.4** Characteristics of TiO<sub>2</sub> crystal structure [43].

Properties	Rutile	Anatase
Crystalline form	Tetragonal	Tetragonal
Band gap energy (eV)	3.03	3.2
Hardness (Mohs)	6.0-7.0	5.5-6.0
Density (g cm <sup>-3</sup> )	4.25	3.894
Gibbs free energy, $\Delta G_f^\circ$ , (kcal/mol)	-212.6	-211.4
Lattice constant, a (Å)	4.593	3.784
Lattice constant, c (Å)	2.959	9.515
Melting point (°C)	1858	Transform to rutile at above 800 °C

Commonly, the two principal catalytic phases of TiO<sub>2</sub>, anatase and rutile, have numerous structural and functional differences. The anatase phase, typically less than 50 nm in size, has the adsorptive affinity for organic compounds higher than that of rutile. Moreover it exhibits lower rates of recombination in comparison to rutile. In contrast, the rutile phase generally exists as particles larger than 200 nm. It has a smaller band gap with excitation wavelengths that extend into the visible. Nevertheless, anatase is generally regarded as the more photochemically active phase of titania. At present, the commercial TiO<sub>2</sub> (Degussa P25) is produced to mixed-phase materials (75% anatase and 25% rutile) such formulations of TiO<sub>2</sub> exhibit higher photocatalytic activity than either pure phase alone. These mixed-phase TiO<sub>2</sub> formulations have been used in many innovative commercial applications for the control of organic contamination including air-purifying bathroom tiles and self-cleaning glass surfaces for the consumer market [44].

However, using TiO<sub>2</sub> is restricted by two phenomena: one is the limited wide band gap of titania, anatase (3.2 eV) and rutile (3.0 eV), useful only in the UV light region ( $\lambda < 388$  nm) and the other is the production of active electron-hole pairs for which charge recombination occurs. Titanium dioxide photocatalyst does not require ultraviolet rays that have an energy level as high as 254 nm and hazardous humans, absorbed by DNA of living mechanisms and damaging. It also allows reactions to be initiated by the near-ultraviolet rays with relatively long wavelengths contained in sunlight and emitted by fluorescence lamps [43]. Furthermore, the development of TiO<sub>2</sub> can be made to workable under visible light by doping with transition metals such as Pt [45], Au [46] and Cu [47]. The modification of TiO<sub>2</sub> photocatalyst by doping with metals represents the reduction in band

gap energy by the creation of energy levels, increasing light absorption wavelength. Doped metals act as electron traps, facilitating charge separation and preventing electron-hole recombination [48].

### 2.2.3 Silver doped titanium dioxide

The silver particles deposited on the surface of the titania can act as electron-hole separation centers. Yu *et al.* (2013) reported that Ag doped TiO<sub>2</sub> exhibited high adsorption rates in visible light. This is a result of the surface plasmon resonance photolysis of Ag nanoparticles, in which the electrons migrate to the conduction band of TiO<sub>2</sub> and are further trapped by O<sub>2</sub>, producing oxidative species [30]. The radius of Ag<sup>+</sup> ion (126 pm) is much larger than that of Ti<sup>4+</sup> (68 pm) and so the Ag<sup>+</sup> ions introduced by the sol-gel process would not enter into the lattice of anatase phase. During calcination, these uniformly dispersed Ag<sup>+</sup> ions would gradually migrate from the volume of the TiO<sub>2</sub> to the surface by enhancing their crystallinity. The release of silver ion is also affected by the calcination temperature, and the amount of silver ion released decreases with increasing the calcinations temperature. This is attributed to the fact that the titania grains aggregate each other to form large grains and the silver ions trap in the composite powder during thermal treatment, thereby less silver ions can be released from the powders into the water. Moreover, silver ion is unstable and transforms easily into black metallic silver or brown silver oxide during thermal treatment, resulting in the decrease of the release rate of silver ion [49].

The silver ion is either reduced during the synthesis phase by irradiating the sample with light or forms during calcination of the sol-gel material via the decomposition of silver nitrate. The silver ion has been reduced into metallic phase by two ways. The first was to directly reduce the AgNO<sub>3</sub> material to silver oxide (Ag<sub>2</sub>O) by irradiating with light with 250 W for 60 min. Another way was to directly calcinate the sample 600 °C for 2 h allowed the thermal decomposition of silver nitrate to occur according to equation (2.10):



For the pre-irradiation samples, the photoreduced Ag cannot be highly dispersed in the surface of TiO<sub>2</sub>; therefore, the amount of active sites on the Ag/TiO<sub>2</sub> surface cannot be changed significantly. The leveling off in photocatalytic activity on further increasing

amount of silver is most likely due to the fact that as the concentration of silver becomes large, it results in one of a number of effects:

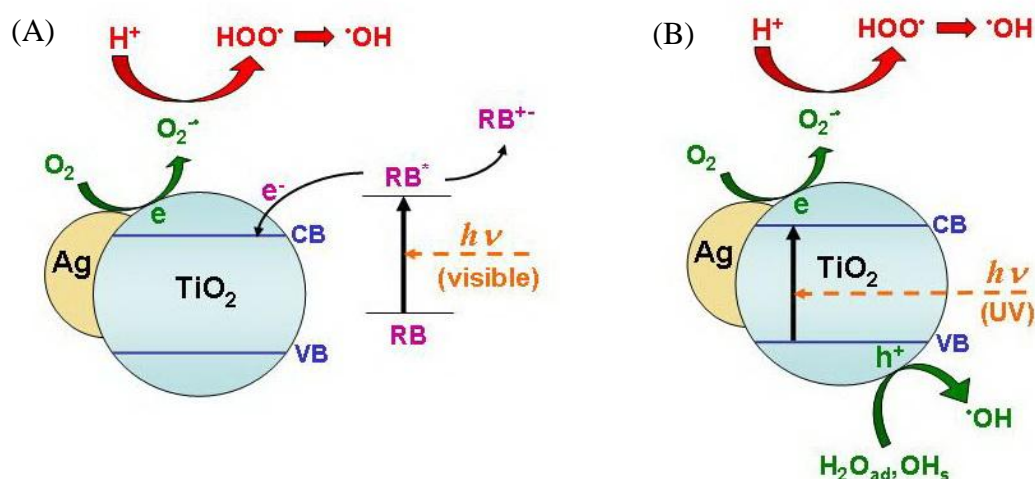
- (i) It acts as a barrier preventing light absorption by titania,
- (ii) It prevents the organic substrate from contacting the titania surface, and
- (iii) The silver may become a significant centre for electron-hole recombination.

The electron transfer from the  $\text{TiO}_2$  conduction band to metallic silver particles at the interface is thermodynamically possible because the Fermi level of  $\text{TiO}_2$  is higher than that of silver metals [48].

The effect of Ag deposited on  $\text{TiO}_2$  may show different effects on the photocatalytic activity depending on the wavelength of light illuminating photoreaction systems, because the photocatalytic mechanism under UV irradiation is generally different from that under visible light irradiation, as shown in Figure 2.4. Consequently, Ag doped or deposited on  $\text{TiO}_2$  are expected to show various effects on the photocatalytic activity of  $\text{TiO}_2$  by the different mechanisms as followed that may act separately or simultaneously depending on the photoreaction conditions. The photodegradation of dye under visible and UV light irradiation can be dedicated to photocatalytic activities by examining from the photocatalytic degradation of the rhodamine B (RB) dye [50]. In addition to these different roles of Ag deposits, the RB photodegradation in aqueous  $\text{TiO}_2$  suspension has been shown to follow the different photocatalytic pathways under UV and visible irradiation.

#### 2.2.3.1 Ag doped $\text{TiO}_2$ under visible light irradiation

The photodegradation of RB in the Ag doped  $\text{TiO}_2$  nanosol under visible light irradiation might be occurred according to Sung-Suh *et al.* (2004) described by the three mechanisms, as shown in Figure 2.3 (A).



**Figure 2.3** Photocatalytic pathways for the RB photodegradation on Ag-TiO<sub>2</sub> particles under (A) visible and (B) UV irradiation [50].

In mechanism (I), the self-photosensitization pathway, RB is activated into its excited state at  $\lambda > 470$  nm, injecting an electron into the conduction band of the TiO<sub>2</sub> semiconductor, whereas RB is covered to the cationic radical (RB<sup>•+</sup>). The injected electron on the TiO<sub>2</sub> particle reacts with adsorbed oxidants (usually O<sub>2</sub>) to produce reactive oxygen radicals (e.g., O<sub>2</sub><sup>•-</sup>, <sup>•</sup>OOH, <sup>•</sup>OH) which can degraded RB<sup>•+</sup>. The semiconductor TiO<sub>2</sub> acts only as electron transfer mediator and the oxygen as an electron acceptor leading to an efficient separation of the injected electron and RB<sup>•+</sup> (acting as a hole). For the RB photodegradation on Ag/TiO<sub>2</sub> under visible irradiation, the Ag particles on the TiO<sub>2</sub> surface can act as electron traps facilitating the electron-hole separation and subsequent electron transfer to the adsorbed O<sub>2</sub>.

In mechanism (II), more RB molecules are adsorbed on the Ag/TiO<sub>2</sub> surface than on the TiO<sub>2</sub> surface, thus leading to the injection of more photoexcited electrons from RB<sup>\*</sup> to the conduction band of TiO<sub>2</sub> in self-photosensitization pathway under visible irradiation. The enhanced RB adsorption on the Ag/TiO<sub>2</sub> surface can be supported by both the significant blue shift in  $\lambda_{\text{max}}$  of RB due to faster de-ethylation of RB on Ag/TiO<sub>2</sub> during the RB photodegradation and a decrease in the RB adsorbance ( $\lambda_{\text{max}}$ ) after contact with Ag/TiO<sub>2</sub> particle in the dark.

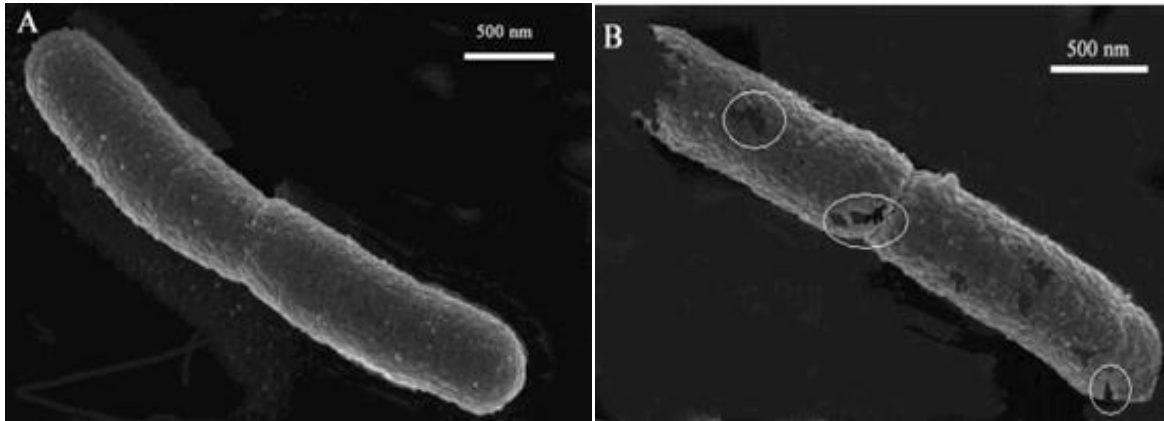
In mechanism (III), the surface plasmon resonance of Ag metals on TiO<sub>2</sub> is excited by visible light, enhancing the surface electron excitation and electron-hole separation.

### 2.2.3.2 Ag doped TiO<sub>2</sub> under UV light irradiation

The RB photodegradation on Ag/TiO<sub>2</sub> under UV irradiation is represented in Figure 2.3 (B). The Ag deposition slightly increases the TiO<sub>2</sub> photoactivity. This is ascribed according to the effect of Ag deposits only mechanism (I) under UV irradiation. In the TiO<sub>2</sub>-sensitization pathway for the RB photodegradation under UV irradiation, the valence electrons of TiO<sub>2</sub> particles are excited to the conduction band by UV light and after various other events, electron on the TiO<sub>2</sub> particle surface are scavenged by the present molecular oxygen to produce reactive oxygen radicals, whereas the valence hole become trapped as the surface-bound OH<sup>•</sup> radicals on oxidation of either the surface OH<sup>-</sup> group and the surface H<sub>2</sub>O molecules. Therefore, the charge separation on TiO<sub>2</sub> is a crucial factor to affect the efficiency of the RB photodegradation in TiO<sub>2</sub> under UV irradiation. For the RB photodegradation on Ag/TiO<sub>2</sub> under UV irradiation, Ag metals act as electron traps according to mechanism I thereby enhancing the charge separation. For the mechanism II is not applicable under UV irradiation because the Ag surface plasmon resonance is not excited by UV light [50].

### 2.2.3.3 Antibacterial activity of Ag doped TiO<sub>2</sub>

The photocatalytic activity of Ag/TiO<sub>2</sub> nanoparticles depends not only on the properties of the enhancement of its photocatalytic efficiency; however, silver nanoparticles have prospective applications, including biosensing, biodiagnostics, optical fibers, and antimicrobial and photocatalytic uses. Silver nanoparticles have high activity to penetrate inside the bacteria and believed have caused damage by interacting with DNA and enzyme [51]. After silver nanoparticles penetrate into the bacteria inactivate their enzymes, generate hydrogenperoxide and cause bacterial cell death. It has been observed that heavy metals are toxic and reactive with proteins therefore, they bind proteins molecules; as a result cellular metabolism is inhibited causing death of microorganism [20]. The silver ion (Ag<sup>+</sup>) could inhibit the DNA synthesis with direct binding on the bacterial DNA and also adsorbs the protein on the bacterial membrane influencing membrane synthesis with S-Ag bonds [19]. The Ag<sup>+</sup> bacterial effect is of great use for preventing the bacterial infection at osseointegration phase because it can trap the excited electrons from TiO<sub>2</sub> and leave the holes for the degradation reaction [51]. Figure 2.4 shows the outer membrane of the *E. coli* cell can be damaged on the mesoporous Ag/TiO<sub>2</sub> as presented in (a) before and (b) after destroyed which is investigated by FESEM.



**Figure 2.4** FESEM of *E. coli* (A) before and (B) after being damaged on the mesoporous Ag doped TiO<sub>2</sub> film [51].

#### 2.2.4 Photocatalytic oxidation

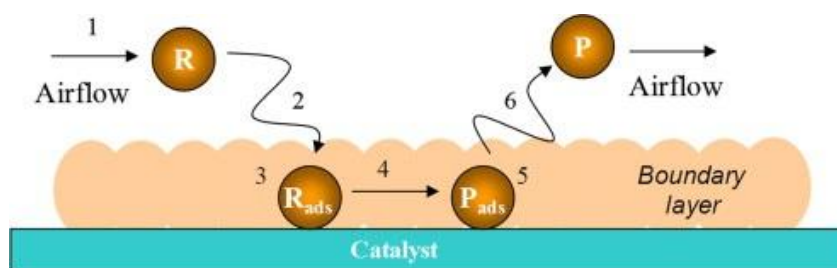
The literature mentions air purification techniques of photocatalytic oxidation (PCO), identified since 1906 that provide a wide range of potential applications. The PCO process is a new advance oxidation technology (AOTs), which has been widely established as an alternative physical-chemical process for the elimination of toxic and hazardous organic substances and metals in wastewaters, drinking water, and air. The advantage of photocatalysis compared with conventional adsorption and chemical oxidation process is decomposition or transformation the toxic pollutants to nontoxic forms. There are many metallic compounds as TiO<sub>2</sub>, PbO<sub>2</sub>, SnO<sub>2</sub>, WO<sub>3</sub> and Fe<sub>2</sub>O<sub>3</sub> that sensitize with UV radiation. However, the photocatalysts have recently developed in which TiO<sub>2</sub> due to its chemical stability, relatively low price, non-toxicity and high photocatalytic activity. If emitting high energy radiation, UVC (wavelength band from 200-280 nm), the electron transition with the catalyst is promoted to contribute the photocatalytic reaction. Most PCO technologies are implemented in buildings which can play a significant role in reducing building energy consumption, and in reducing indoor air contaminant level. The PCO process commonly uses nano-semiconductor catalysts and UV light to convert organic compounds in indoor air into benign and odorless constituents (H<sub>2</sub>O and CO<sub>2</sub>) [19].

The UV-PCO technique for air purification is usually implemented under room temperature and pressure, and may be more energy efficient than other techniques, because the semiconductor catalysts are inexpensive and may be capable of oxidizing most



organic compounds effectively [42]. The whole PCO process may be divided into six elemental mass transfer processes occurring in series (Figure 2.5):

- (1) Advection (VOCs and precursor species are carried by air flows)
- (2) External diffusion of reagent species through the boundary layer surrounding the catalyst pellet
- (3) Adsorption onto the catalyst's surface
- (4) Chemical reaction at the catalyst's surface
- (5) Desorption of reaction products
- (6) Boundary layer diffusion of products to the main flow.



**Figure 2.5** Elemental mass transfer process involved in the photocatalytic oxidation of VOCs with a catalyst [42].

Recent advances have been made on the selective photocatalytic transformations on titanium oxide-based photocatalysts both in gas and liquid media. Due to the increasingly stringent environmental limitations for industrial chemical processes, traditional processes employing harmful chemicals and dangerous oxidant/reducing agents with concomitant formation of large amount of harmful waste must be altered to environmentally benign processes. Heterogeneous photocatalytic systems with recyclable catalysts and without the used emission of harmful chemicals/wastes have significant advantages. Titanium oxide based photocatalysts have a great potential as a versatile tool in “green” organic synthesis. Several photocatalytic reactions proceed highly efficiently and selectively on the titanium oxide-based photocatalysts. Photocatalytic transformations hold significant promise for the development of economically and environmentally friendly synthesis processes. Most of the photocatalytic reactions performed so far are oxidation or reductions, and some coupling reactions are also proposed. In the oxidation reactions, aromatics, hydrocarbons, and halogenated aromatics are often used as a substrate. The  $\cdot\text{OH}$  radicals of  $\text{TiO}_2$  react



efficiently with the well-adsorbed aromatic compounds [32]. The conversion of alkanes to oxygenate, such as alcohols, ketones, aldehydes, and carboxylic acids with  $O_2$  is significantly important in the chemical industry. Photocatalytic conversion of alkanes to oxygenate with  $TiO_2$  has been studied extensively.

## 2.3 Thin film deposition technique

The coating technique can be classified as physical vapour deposition (PVD) and chemical vapour deposition (CVD). Physical vapour deposition (PVD) is fundamentally a vaporisation coating technique involving the transfer of material on an atomic level. It is an alternative process to electroplating. The process is similar to chemical vapour deposition (CVD) except that the raw materials/precursors, i.e. the material that is going to be deposited starts out in solid form, whereas in CVD, the precursors are introduced to the reaction chamber in the gaseous state [52].

### 2.3.1 Physical vapor deposition (PVD)

PVD is a variety of vacuum deposition, and is a general term used to describe any of a variety of methods to deposit thin films by the condensation of a vaporized form of the material onto various surfaces (e.g. onto semiconductor wafers). The coating method involves purely physical processes, such as high temperature vacuum evaporation or plasma sputter bombardment rather than involving a chemical reaction at the surface to be coated as in chemical vapor deposition. Variants of PVD include, in order of increasing novelty:

- Evaporative deposition: In which the material to be deposited is heated to a high vapor pressure by electrically resistive heating in a "low" vacuum.
- Electron beam physical vapor deposition: In which the material to be deposited is heated to a high vapor pressure by electron bombardment in a "high" vacuum.
- Sputter deposition: In which a glow plasma discharge (usually localized around the "target" by a magnet) bombards the material, sputtering some away as a vapor. PVD Animation is an animation of a generic PVD sputter tool.
- Cathodic Arc Deposition: In which a high power arc directed at the target material blasts away some of it into a vapor.

- Pulsed laser deposition: In which a high power laser ablates material from the target into a vapor.

PVD is used in the manufacture of items, including semiconductor devices, aluminized PET film for balloons and snack bags, and coated cutting tools for metalworking. Besides PVD tools for fabrication, special smaller tools mainly for scientific purposes have been developed. They mainly serve the purpose of extreme thin films like atomic layers and are used mostly for small substrates. A good example is mini e-beam evaporators which can deposit monolayers of virtually all materials with melting points up to 3500 °C. The use of such coatings is aimed at improving efficiency through improved performance and longer component life. They may also allow coated components to operate in environments that the uncoated component would not otherwise have been able to perform

*Disadvantages of the physical vapor deposition process*

- It is a line-of-sight technique meaning that it is extremely difficult to coat undercuts and similar surface features
- High capital costs
- Some processes operate at high vacuums and temperatures requiring skilled operators
- Processes requiring large amounts of heat require appropriate cooling systems
- The rate of coating deposition is usually quite slow

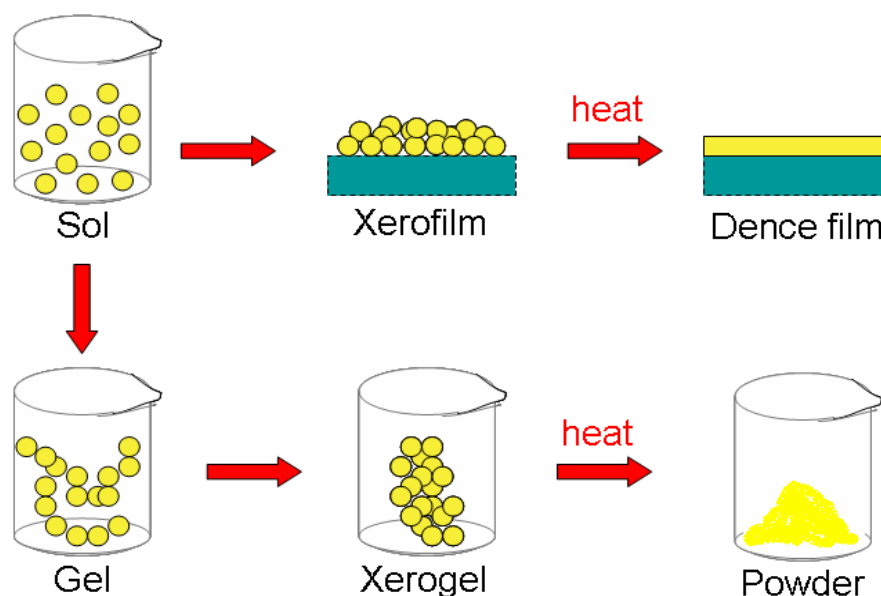
### 2.3.2 Chemical vapor deposition (CVD)

CVD is a method by which a thermally activated chemical reaction occurs from the vapor gas phase depositing a solid thin film. The properties of the coating are controlled by process parameters such as temperature, pressure, flow rates, and input concentrations. The deposition of film by CVD is much more complex than other techniques. It required a chemical reaction that generally includes multicomponent species with the possibility of forming several intermediate products. CVD has become a very important and popular technique for thin film. Due to this technique has the advantages of chemical reaction which easily deposits on substrate and very high purity and dense. Otherwise, it preferred deposition method by needed high temperature for many of the reactions [52].

## 2.4 Synthesis of TiO<sub>2</sub> by microwave assisted sol-gel technique

The synthesis processes to TiO<sub>2</sub> are several methods such as electro-deposition, chemical- or physical vapour deposition, hydrothermal, ultrasound and sol-gel processes [53, 54]. Among all techniques, the sol–gel approach based on the controlled hydrolysis and condensation of appropriate precursors, mostly titanium alkoxides or chlorides, is of particular interest, because it gives a very good compositional and morphological control over the product properties, such as specific surface area, nanoparticle size, degree of aggregation, etc.

Sol-gel processing is commonly used to synthesize oxide materials to thin film. Indeed, the sol-gel process is an alternative to chemical preparation which applied to a substrate by spinning, dipping or draining [55]. The process of sol-gel involves a rigid two-phase system is not reversible. The first step is choosing the right reagents such as silica form of tetraethyorthosilicate (TEOS), which can reacts slowly with water, comes to equilibrium as a complex silanol. The other ingredients are ethanol and water, then the chemical reactions of hydrolyzation and polymerization begins to form siloxane groups. In the system, the sol-gel transition is reached when the one-phase liquid become a two-phase alcogel (i.e., solid plus liquid). Once through the sol-gel transition, the solvent phase is removed by ordinary evaporation while the coating is on substrate. If the substrate has been handled properly, a tackey gel covers the surface uniformly. In addition, the advantages of the sol-gel process are high purity, homogeneity, and low temperature. Because the mixing is accomplished in solution, components mix on the atomic scale in relatively short times. When considering the sol-gel coating, it was found that calcinations at high temperature are necessarily used in the process, according to the specific substrate type. The mechanism path way of sol-gel process to prepare thin film is shown in Figure 2.6.



**Figure 2.6** Thin film preparation by the sol-gel method.

The sol-gel processing is typically required for heating to high temperatures, and so the processes are time consuming [56]. Microwave assisted sol-gel has proven to be a promising method for  $\text{TiO}_2$  synthesis. This is due to the microwave technique can offer a faster and more convenient to prepare nanocrystalline  $\text{TiO}_2$ , rather than use the traditional hydrothermal method, which requires longer synthesis time [27]. Microwave irradiation can promote nucleation of titania crystals, by providing homogeneous heating in a short time, and thus reduce energy costs [26, 28].

Microwave technique is applied for chemistry preparation to substitute for a conventional heating furnace. The microwave technique has been extended as one of hydrothermal processes for synthesis of fine oxide powders. Microwave is absorbed directly into solvent having large dielectric loss like water, and enables the rapid heating compared to a conventional heating process in which the container is heated from the outside. The short-time reaction is preferable for efficient industrial production because the long-time reaction consumes more energy. In addition, the most noteworthy phenomenon by microwave irradiation is the selective heating of high-dielectric media, especially water. Its benefit over traditional ovens include reaction rate acceleration, milder reaction conditions, higher chemical yield, lower energy usage and different reaction selectivity, becoming one of the most interesting technique at present [57]. It can be expected that the microwave field energy will be converted to heat by different amounts of the system

domains. Strong agitation, provided by the reorientation of molecules in phase with the electrical field excitation, causes an intense internal heating. Any polar molecule ( $\text{H}_2\text{O}$ ) is the target of microwave technique, because it absorbs the microwave irradiation which forces to rotate with the field and energy in collisions. Noteworthy, photocatalyst preparation by microwave technique is now applying to assist by suppressing the requirement of heating process at high temperature [27]. Microwave irradiation has been used to prepare  $\text{TiO}_2$  photocatalyst widely and acceptable to instead of the traditional heating step. Microwave processing can lead to the following positive effects in terms of material processing:

- Reduced process times
- Reduced energy consumption
- Improved product homogeneity
- Improved matrix-fibre interfacial strength
- Improved mechanical properties

## 2.5 Mesoporous molecular sieve MCM-41

Mesoporous silica also has been receiving a lot of attention. Regularly-oriented mesopores from a sol-gel process using the self-assembly of organic surfactants as the template. The sol-gel process using metal alkoxides is useful to achieve homogeneous distribution of the second component into Si-O network. Inada *et al.* (2008) studied the process factors on formation of  $\text{SiO}_2\text{-TiO}_2$  mesoporous materials from Si and Ti alkoxides. They found that the way for homogenization is the partial hydrolysis of Si alkoxide before the addition of Ti alkoxide. Homogeneous  $\text{SiO}_2\text{-TiO}_2$  mesoporous materials were synthesized by using acetylacetone as capping agent of Ti alkoxide to inhibit the separate deposition of  $\text{TiO}_2$  [58]. At recent years, mesoporous silica has become to apply with the photocatalytic reaction of  $\text{TiO}_2$  particle embedded in used, especially, to react with volatile organic compounds (VOCs), aromatic molecule, such as BTEX groups. The porous photocatalyst with very high adsorptive capacity enhanced the subsequent photocatalysis reactions and lead to a positive synergistic effect. Contained  $\text{TiO}_2\text{-SiO}_2$  with higher surface area ( $421.1 \text{ m}^2 \text{ g}^{-1}$ ) can achieve 100% conversion efficiency. The higher surface area indicates a more porous material, and leads to higher conversion efficiency [32].

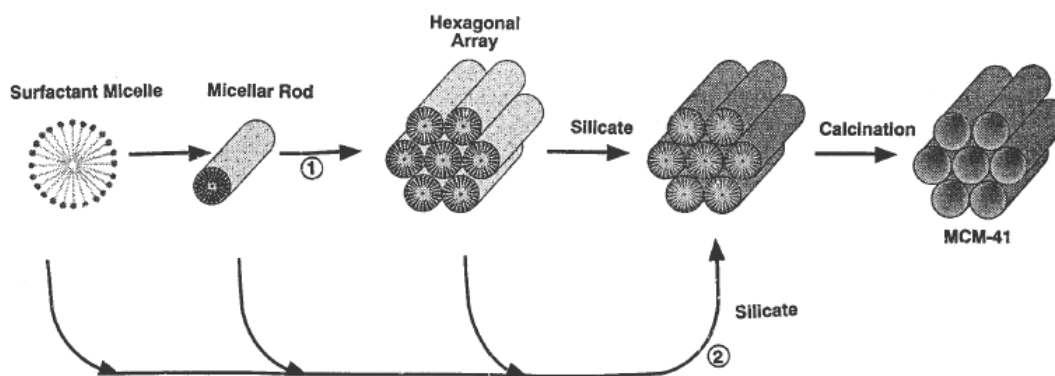
### 2.5.1 History of MCM-41

Porous materials have been used in various applications as catalysts, adsorbents, separation materials and other industrial applications. The large surface areas of these materials enhance their catalytic, sorptive, and separation activities. According to International Union of Pure and Applied Chemistry (IUPAC) definition, based on pore width, three types of pore can be present in a porous solid: micropore ( $< 2$  nm), mesopore (2-50 nm) and macropore ( $> 50$  nm). Microporous materials, such as zeolites and related materials are extensively used in the petrochemical industry as heterogeneous catalysts in cracking and other applications. Micro/mesoporous materials and mesoporous materials (e.g. silica gels, porous glasses, MCM-41, and active carbon) are widely used in separation processes, catalysis, and adsorption. The successful performance of the adsorption unitary operation in industry and pollution abatement requires a comprehensive characterization of these porous materials with regard to micropore volume, surface area, and pore size distribution [59].

In 1992, researchers at Mobil Research and Development Corporation reported the synthesis of a new family of silicate/aluminosilicate mesoporous materials (M41S) possesses a regular hexagonal array of uniform pore openings with a broad spectrum of pore diameters between 1.5 to 10 nm. The mesoporous structure can be regulated by a complex choice of templates (e.g. surfactants, adding auxiliary organic chemicals and changing reaction parameters such as temperature and compositions) [59]. These mesoporous molecular sieves are formed by a liquid crystal templating mechanism. The proposed pathways are illustrated in Figure 2.7.

**Pathway 1:** a rod-shaped micelle formed a hexagonal liquid crystal phase before the additional of silicate species. The porous structure was obtained after removing organic template.

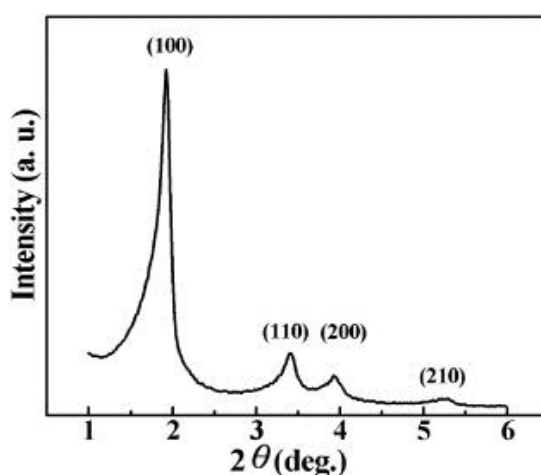
**Pathway 2:** Added to the surfactant solution, the silicate species formed hexagonal silicate skeleton. It was proposed that without the adding silicate the disordered of micelles were occurred. By adding excess surfactant, highly ordered hexagonal structure was occurred due to bonding between micelle and silicate bonding.



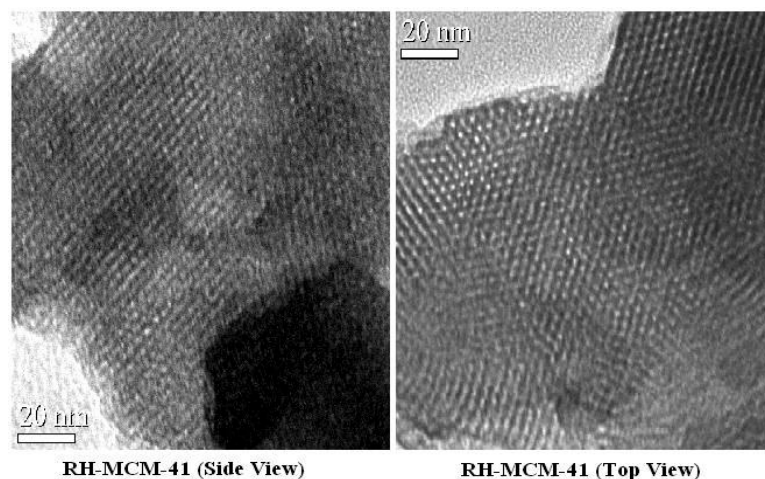
**Figure 2.7** Mechanistic pathway of MCM-41: (1) liquid crystal phase, (2) silicate anion [59].

### 2.5.2 Characterizations of MCM-41

Examination of the sample by X-ray diffraction and transmission electron microscopy (TEM) are the essential characterization techniques to identify the mesoporous characteristics of MCM-41 materials. X-ray diffraction pattern of MCM-41 structures in Figure 2.8 shows a typical four-peak pattern with a very strong peak at a low angle ( $d_{100}$  reflection line) and three weaker peaks at higher angle ( $110$ ,  $200$ , and  $210$  reflection lines). X-ray diffraction technique is used to identify the structure, phase purity, degree of crystallinity, unit cell parameters and crystallite size. The uniformly ordered mesostructure channels of MCM-41 can be observed from Transmission electron microscopy (TEM) as shown in Figure 2.9.



**Figure 2.8** Surface analysis of MCM-41 for XRD pattern [60].



**Figure 2.9** Proposed structure of spherical MCM-41 [61].

At present, MCM-41 has been synthesized from rice husk that comprises of 90 wt% of silica. The RH-MCM-41, called the MCM-41 synthesized from rice husk silica was prepared by following the chemical composition ratios of  $1\text{SiO}_2$ :  $1.09\text{NaOH}$ :  $0.13\text{CTAB}$ :  $120\text{H}_2\text{O}$  [62]. The four distinctive peaks of hexagonal structure of XRD diffractogram of RH-MCM-41 were similar to those of the parent MCM-41 reported elsewhere. Its pore diameter, pore volume and surface area were 2.9 nm,  $0.93\text{ cm}^3\text{ g}^{-1}$ , and  $800\text{ m}^2\text{ g}^{-1}$ , respectively. The RH-MCM-41 was tested as a catalyst support in the dechlorination reaction. The degradation rate of chlorinated gases was enhanced more than 70%. Areerob *et al.* (2006) have studied the tailoring of surface polarity of MCM-41 synthesized from rice husk silica and rice husk ash by silylation technique. The samples were silylated with two functional silanes; trimethylchlorosilane (TMCS) and phenyldimethylchlorosilane (PDMS) in order to reduce the surface polarity. After silylation, the degree of hydrophobicity increased up to 83.06% on TMCS-RH-MCM-41, much more than that of TMCS-RHA-MCM-41 (57.97%). The adsorption capacity of benzene on silylated samples (TMCS-RH-MCM-41 and TMCS-RHA-MCM-41) was approximately twice higher than that on the unsilylated samples [61].

MCM-41 can enhance the interaction between  $\text{TiO}_2$  and the transition metal, which directly correlates to photoactivity. The MCM-41 with Ti in the framework was synthesized for the first time in 1993, and later it was found that Ti-MCM-41 could selectively catalyze the oxidation of olefins and cyclo-olefins to epoxides at low temperatures. Ti was mainly located in the silica framework, while no extra-framework



TiO<sub>2</sub> was detected. Titanium atoms in the framework were mainly tetracoordinated and the TiO<sub>4</sub> tetrahedron was not regular, perhaps caused by the larger size of the Ti atom in comparison with that of the Si atom. The calcination forms of Ti-MCM-41 indicated: (1) the presence of isolated Ti species in the framework, (2) predominantly tetrahedral coordination for Ti, along with some dehydrated five- and six-coordinated sites, and (3) Ti sites virtually independent of the framework assembly pathway. Klankaw *et al.* (2012) demonstrated that MCM-41 has a highly ordered hexagonal structure, with large surface area (> 800 m<sup>2</sup> g<sup>-1</sup>), in order to improve the adsorbability of TiO<sub>2</sub> thin film, MCM-41 can enhance the specific surface area of TiO<sub>2</sub> thin film. Moreover, the functional groups of silanol (Si-OH) found in the MCM-41 structure can generate active hydroxyl radicals (<sup>•</sup>OH), which behave as an oxidizing agent and destroy organic pollutants during photocatalytic reactions. However, a blue shift effect occurred with the introduction of a mesoporous silica (MCM-41) to TiO<sub>2</sub> photocatalyst [33].

## 2.6 Crystal size

X-ray diffraction technique is one of the best methods to study crystal forms, calculating from the angles at which diffraction line appear. XRD patterns are used to determine crystal size from the broadening of the diffraction line at half the line of maximum intensity. In 1918, Bragg developed an equation to calculate crystal size from the broadening of a diffraction line at half the line maximum intensity by employing only ordinary principles of optical diffraction and starting from the following equation 2.11, usually called Bragg's equation:

$$n\lambda = 2d \sin \theta \quad (2.11)$$

The use of the equation developed by Bragg, which is considered a simplified version of Scherrer's Equation, is employed in inorganic chemistry to calculate particle size from X-ray patterns (2.2). The equation is as follows:

$$\beta_{hkl} = \frac{0.89\lambda}{L \cos \theta} \quad (2.12)$$

Where  $\beta_{hkl}$  is the broadening of the diffraction line measured at half the line maximum intensity,  $\lambda$  is the X-ray wavelength,  $L$  is the crystal size and  $\theta$  is the diffraction angle. The broadening of a peak is related to the crystal size and to the wavelength  $\lambda$  provided by the equipment use.

## 2.7 Adsorption

The Brunauer, Emmett and Teller (BET) volumetric gas adsorption technique using nitrogen, argon, etc. is a standard method for the determination of the surface areas and pore size distribution of finely divided porous samples. For MCM-41, three well-defined stages may be identified in a nitrogen adsorption-desorption isotherm at 77 K: (i) a slow increase in nitrogen uptake at low relative pressures, corresponding to monolayer-multilayer adsorption on the pore walls, (ii) a steep increase in  $N_2$  adsorption at intermediate relative pressures ( $P/P_o$  range between 0.2 to 0.4) indicating the capillary condensation in mesopores, and (iii) a plateau at high relative pressures associated with multilayer adsorption on the external surface of the crystals [61].

Adsorption isotherms should conventionally be plotted on the basis of relative pressure,  $p/p^0$  (x-axis) versus amount adsorbed expressed as a molar quantity (y-axis) in  $\text{mol g}^{-1}$ . The experimental procedure involves the use of partial pressure where the actual pressure is expressed with respect to the saturation vapor pressure at a constant temperature of adsorption, hence the process is isothermal. Adsorption data may alternatively be expressed in terms of an isobar, which is a variation in uptake with temperature at constant pressure or an isotherm, the change in temperature with pressure at a constant surface coverage [63].

### 2.7.1 Adsorption mechanisms

Depending upon the nature of forces existing between adsorbate molecules and adsorbent, the adsorption can be classified into two types:

#### 2.7.1.1. Physical adsorption (physisorption)

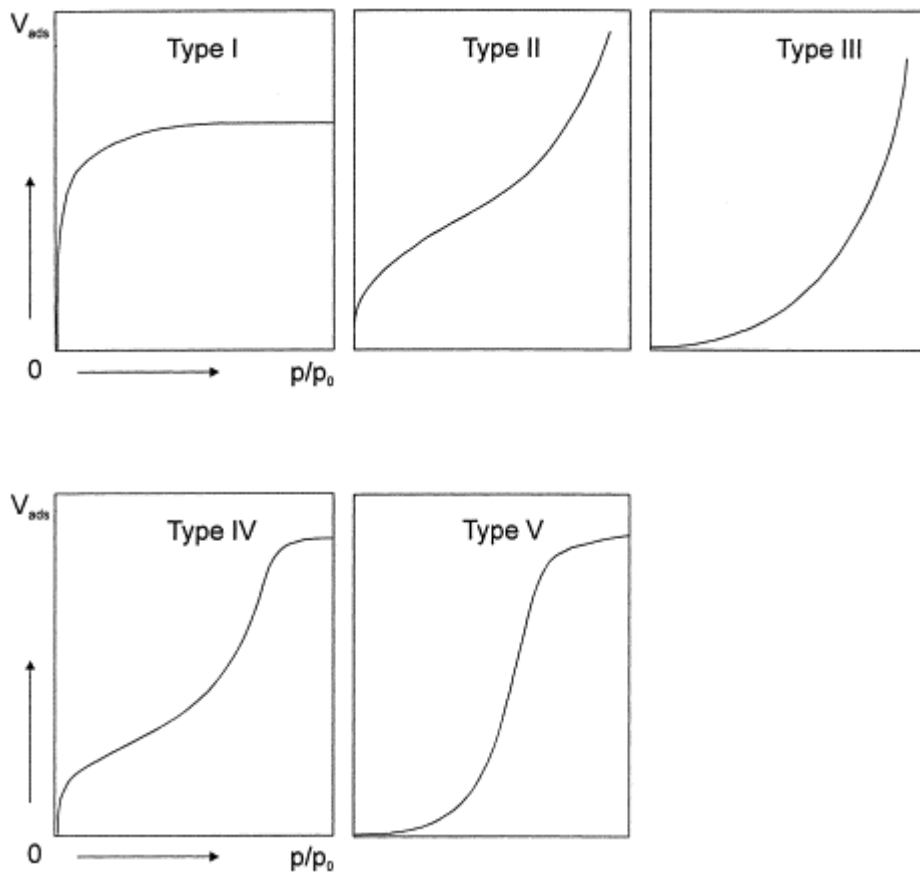
If the force of attraction existing between adsorbate and adsorbent are Vander Waal's forces, the adsorption is called physical adsorption, also known as Vander Waal's adsorption. In physical adsorption, the force of attraction between the adsorbate and adsorbent are very weak, therefore this type of adsorption can be easily reversed by heating or by decreasing the pressure.

### 2.7.1.2 Chemical adsorption (chemisorption)

If the force of attraction existing between adsorbate and adsorbent are almost the same strength as the chemical bonds, the adsorption is called chemical adsorption, also known as Langmuir adsorption. In chemisorption the force of attraction is very strong, therefore adsorption cannot be easily reversed.

### 2.7.2 Type of adsorption isotherms

The majority of isotherms resulting from physical adsorption may conveniently be grouped into five classes, originally proposed by Brunauer, Deming, Deming and Teller (BDDT), sometimes referred to as the Brunauer, Emmett and Teller (BET), or simply, the Brunauer classification. The essential isotherms of these types are shown in Figure 2.10. The isotherms of type IV and type V possess a hysteresis loop and the stepped isotherm [63]. Five different types of adsorption isotherms and their characteristics are explained below.



**Figure 2.10** Adsorption isotherm types defined by Brunauer [63].

**Isotherms of Type I** is a characteristic of a microporous solid. This will result in a distortion of the isotherm, especially at low relative pressures. The estimation of the total micropore volume and the shape of the isotherm were explained in terms of the Langmuir model. Many solids yield Type I isotherms are the xerogels of silica, titania, alumina or stannic oxide.

**Isotherms of Type II** indicates that the solid is non-porous. It is possible in principle to derive a value of the monolayer capacity of the solid to calculate the specific surface of solid. The monolayer capacity is defined as the amount of adsorbate, accommodated in a completely filled or single molecular layer on the surface of unit mass (1 g) of the solid.

**Isotherms of Types III and V** explain a characteristic of weak adsorbent-adsorbate interaction. Type III isotherms are indicative of a non-porous solid or microporous solid. The weak interactions between the adsorbate and the adsorbent lead to low uptakes at low relative pressures but after a molecule become adsorbed at a primary adsorption site. The adsorbate-adsorbate interaction becomes the driving force of the adsorption process, resulting in accelerated uptakes at higher relative pressure.

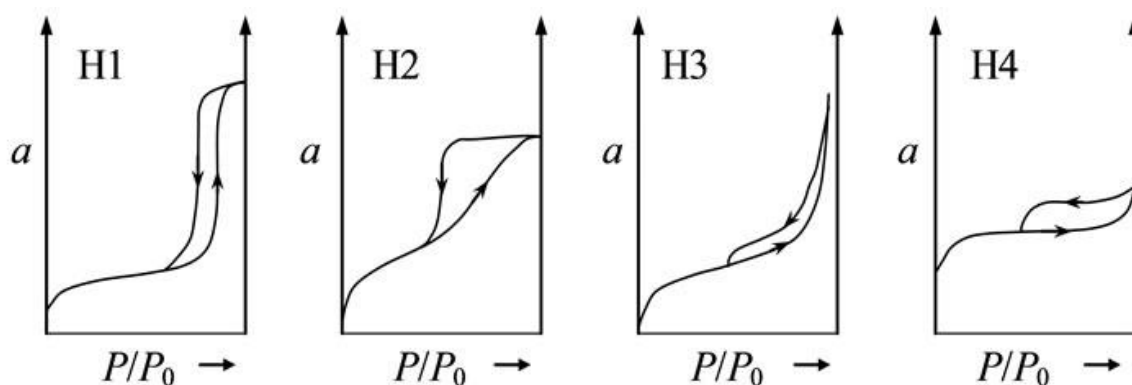
**Isotherms of Type IV** is a characteristic of a mesoporous solid. From this type of isotherm, it is possible to calculate the specific surface area of solid which based on nitrogen adsorption at its boiling point. In Type IV isotherm part, the pore size distribution (PSD) may be also evaluated. A characteristic feature of a Type IV isotherm is its hysteresis loop. The exact shape of the loop varies from one adsorption system to another originally classified by De Boer in 1958 as indicated in Figure 2.10.

**Isotherms of Type V** explain a characteristic of weak adsorbent-adsorbate interaction. These isotherms are the presence of mesoporous or microporous solid porosity, surface area and pores size distribution which originate through the adsorption of either nonpolar or polar molecules.

The behavior of the nitrogen adsorption can be described according to the adsorption condensation theory. When relative pressures  $P/P_0$  are lower than 0.05, nitrogen is adsorbed in the form of single molecules. With an increase in relative pressure, multi-layered adsorption and subsequent capillary condensation occur in some small micropores, which are larger than the pore of monomolecular adsorption, accompanied with increases in the amount of adsorption. A classification of hysteresis loops as recommended in the International Union of Pure and Applied Chemistry (IUPAC) manual consists of the four

types shown in the Figure 2.11. To avoid confusion with the original de Boer classification, the characteristic types are now designated H1, H2, H3 and H4 but it is evident that the first three types correspond to types A, B and E, respectively. It will be noted that H1 and H4 represent extreme types in which the former's adsorption and desorption branches are almost vertical and nearly parallel, whereas in the latter they are nearly horizontal and parallel over a wide range of relative pressure. Types H2 and H3 may be regarded as intermediates between the two extremes.

As pointed out earlier, certain shapes of hysteresis loops are associated with specific pore structures. Thus, type H1 loops are often obtained with agglomerates or compacts of spheroidal particles of fairly uniform size and array. Silica gels tend to give H2 loops, but the distributions of pore size and shape are not well defined. Types H3 and H4 have been obtained with adsorbents having slit-shaped pores or plate-like particles in case of H3. The type I isotherm character associated with H4 is microporosity. Type of H1 hysteresis (e.g. parallel adsorption and desorption branches) is observed for adsorbents such as SBA-15, MCM-41, MCM-48 and controlled pore glass (CPG) due to metastable states associated with pore condensation of a fluid confined to narrow pores.



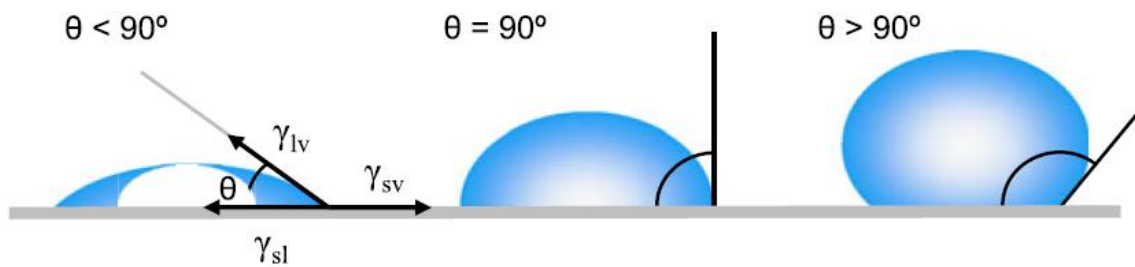
**Figure 2.11** The first four types of hysteresis [64].

## 2.8 Contact angle and wetting property

In recent years, there has been increasing interest in the study of superhydrophobic or superhydrophilic surfaces, due to their potential applications in, for example, self-cleaning, nanofluidics, and electrowetting. Wettability studies usually involve the measurement of contact angles as the primary data, which indicates the degree of wetting

when a solid and a liquid interact. Small contact angles ( $<90^\circ$ ) correspond to high wettability, while large contact angles ( $>90^\circ$ ) correspond to low wettability. Consider a liquid drop resting on a flat, horizontal solid surface. The contact angle is defined as the angle formed by the intersection of the liquid-solid interface and the liquid-vapor interface (geometrically acquired by applying a tangent line from the contact point along the liquid-vapor interface in the droplet profile). The contact angle is defined as the angle formed by the intersection of the liquid-solid interface and the liquid-vapor interface (geometrically acquired by applying a tangent line from the contact point along the liquid-vapor interface in the droplet profile). Figure 2.12 shows a small contact angle that observed when the liquid spreads on the surface, while a large contact angle is observed when the liquid beads on the surface. More specifically, a contact angle less than  $90^\circ$  indicates that wetting of the surface is favorable, and the fluid will spread over a large area on the surface; while contact angles greater than  $90^\circ$  generally means that wetting of the surface is unfavorable so the fluid will minimize its contact with the surface and form a compact liquid droplet.

Machida *et al.* (1999) discovered that when the  $\text{TiO}_2$  thin film was irradiated by ultraviolet ray (UV), the contact angle of water decreased gradually and finally it became almost zero. This phenomenon was called as “super-hydrophilicity” [66]. For super-hydrophobic surfaces, water contact angles are usually greater than  $150^\circ$ , showing almost no contact between the liquid drop and the surface, which can rationalize the “lotus effect”.



**Figure 2.12** Contact angles formed by sessile liquid drops on a solid surface [66].

In practice, the wettability of  $\text{TiO}_2$  coated substrates, such as glass, ceramic tiles and plastic surface, are considered for self-cleaning materials. Much research has reported that the super-hydrophilic behavior of the  $\text{TiO}_2$  coating glass surface leads to the formation of powerful agents with the ability to oxidize and decompose many types of bacteria and organic and inorganic materials [2, 65]. If  $\text{TiO}_2$  film is illuminated by light, grease, dirt and

organic contaminants are decomposed, and can easily be swept away by water (rain), providing useful for traditional building materials.

## CHAPTER 3

### METHODOLOGY

The experiments in this study were separated into three parts: synthesis of TiO<sub>2</sub>/MCM-41, synthesis of Ag/TiO<sub>2</sub>/MCM-41, and photocatalytic testing for environmental applications. The details are described below.

#### 3.1 Materials and instruments

##### 3.1.1 Rice husk

Rice husk was provided from rice mills in Chacheangsao province, Thailand. The purity and elemental composition of the extracted silica were silicon dioxide (SiO<sub>2</sub>) with the high purity content >90 wt%. It was acceptable for using as a silica source for MCM-41 synthesis.

##### 3.1.2 Glass slide plates

Glass microscope slide (75 mm × 25 mm × 1.5 mm) was used as a substrate for photocatalyst film.

##### 3.1.3 Lamps

3.1.3.1 A UV Phillips 15 W germicidal bulb ( $\lambda \sim 254$  nm), with a light intensity of 2.5 W m<sup>-2</sup> was used as light sources for photodecolorization of MB dye.

3.1.3.2 A fluorescent Phillips 15 W bulb, with a light intensity of 1,100 lux was used as light sources for photodecolorization of MB dye and antibacterial testing.

3.1.3.3 Four UV lamps (8W Philips,  $\lambda = 254$  nm, light intensity = 2.17 W m<sup>-2</sup>) or four fluorescent lamps (8 W Philips, cool white 4100 K,  $\lambda = 435$  nm, light intensity = 15,400 lux) were used as UV and visible light sources for photodegradation of gaseous benzene.

##### 3.1.4 *Escherichia coli*

Gram-negative *Escherichia coli* ATCC 8739 used for antibacterial testing was obtained from the Thailand Institute of Scientific and Technological Research TIRSTR 780.



### 3.1.5 Chemical agents

All reagents used in this research were analytical grade.

1. Sodium hydroxide (NaOH 99%, Merck)
2. Nitric acid (HNO<sub>3</sub> 65%, Merck)
3. Hydrochloric acid (HCl 37%, Merck)
4. Ethanol (C<sub>2</sub>H<sub>5</sub>OH 99.8%, Merck)
5. Acetone ((CH<sub>3</sub>)<sub>2</sub>CO 95%, Merck)
6. Hexadecyltrimethylammonium bromide, CTAB (C<sub>19</sub>H<sub>42</sub>BrN ≥96%, Fluka)
7. Titanium(IV) butoxide (Ti(OC<sub>4</sub>H<sub>9</sub>)<sub>4</sub> 97%, Fluka)
8. Acetylacetone (C<sub>5</sub>H<sub>8</sub>O<sub>2</sub> 99%, Merck)
9. Silver nitrate (AgNO<sub>3</sub> 99%, POCH S.A.)
10. Methylene blue (C<sub>16</sub>H<sub>18</sub>N<sub>3</sub>ClS.2H<sub>2</sub>O ≥96%, Unilab)
11. Benzene (C<sub>6</sub>H<sub>6</sub> 99.8%, Analytical grade, PA Panreac)
12. Deionized water

### 3.1.6 Apparatuses

1. Domestic microwave oven (M181GN, maximum 850 W, Samsung)
2. Oven (WOE-105, WIFD)
3. Electronic balance (HB-220, Yamato)
4. Muffle Furnace (JSMF-30T maximum temperature 1200 °C, JSR)
5. Vacuum pump (Rocker 300, Today SC)
6. Magnetic stirrer (MS115, HL Instrument)
7. pH meter (86551, Benchtop meter)
8. Dip coater
9. Hot plate (VELP, Scientifica)
10. UV light meter (UV-340A, Lutron)
11. Lux meter (LX-105, Lutron)
12. Teflon vessel microwave autoclave

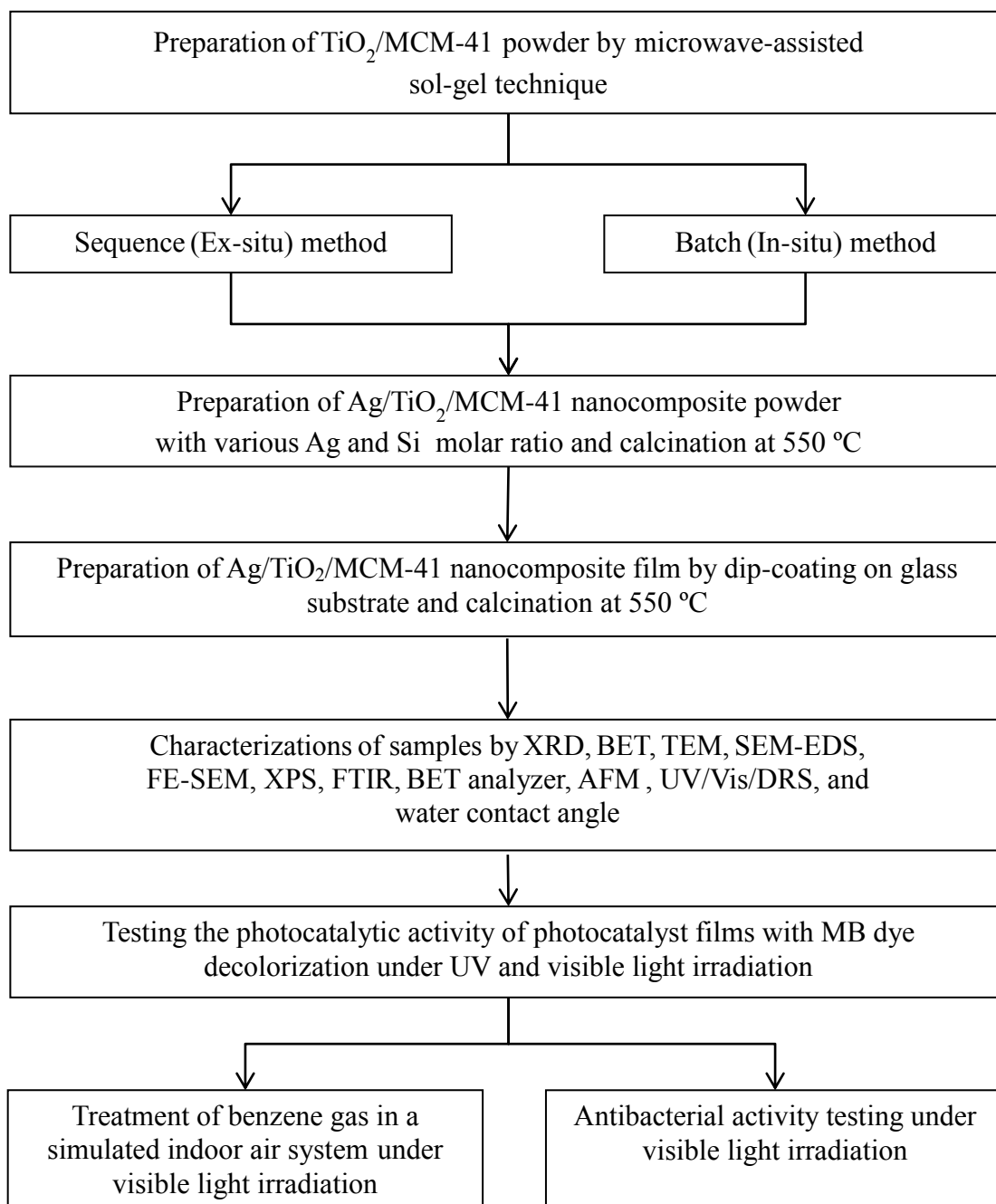
### 3.1.7 Analytical instruments

1. Atomic force microscope (AFM: SPI4000, SEIKO)
2. X-ray diffraction (XRD: D8 Advance with Eulerian Cradle, Bruker)
3. X-ray fluorescence (WD-XRF: PW2400, Philips)

4. Field emission scanning electron microscope (FESEM: S-4800, Hitachi)
5. Fourier transform infrared spectrometer (FTIR: Perkin Elmer, GX)
6. Brunauer-emmett-teller surface analyzer (BET: Autosorb-1 Charantachrome, BEL model)
7. UV-visible diffuse reflectance spectrometer (UV/Vis/DRS: U-4100, Hitachi)
8. UV-visible spectrophotometer (Genesys10-S, Thermo Electron Co.)
9. Transmission electron microscope (TEM: JEM-2100, JEOL)
10. Scanning electron microscope-Energy dispersive X-ray spectroscope (SEM-EDS: JSM-5420LV, JEOL)
11. X-ray photoelectron spectroscopy (XPS: AXIS Ultra DLD, Kratos Analytical Ltd.)
12. Drop shape analyzer
13. Gas chromatography with flame ionize detector (GC/FID: GC-14B, Shimadzu)

### 3.2 Experimental procedures

The experimental procedure is presented as follows:



**Figure 3.1** Experimental diagram.

### 3.2.1 Preparation of extracted silica

1. Rice husk provided from rice fields in central of Thailand was cleaned by water for several times to remove soil and dust.
2. The water-rinse rice husk was introduced to boil in 1 M HCl solution at 80 °C for 1 h.
3. The acid-treated rice husk was rinsed with deionized water until the rinsed water was neutral, then dried at 105 °C for 3 h.
4. Rice husk was calcined in a muffle furnace at 650 °C for 4 h to remove organic impurities.

### 3.2.2 Preparation of MCM-41

MCM-41 was synthesized from rice husk silica with the molar compositions of 1SiO<sub>2</sub>: 1.09 NaOH: 0.13 CTAB: 121.98 H<sub>2</sub>O [62]. The synthesis procedures are as follows:

1. Sodium silicate solution was initially prepared by dissolving 1.88 g of sodium hydroxide in 8 mL of deionized water. 4.32 g of rice husk silica was then added and heated gently until the solution was clear and viscous.
2. 3 g of CTAB was dissolved with 1.14 g of sodium hydroxide in 150 mL of deionized water. The solution was stirred vigorously until homogeneous.
3. The CTAB alkali solution was poured into sodium silicate solution. The mixture was mechanically stirred for 30 min with the synthesis pH controlled at 10. The gel was continuously stirred at room temperature for 48 h.
4. After aging, the suspended solid was filtered through Whatman paper with sieve size No. 48. Then, it was rinsed with ethanol and deionized water and dried at 105 °C. The obtained sample was named “as-synthesized MCM-41”.
5. The as-synthesized MCM-41 was calcined at 550 °C for 5 h under air flow in an electrical furnace. The obtained sample was called “MCM-41”.

### 3.2.3 Preparation of TiO<sub>2</sub>/MCM-41

TiO<sub>2</sub>/MCM-41 was prepared by batch and sequence methods via hydrothermal and microwave assisted sol-gel technique, where the Ti/Si molar ratio was used as 1:1. The batch method was prepared from the chemical mixing of substances into one step (in-situ

method), marked as “B”. The sequence method was prepared from the as-synthesized MCM-41 mixed with titanium precursor solution (ex-situ method) as marked as “S”. The experimental procedures of these two methods are explained as below.

#### 3.2.3.1 Batch method

1. Sodium silicate solution was initially prepared by dissolving 1.88 g of NaOH in 8 mL of deionized water. 4.32 g of rice husk silica was added and heated gently until the solution was clear and viscous.
2. 3 g of CTAB was dissolved in 1.14 g NaOH with 150 mL of deionized water. Then, the solution was stirred vigorously until homogeneous.
3. The CTAB alkali solution was poured into sodium silicate solution. The mixture was mechanically stirred for 30 min with synthesis pH controlling.
4. The titanium precursor was prepared by 24.5 mL of titanium butoxide dissolved in 75.7 mL of ethanol solution, 3.7 mL of acetyl acetone, 2.6 mL of H<sub>2</sub>O and 1 mL of nitric acid 65%.
5. The mixed solution at molar ratio Ti/Si as 1:1 was stirred vigorously at room temperature for 30 min then divided to two portions for microwave irradiation and hydrothermal process.
6. A part of the solution was obtained in a Teflon vessel microwave autoclave and irradiated in a domestic microwave oven to promote a nucleation by irradiation at 100 W for 5 min, while another solution was hydrothermally processed by heating at 80 °C for 24 h.
7. After heating, the sol-gel solution was dried overnight at 80 °C and finally calcined at 550 °C for 5 h to obtain powder samples. These batch samples were denoted according to heating processes and called B-100W, B-450W and B-hydrothermal.

#### 3.2.3.2 Sequence method

1. The as-synthesized MCM-41 powder, prepared as described in section 3.2.2 was added into the titanium precursor solution and stirred vigorously for 1 h until homogeneous and transparent.
2. The mixed sol-gel solution was divided into three portions and placed into a microwave oven at 100 W for 5 min, heating in the oven at 80 °C for 1 h and hydrothermally processed at 80 °C for 48 h.

3. The obtained sol-gel solution was then dried overnight at 80 °C and finally calcined at 550 °C for 5 h in a muffle furnace. These samples were denoted as S-100W, S-heating oven and S-hydrothermal, respectively.

#### 3.2.4 Preparation of Ag doped TiO<sub>2</sub>

An Ag/TiO<sub>2</sub> precursor solution was prepared by mixing titanium butoxide and AgNO<sub>3</sub> in ethanol solution with molar composition of 1Ti(OC<sub>4</sub>H<sub>9</sub>)<sub>4</sub>: 18CH<sub>3</sub>CH<sub>2</sub>OH: 0.5C<sub>5</sub>H<sub>8</sub>O<sub>2</sub>: 2H<sub>2</sub>O: 0.2HNO<sub>3</sub>: 0.1AgNO<sub>3</sub> (10% mol Ag), modified from Hou *et al.* (2008) [67]. The details are described below.

1. 24.5 mL of titanium butoxide was dissolved in 75.7 mL ethanol solution, 3.7 mL of acetyl acetone, 2.6 mL of H<sub>2</sub>O and 1 mL of nitric acid (65%).
2. AgNO<sub>3</sub> with the varying molar ratios of Ag/Ti as 0, 0.01, 0.1 and 0.5 was added into the titanium precursor solution. Then, the mixture was stirred at room temperature for 1 h until dissolved.
3. The Ag doped TiO<sub>2</sub> solution was placed into a microwave oven and irradiated at 100 W for 5 min. The mixed sol-gel was then dried and calcined at 550 °C for 5 h, called “Ag/Ti/Si (0.1/1/0)”.

#### 3.2.5 Preparation of Ag/TiO<sub>2</sub>/MCM-41

The Ag/TiO<sub>2</sub>/MCM-41 sol-gel was synthesized by microwave-assisted sol-gel processes using the sequence synthesis method. TiO<sub>2</sub> precursor was prepared by dissolving titanium butoxide in the mixed solvents (ethanol and acetylacetone). The Ag doped TiO<sub>2</sub> gel was prepared by dissolving AgNO<sub>3</sub> into the TiO<sub>2</sub> precursor. Then, as-synthesized MCM-41 precursor was added to the Ag/TiO<sub>2</sub> precursor solution. The details were described below.

1. The Ag doped TiO<sub>2</sub> precursor solution was prepared by mixing titanium butoxide and AgNO<sub>3</sub> in ethanol solution with molar compositions of Ti(OC<sub>4</sub>H<sub>9</sub>)<sub>4</sub>: 18CH<sub>3</sub>CH<sub>2</sub>OH: 0.5C<sub>5</sub>H<sub>8</sub>O<sub>2</sub>: 2H<sub>2</sub>O: 0.2HNO<sub>3</sub>: xAgNO<sub>3</sub> (where, x = the molar ratio of Ag as 0, 0.01, 0.1 and 0.2).
2. The as-synthesized MCM-41 was then loaded into vigorously stirred Ag doped TiO<sub>2</sub> precursor solutions, with different Si molar ratios. The molar ratios of Si were varied from 0, 0.5, 1 and 2, after processing the various molar ratios of Ag.
3. The mixed sol-gel was stirred at room temperature for 1 h. The pH was measured and recorded at a level of approximately 7±0.5. The microwave

assisted sol-gel method was carried out by irradiating in a domestic microwave at 100 W for 5 min (measured temperature at 75°C).

4. To obtain the nanocomposite powder, the gel was dried and calcined at 550 °C for 5 h with a heating rate of 9 °C min<sup>-1</sup> in a muffle furnace. The nanocomposite films were formed by dipping the gel on glass slides (75 mm × 25 mm) using an automatic coating machine with a draw speed of 10 cm min<sup>-1</sup> for 5 cycles. These samples were denoted as Ag/Ti/Si (x/y/z), according to their different molar ratios. For example, Ag/Ti/Si (0.1/1/0.5) represents a film composition corresponding to 0.1 mol Ag, 1.0 mol Ti and 0.5 mol Si.

### 3.2.6 Characterizations

The physical and chemical properties of samples in the forms of powder and film were characterized by instruments as follows.

#### 3.2.6.1 X-ray Diffraction (XRD)

The crystallinity structures of the powder samples were analyzed by XRD spectrometer (D8 Advance with Eulerian Cradle; Bruker) with CuK $\alpha$  40kV, 40 mA. The scanning is performed at 2 $\theta$  radiation in regular range from 1° to 8° for MCM-41, and 20° to 70° for TiO<sub>2</sub> and Ag. For film characterization, the XRD patterns were analyzed in the range of 20° to 50° by Rigaku TTRAX III using Cu K $\alpha$  radiation at a voltage of 50 kV with speed time of 3° min<sup>-1</sup>.

#### 3.2.6.2 X-rays Fluorescence Spectroscopy (XRF)

A qualitative analysis of powder samples was employed by wavelength dispersive X-ray fluorescence (WD-XRF) spectrometer (PW2400, Philips) by using an X-ray source to eject core-shell electrons from an atom to create an excited state. The chemical composition of Si and Ti on the powder samples were recorded in % element and % atomic.

#### 3.2.6.3 Fourier Transform Infrared Spectrometer (FTIR)

The functional groups of Ag and MCM-41 doped TiO<sub>2</sub> thin film were studied by using FTIR (Perkin Elmer, GX). One milligram of sample was mixed with 100 mg of KBr and ground. Then sample was pressed to make the pellets at 10 N m<sup>-2</sup>. The wavenumber was scanned in the region of 450 to 4000 cm<sup>-1</sup>.

#### 3.2.6.4 Transmission electron microscope (TEM)

The inner constructible properties of powder particles, such as pore size diameter, pore distribution and crystallite size were performed with TEM (JEM-2100, JEOL) at voltages up to 200 kV.

#### 3.2.6.5 Scanning electron microscope-Energy dispersive X-ray spectroscopy (SEM-EDS)

Morphological image and chemical composition of Ti/MCM-41 powder were determined from scanning electron microscope-energy dispersive X-ray spectroscopy (SEM-EDS: JSM-5420LV, JOEL).

#### 3.2.6.6 Brunauer-Emmett-Teller surface analyzer (BET)

The porosity of these samples was measured by N<sub>2</sub> gas adsorption-desorption isotherms at 77 K analyzed with surface analyzer (Autosorb-1 chrantachrome, BEL model). The sample, weighing about 0.1000 g, was degassed to remove moisture and contaminants under nitrogen gas flow at 150°C for 3 h. The specific surface area was calculated following Brunauer Emmett Teller (BET) technique and the pore size distribution was measured by the Barrett-Joyner-Halenda (BJH) method. The total pore volume was obtained from the maximum amount of nitrogen gas adsorbed at partial pressure ( $P/P_0 = 0.999$ ).

#### 3.2.6.7 Field Emission Scanning Electron microscope (FESEM)

The thickness and surface morphology of the photocatalyst films were characterized using field emission scanning electron microscope (FESEM: S-4800, Hitachi) with a  $\times 100,000$  magnification.

#### 3.2.6.8 Atomic force microscope (AFM)

The surface imaging and the Root Mean Square (RMS) roughness of films were measured using an atomic force microscope (AFM: SPI4000, SEIKO). The RMS roughness values were estimated by spectral analysis on 1  $\mu\text{m}^2$  area and scan speed of 0.50 Hz. The roughness of the nanocomposite films is evaluated by RMS average of the roughnesses.

#### 3.2.6.9 X-ray photo-electron spectroscopy (XPS)

The binding energy of the elements was analyzed based on the survey spectrum and scanning at high resolution of Ag3d, O1s, Ti2p and Si2p. (XPS: AXIS Ultra DLD, Kratos Analytical Ltd.). The binding energy scale was calibrated with respect to C1s peak at 285.0 eV.)



### 3.2.6.10 UV-visible diffuse reflectance spectrometer (UV-Vis-DRS)

The UV-visible absorption spectra was measured with a spectrometer (U-4100, Hitachi) equipped with a diffuse-reflectance accessory of solid (powder and film) samples in the region of 250-700 nm.

### 3.2.6.11 UV-visible spectrophotometer

The UV-visible spectrophotometer (Genesys10-S, Thermo Electron Cooperation) was used to determine the absorbance of methylene blue dye at wavelength of 663 nm.

### 3.2.6.12 Gas chromatography-flame ionization detector (GC/FID)

The sampling gas was taken for detection by a gas chromatography-flame ionization detector (GC/FID-14B, Shimadzu) using a Rtx-502.2 capillary column. The injection temperature of 100 °C, column temperature of 100 °C and detection temperature of 150 °C were set up for GC analysis.

### 3.2.6.13 Contact angle measurement

The contact angle is commonly used to describe the relative hydrophobicity/hydrophilicity of a material's surface. The contact angle was measured by dropping 1 mL of water onto the film surface. The optical images of water droplet were recorded with camera at interval times. The contact angle ( $\theta$ ) can be determined from the diameter ( $d$ ) and the height ( $h$ ) of the droplet, following equation (3.1).

$$\frac{\theta}{2} = \tan^{-1} \left( \frac{2h}{d} \right) \quad (3.1)$$

## 3.2.7 Photocatalytic treatment of benzene

The Ag/TiO<sub>2</sub>/MCM-41 films obtained from the sequence method were used as photocatalyst films for benzene gas treatment. The experiment was tested into batch system and simulated indoor air process. In a batch system, benzene gas concentration of 100 ppm (159.41 mg m<sup>-3</sup>) was prepared from the analytical benzene reagent (99.7% benzene) and injected with microsyringe in a gas chamber at 25 °C, following equation (2).

$$V_A = \frac{C_B \times MW_A \times V_B}{10 \times \% \times D_A \times 24.5} \quad (3.2)$$

Where

$V_A$  is the volume of benzene in liquid phase ( $\mu\text{L}$ )

$V_B$  is the volume of benzene gas in a chamber (L)

$C_B$  is the concentration of benzene gas in a chamber (ppm)

$MW_A$  is molecular weight of benzene ( $78.11 \text{ g mol}^{-1}$ )

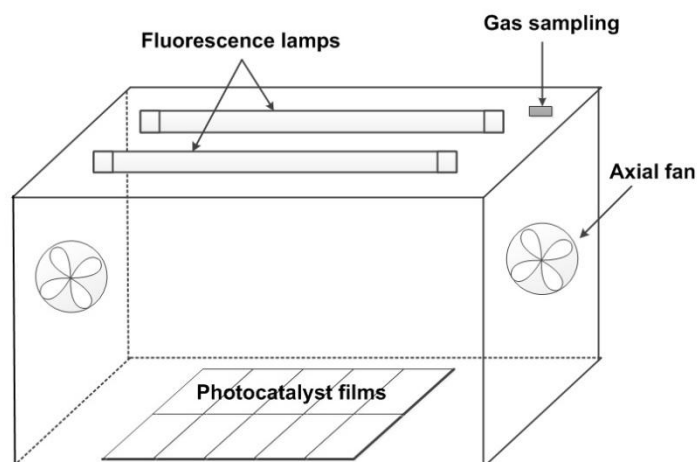
$D_A$  is the density of benzene reagent ( $0.876 \text{ g mL}^{-1}$ ).

% is the purity of benzene reagent (99.7%)

24.5 is the molar volume of gas at  $25^\circ\text{C}$  and 1 atm ( $\text{L mol}^{-1}$ )

### 3.2.7.1 Batch process

The experiment was carried out in a batch reactor that was constructed in a rectangular solid with volume of 10 L ( $23.0 \text{ cm} \times 32.5 \text{ cm} \times 13.5 \text{ cm}$ ). Ten photocatalyst films (total area =  $0.19 \text{ m}^2$ ) were arranged horizontally with light sources. The distance between films and light sources was approximately as 10 cm. The batch reactor was equipped with two 8 W fluorescence lamps and two blowers. 100 ppm of benzene gas was prepared from  $3.6 \mu\text{L}$  of benzene reagent (99.7%) vapory into the batch reactor. Then, the benzene gas was allowed to stand for 1 h in the dark to disperse homogeneously before the photocatalytic degradation. Afterward the lamps were turned on and the 1 mL of gas was collected every 30 min for measuring the remaining concentration of benzene gas by gas chromatography/flameionization detector (GC/FID, Shimadzu GC-14B). The injection temperature of  $100^\circ\text{C}$ , column temperature of  $100^\circ\text{C}$  and detection temperature of  $150^\circ\text{C}$  were set up for GC analysis. The schematic diagram of batch reactor is shown in Figure 3.2.



**Figure 3.2** Schematic diagram of the batch reactor.

The photocatalytic degradation rate of gaseous benzene was calculated according to the following equation:

$$\text{Degradation rate} = \frac{C_0 - C_t}{C_0} \times 100\% \quad (6.1)$$

Where,  $C_0$  and  $C_t$  are the initial concentration and the concentration of benzene gas at irradiation time  $t$  (h), respectively.

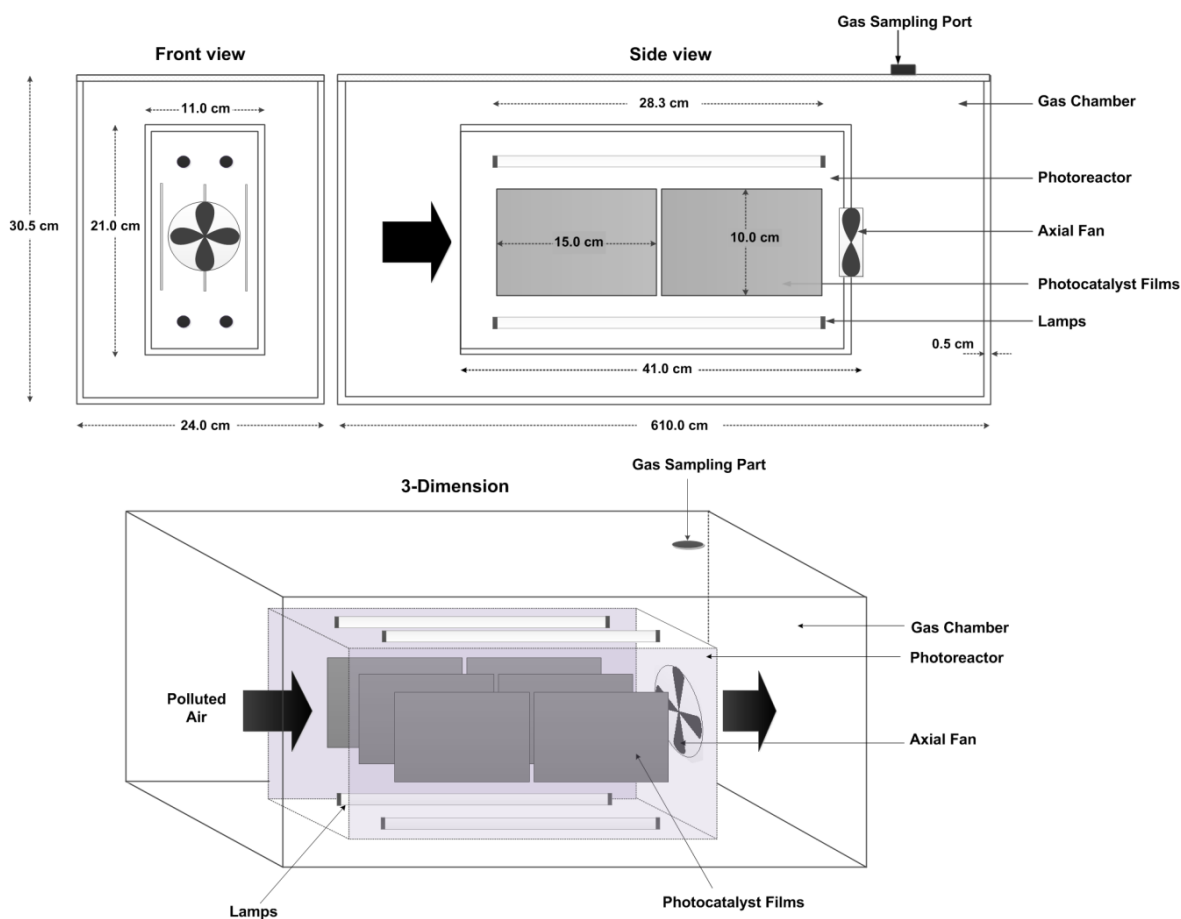
### 3.2.7.2 Simulated indoor air process

The photocatalysis treatment of benzene gas on films was performed in a simulated indoor air system, also known as a semi-batch process, by flowing gas through the photocatalyst films into one direction. The six photocatalyst films of  $\text{TiO}_2$ ,  $\text{Ag/TiO}_2$  or  $\text{Ag/TiO}_2/\text{MCM-41}$  with the size of  $10 \times 15$  cm were placed vertically in the left, middle and right sides of the photoreactor (total active area =  $0.12 \text{ m}^2$ ). Acrylic sheet with thickness of 0.5 cm was constructed to the rectangular solid of gas chamber and photoreactor. The gas chamber was built to the total volume of 40 L ( $22 \text{ cm} \times 60 \text{ cm} \times 30 \text{ cm}$ ). The photoreactor which volume of 8 L ( $10 \text{ cm} \times 40 \text{ cm} \times 20 \text{ cm}$ ) was set into the gas chamber. That is, two lamps were fixed at above and another two lamps were fixed at bottom of the photoreactor. Either four UV lamps (8 W Philips,  $\lambda = 254 \text{ nm}$ , light intensity =  $2.17 \text{ W m}^{-2}$ ) or four fluorescent lamp (8 W Philips, cool white 4100 K,  $\lambda = 435 \text{ nm}$ , light intensity = 15,400 lux) were used as light source. The distance between the films and the light source was set at 5 cm. Benzene gas at concentration of 50 ppm was prepared from the reagent by injection to the gas chamber. The benzene gas was flowed entering through the rectangular photoreactor by axial fan which set at outlet of the photoreactor for air flowing.

The photocatalytic activity of films without lightening condition was first analyzed. One milliliter of a sampling gas was taken three times from gas chamber to detect every 30 min by gas chromatography-flame ionization detector (GC/FID-14B, Shimadzu) using Rtx-502.2 capillary column. The injection temperature of  $100^\circ\text{C}$ , column temperature of  $100^\circ\text{C}$  and detection temperature of  $150^\circ\text{C}$  were set up for GC analysis. Subsequently, the concentration of gas degradation was measured after 1 h. The UV or the fluorescence lamps were turned on for photocatalytic activity of films. The reaction gases were taken

out to measure the concentration changed every 30 min. Figure 3.3 shows the simulated indoor air process which set up and testes for benzene gas treatment on photocatalyst films.

Before starting photocatalytic test, the photocatalyst films were obtained in the photoreactor while all lamps were turned off. After the adsorption of benzene on the film reached its equilibrium, the UV or fluorescence lamps in the chamber were turned on. The change of benzene concentration in the gas chamber was measured by gas chromatography-flame ionization detector (GC/FID-14B, Shimadzu) using Rtx-502.2 capillary column. The photocatalytic rate was studied based on kinetic first order reaction ( $\text{h}^{-1}$ ) and the reaction rates ( $\text{g L}^{-1} \text{h}^{-1}$ ), were calculated, respectively.

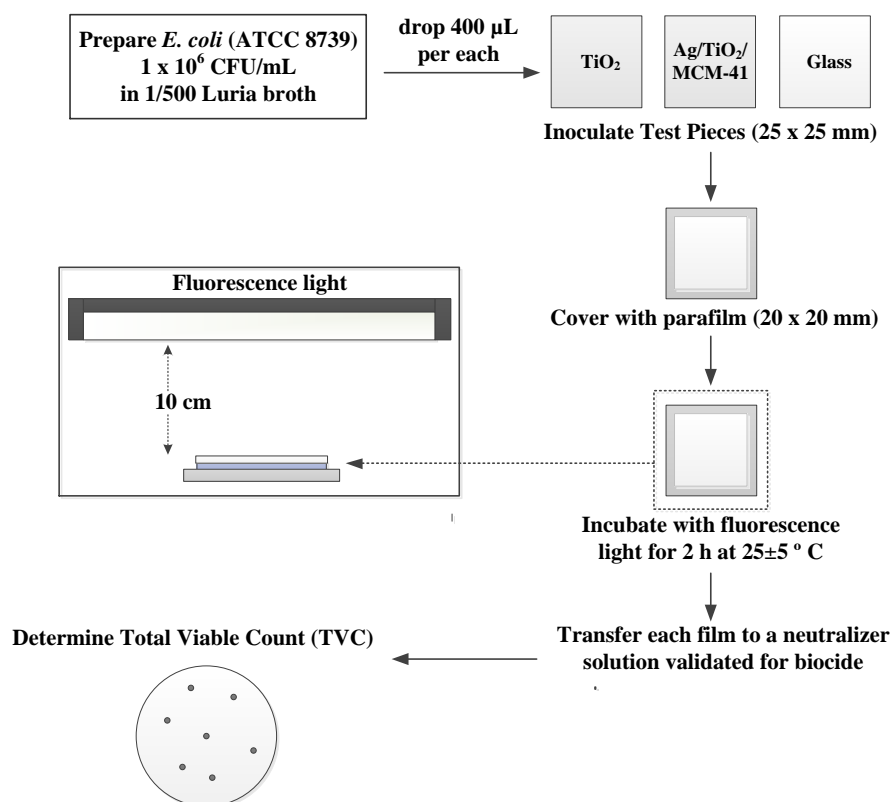


**Figure 3.3** Schematic diagram of the simulated indoor air system.

### 3.2.8 Antibacterial activity

The antibacterial activity of  $\text{TiO}_2$  and  $\text{Ag/TiO}_2/\text{MCM-41}$  photocatalyst films was evaluated by the method modified from the Japanese Industrial Standard JIS Z 2801:2000

method compared to a glass blank [68]. *Escherichia coli* (*E. coli*, ATCC 8739), the gram-negative bacilli, was chosen as the standard bacteria in antimicrobial testing. Firstly, a cell suspension of *E. coli* ( $1 \times 10^6$  CFU mL<sup>-1</sup>) was prepared in 1/500 Luria broth medium. 400 µL of aliquot was dropped onto the test films and the glass blank, which had a test films size if  $25 \times 25$  mm and was covered with parafilm (size as  $20 \times 20$  mm). Next, all samples were incubated under fluorescent light (15 W) at  $25 \pm 5$  °C for 2 h. After incubation, the bacteria was washed out with broth from these films and transferred to individual containers containing an aliquot (10 mL) of a neutraliser validated for the biocide in each film. Finally, 1 mL of each bacteria suspension was spread on a nutrient agar plate and incubated at 37 °C for 24 h followed by counting the surviving bacterial colonies. The numbers of colony forming units within the resulting suspensions were enumerated. This testing was replicated in another two pieces per each sample films. The glass blank was also processed in this manner prior to incubation to provide base-line data. The diagram of antimicrobial testing was described, as shown in Figure 3.4.



**Figure 3.4** Schematic diagram of antibacterial testing on photocatalyst films using modified method from JIS Z 2801: 2000 standard [68].

## CHAPTER 4

### PREPARATION OF TiO<sub>2</sub>/MCM-41 NANOCOMPOSITE POWDER BY MICROWAVE-ASSISTED SOL-GEL TECHNIQUE

#### 4.1 Introduction

Titanium dioxide (TiO<sub>2</sub>) has been widely used as a photocatalyst for environmental applications. However, its low surface area and the limitation of photo-reaction under UV irradiation cause insufficient contact between pollutant and catalyst surface. TiO<sub>2</sub> embedded in mesoporous silica (MPS) is an attractive method to enhance the photocatalytic reactivity of TiO<sub>2</sub> because MPS provides high surface area and abundant hydroxyl groups (OH) [23]. Previous researchers have reported that TiO<sub>2</sub> embedded in mesoporous silica had higher adsorptive capacity leading to a positive effect to photocatalytic reaction [24, 69]. Recently, TiO<sub>2</sub> thin film doped with a mesoporous silica (MCM-41) has been studied, in order to improve the adsorbability of TiO<sub>2</sub> thin film [14]. MCM-41 has a highly ordered hexagonal structure, with large surface area (> 800 m<sup>2</sup> g<sup>-1</sup>), and this can enhance the specific surface area of TiO<sub>2</sub> thin film. Moreover, the functional groups of silanol (Si-OH) found in the MCM-41 structure can generate active hydroxyl radicals (<sup>•</sup>OH), which behave as an oxidizing agent and destroy organic pollutants during photocatalytic reactions [33, 70].

The synthesis method of titanium containing mesoporous MCM-41 nanoparticle is commonly prepared by sol-gel technique. This method can promote the optimal crystal sizes and structures, as well as the phase compositions of TiO<sub>2</sub> nanoparticles. However, the sol-gel method usually involves long reaction time to promote the nucleation and requires high temperature. To overcome these drawbacks, a new preparation of TiO<sub>2</sub>/MCM-41, using a microwave assisted sol-gel technique, has been developed [33]. This method was claimed that microwave can offer a faster and more convenient in preparing nanocrystalline than the traditional hydrothermal method which requires a longer synthesis time [71]. Microwave irradiation can promote nucleation of titania crystal by providing homogeneous and rapid heating which can reduce energy cost [28].

This study aims to apply a microwave assisted sol-gel method to prepare titanium-containing mesoporous MCM-41 by comparing between batch (B) and sequence (S) methods. In addition, the influence of MCM-41 on the photocatalytic reactivity of TiO<sub>2</sub>

was investigated. The photocatalytic reactivity of powder samples was evaluated by photocatalytic decolorization of methylene blue dye under UV irradiation.

## 4.2 Research objectives

4.2.1 To apply a microwave-assisted sol-gel method for the preparation of  $\text{TiO}_2/\text{MCM-41}$  nanoparticles.

4.2.2 To compare the preparation method of  $\text{TiO}_2/\text{MCM-41}$  nanoparticles between batch (B) and sequence (S) methods.

4.2.3 To characterize and study the photocatalytic reactivity of the synthesized  $\text{TiO}_2/\text{MCM-41}$  nanoparticles.

## 4.3 Experimental procedure

$\text{TiO}_2/\text{MCM-41}$  nanoparticles were prepared by batch and sequence methods using microwave-assisted sol-gel technique. Batch method (B) was the method that mixes sodium silicate, titanium precursor and CTAB within a batch system or called “in-situ” method. Sequence method (S) was the method that adds as-synthesized MCM-41 powder into titanium precursor solution or called “ex-situ” method.

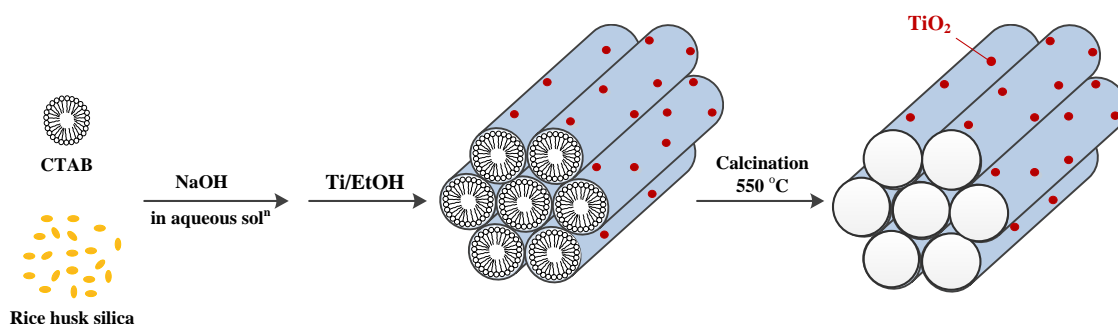
### 4.3.1 Preparation of $\text{TiO}_2/\text{MCM-41}$ from rice husk

Titanium dioxide ( $\text{TiO}_2$ ) was prepared by mixing  $\text{Ti}(\text{OC}_4\text{H}_9)_4$ :  $\text{CH}_3\text{CH}_2\text{OH}$ :  $\text{C}_5\text{H}_8\text{O}_2$ :  $\text{H}_2\text{O}$ :  $\text{HNO}_3$  in a molar ratio of 1:18: 0.5: 2: 0.2. The mixed titanium solution was stirred at room temperature for 30 min, denoted as “titanium precursor solution”. To obtain  $\text{TiO}_2$  particles, the sol-gel solution was dried and calcined at 550 °C for 5 h. For  $\text{TiO}_2/\text{MCM-41}$  preparation, the different methods of batch and sequence methods were compared.

#### 4.3.1.1 Preparation of $\text{TiO}_2/\text{MCM-41}$ by batch method (B)

Sodium silicate solution was prepared by dissolving 4.32 g of silica into 1.88 g of sodium hydroxide and 8 mL of deionized water. The solution was heated gently until it was clear and viscous. Next, 3 g of CTAB was dissolved in 1.14 g of sodium hydroxide and 150 mL of deionized water, then the solution was stirred vigorously until homogeneous. The CTAB alkali solution was poured into the sodium silicate solution and stirred for 30 min. Titanium precursor solution was simultaneously prepared and mixed

with the prepared MCM-41 solution at molar ratio of Ti/Si as 1:1 in a batch system. After the precursor solutions were mixed together under vigorous stirring at room temperature for 30 min, the solution was transferred to a Teflon vessel microwave autoclave and irradiated by microwave at 100 W or 450 W for 5 min. A domestic microwave oven was used to promote a nucleation of samples compared to a traditional hydrothermal heating at 80 °C for 48 h. The obtained slurry was dried at 80 °C for 24 h and calcined at 550 °C for 5 h in a muffle furnace. These batch samples were denoted according to the heating processes as “B-100W”, “B-450W” and “B-hydrothermal”. The schematic diagram of TiO<sub>2</sub>/MCM-41 prepared by the batch method (B) is presented in Figure 4.1.

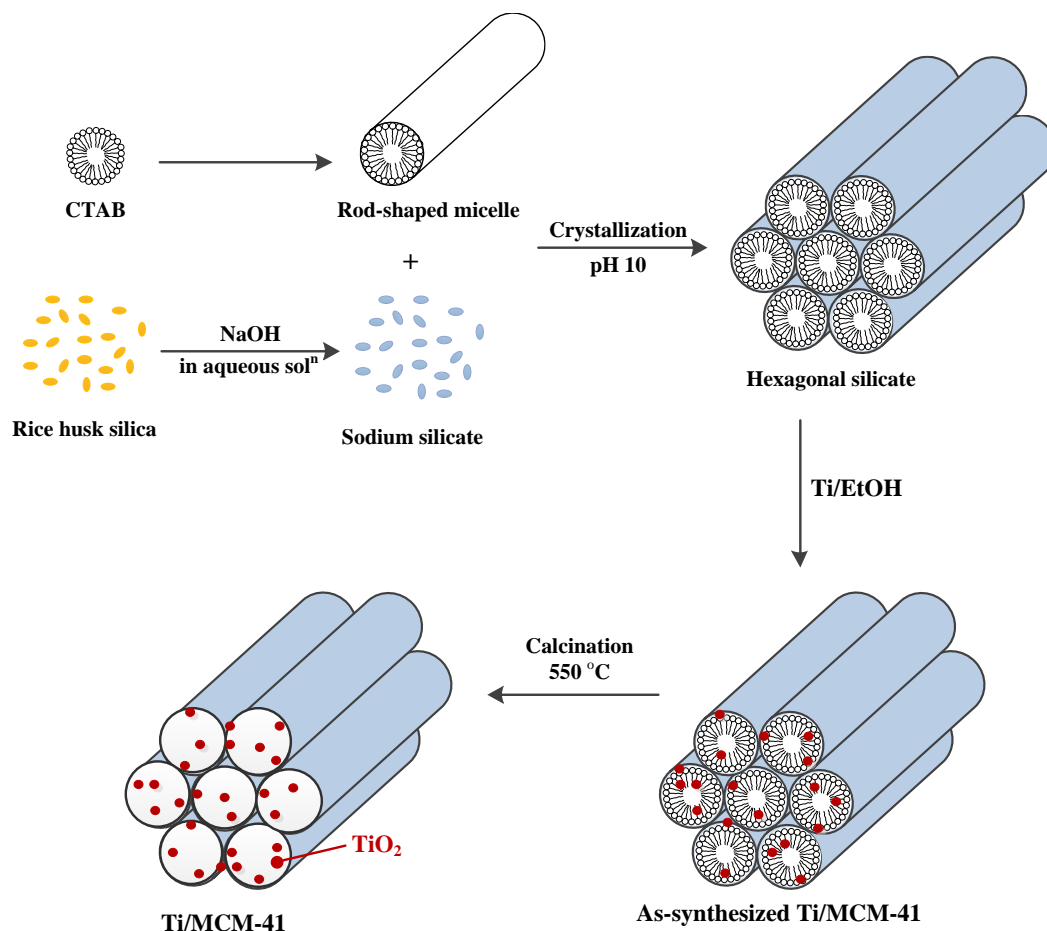


**Figure 4.1** Schematic representation of TiO<sub>2</sub>/MCM-41 prepared by batch method (B).

#### 4.3.1.2 Preparation of TiO<sub>2</sub>/MCM-41 by sequence method (S)

The sequence method was prepared by adding as-synthesized MCM-41 powder into the titanium precursor solution. The sol-gel solution was stirred vigorously and divided into three portions. Each portion was treated with different methods as irradiating at 100 W for 5 min, heating in oven at 80 °C for 1 h, and hydrothermal at 80 °C for 48 h. However, the microwave irradiation at 450 W could not be used in this method because the high wattage microwave heating caused rapid volatilization of organic solvent during irradiation. The mixed sol-gel solution was then dried overnight and calcined at 550 °C for 5 h in a muffle furnace. These samples were denoted according to the heating processes as “S-100W”, “S-heating oven” and “S-hydrothermal”, respectively. The schematic diagram of TiO<sub>2</sub>/MCM-41 prepared by sequence method (S) is presented in Figure 4.2.





**Figure 4.2** Schematic diagram of  $\text{TiO}_2/\text{MCM-41}$  prepared by sequence method (S).

#### 4.3.2 Characterizations

The crystallinity of powder samples was characterized by X-ray diffraction (Miniflex) using  $\text{Cu K}\alpha$  radiation ( $\lambda = 1.5406 \text{ \AA}$ ) at a voltage of 40 kV and 40 mA. The samples were scanned in the range of  $2\theta = 1\text{--}70^\circ$  at a scanning speed of  $2^\circ \text{ min}^{-1}$ . The porosity of these samples was measured by nitrogen gas adsorption-desorption isotherms at 77 K and analyzed with a surface analyzer (Autosorb-1 chrantachrome, BEL model). The specific surface area and pore size distribution were calculated by the Brunauer-Emmet-Teller (BET) method and the Barrett-Joyner-Halenda (BJH) method, respectively. The total pore volume was obtained from the maximum amount of nitrogen gas adsorbed at partial pressure ( $P/P_0 = 0.979$ ). The morphological characterization of powder samples were examined from Transmission electron microscopy (TEM: JEOL-2010) at voltages up to 200 kV and the Scanning electron microscopy-Energy dispersive X-ray spectroscopy

(SEM-EDX: JSM-5420LV, JOEL). The ultraviolet-visible adsorbance spectra were obtained by using a UV-visible diffuse reflectance spectrophotometer (U-3501, Hitachi) with the scanning range of 300-700 nm. Fourier Transform Infrared Spectra (FTIR: Perkin Elmer, GX) is used to identify the functional groups of all samples at scanning in the region of 450 to 4000  $\text{cm}^{-1}$ .

#### 4.3.3 Photocatalytic performance of $\text{TiO}_2/\text{MCM-41}$

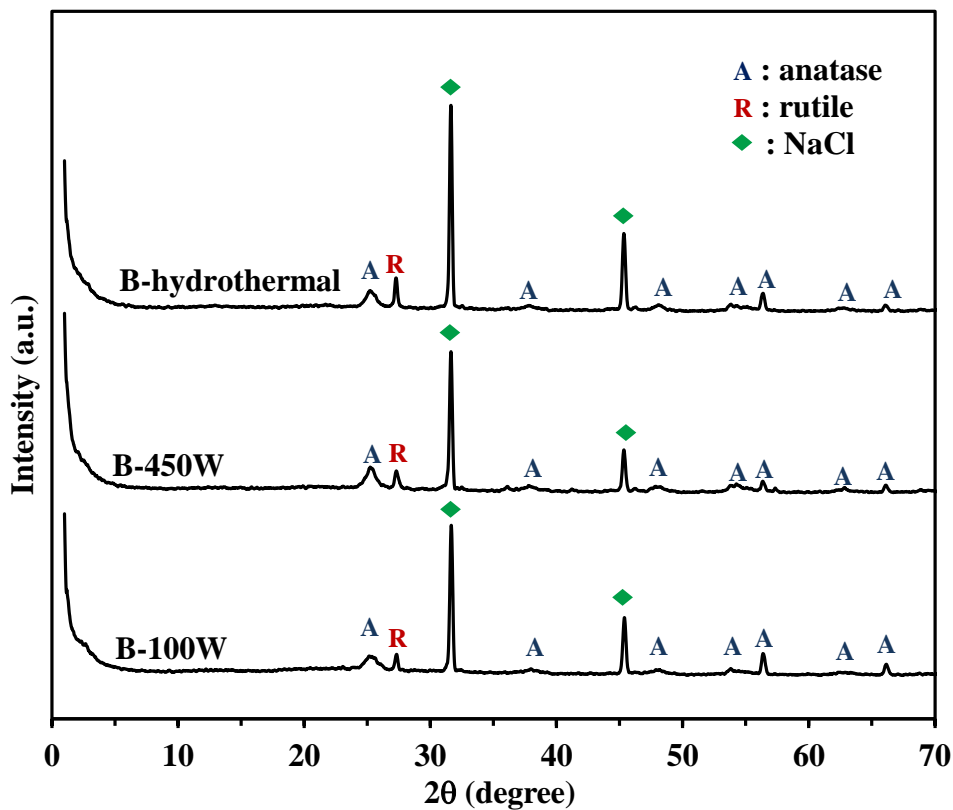
The photocatalytic activity of the powder samples was determined from the decolorization of the methylene blue (MB) dye solution. For each test, 20 mL of  $10^{-5}$  M MB was transferred into the pyrex beaker which contained 0.1 g of powder samples. After that, the photocatalytic activity of samples on MB dye was studied by turning on UV 15 W germicidal lamp,  $\lambda \sim 254$  nm, Philips. The distance of light sources above the solution was set at 15 cm. The UV light intensity above samples determined from the UV light meter was  $2.5 \text{ W m}^{-2}$ . At given irradiation time intervals, 1 mL of MB solution was taken to analyze the absorption intensity by UV-visible spectroscopy (Genesis10 UV) at the wavelength of 663 nm ( $\lambda_{\text{max}}$ ).

### 4.4 Results and discussion

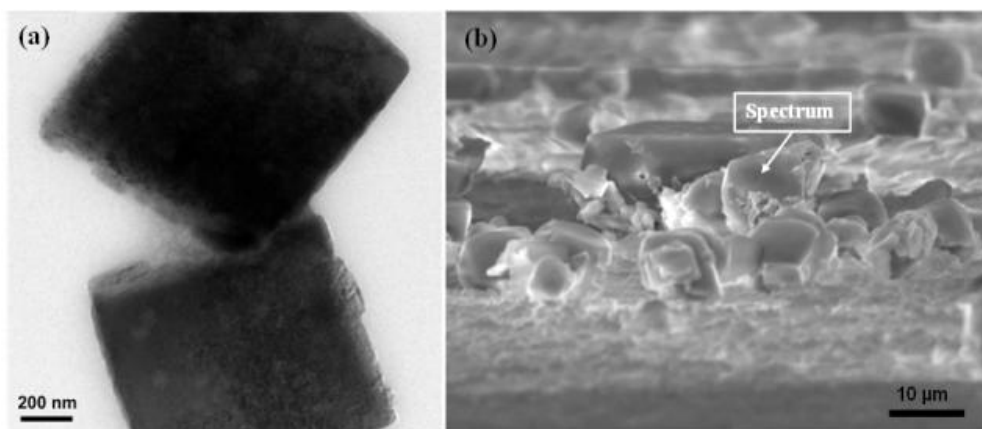
#### 4.4.1 $\text{TiO}_2/\text{MCM-41}$ characterizations

Figure 4.3 shows the wide angle XRD patterns of B samples prepared by different heating processes scanned in the range of  $1^\circ$  to  $70^\circ$ . The diffraction peaks of all B samples exhibit the both characteristics of anatase at  $2\theta$  equal to  $25.3^\circ$  ( $101$ ) and rutile at  $2\theta$  equal to  $27.4^\circ$  ( $110$ ), according to JCPDS No. 21-1272 and JCPDS No. 21-1276. However, the characteristic peak of MCM-41 was not obviously seen. Moreover, the strong diffraction peaks at  $2\theta$  of  $31.3^\circ$  and  $44.8^\circ$  were observed from all B samples. These peaks were assigned to sodium chloride (NaCl) crystal phase of ( $200$ ) and ( $220$ ), respectively [72]. The diffraction pattern of B-hydrothermal exhibits the greater crystallinity of anatase and rutile phases than other samples. This is because the hydrothermal process requires longer heating time (48 h) during crystallization. As a result, the phase transformation of anatase to rutile might be easily occurred. However, microwave irradiation provided both anatase and rutile  $\text{TiO}_2$  phase, comparable to hydrothermal heating. It is noticed that heating with

microwave can reduce crystallization time from 2,880 min to 5 min. Accordingly, the hydrothermal process can be replaced with the microwave irradiation.



**Figure 4.3** XRD patterns of  $\text{TiO}_2/\text{MCM-41}$  synthesized by batch (B) method with the different heating process: hydrothermal reflux and microwave irradiation.



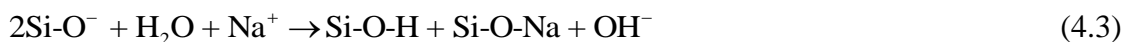
**Figure 4.4** (a) TEM image (magnification  $\times 10,000$ ) and (b) SEM image of Na cubic particles on B-100W sample.

The morphological observations from the TEM and SEM images of the B samples display the cubic particles, as seen in Figure 4.4. The EDX analysis was used to identify the chemical composition of the cubic particles as shown in Table 4.1.

**Table 4.1** Chemical composition of B sample analyzed from EDX.

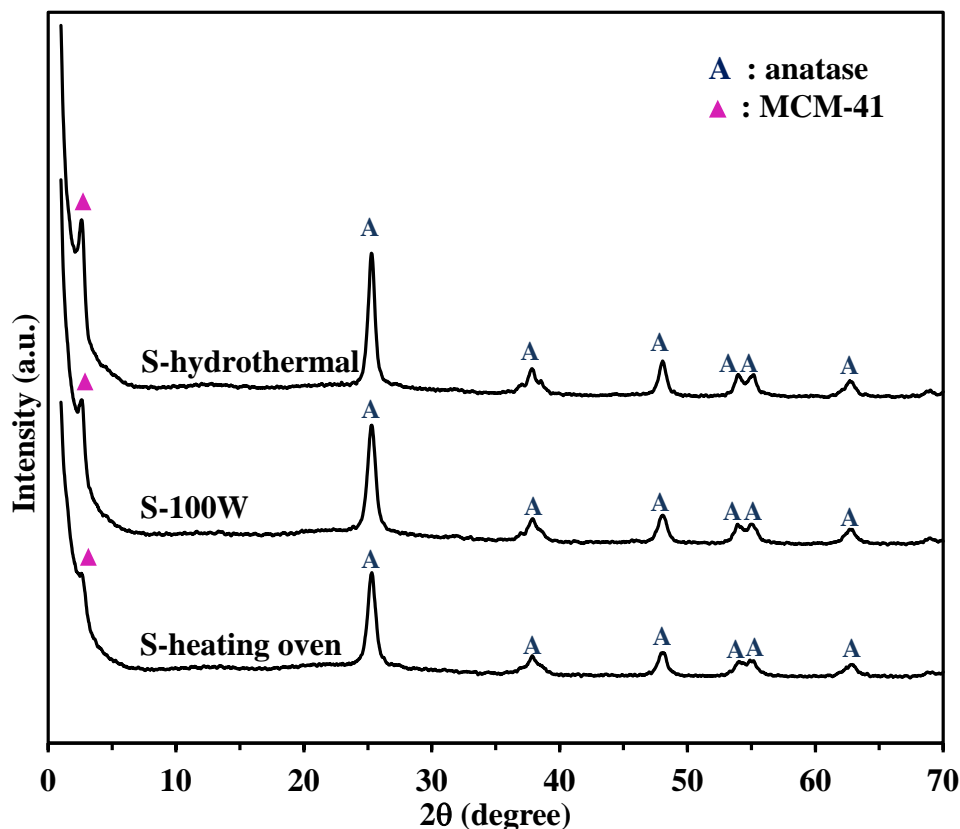
Element	C	O	Na	Mg	Al	Si	Ca	Ti
%Atomic	15.62	59.9	12.65	0.66	0.29	9.38	0.92	0.56

The EDX data confirms that TiO<sub>2</sub>/MCM-41 was contaminated with Na. It is possible that the sodium chloride (NaCl) crystal was able to form. The excess of Na<sup>+</sup> dissolved from NaOH in aqueous solution combines with Cl<sup>-</sup> from HCl. The mechanisms were described as the following equations (4.1-4.4).



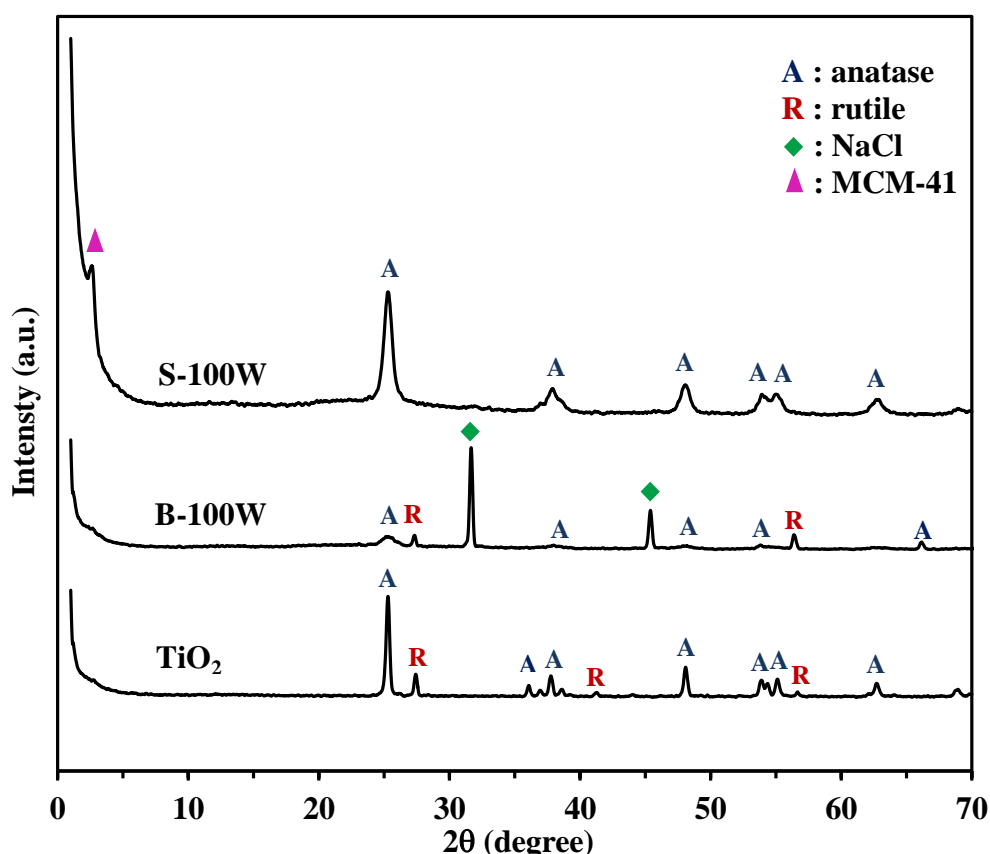
The XRD patterns of the S samples are display in Figure 4.5. The results from all S samples exhibit anatase phase at 2θ of 25.3 ° (101) and MCM-41 crystal phase at 2θ of 2.3° (100), whereas the rutile phase was not observed. The XRD peak intensity of S-heating oven exhibits lower crystal phases than other samples. When compare the XRD peak intensity of S-hydrothermal to that of S-100W samples, the main diffraction peak of MCM-41 prepared by hydrothermal processing has a slightly higher intensity than that of MCM-41 prepared by microwave irradiation because the hydrothermal process requires longer heating time during crystallization. This is in agreement with the previous study [71] that the microwave assisted sol–gel method required shorter crystallization time than the conventional sol–gel methods. The crystallization using microwaves took only 5 min, while the conventional method took 2,880 min. Moreover, the process of the microwave assisted sol–gel technique is simple, convenient and energy cost saving. The electricity

consumption for the microwave method is only 0.008 kWh, while that of the hydrothermal process is 6.5 kWh.



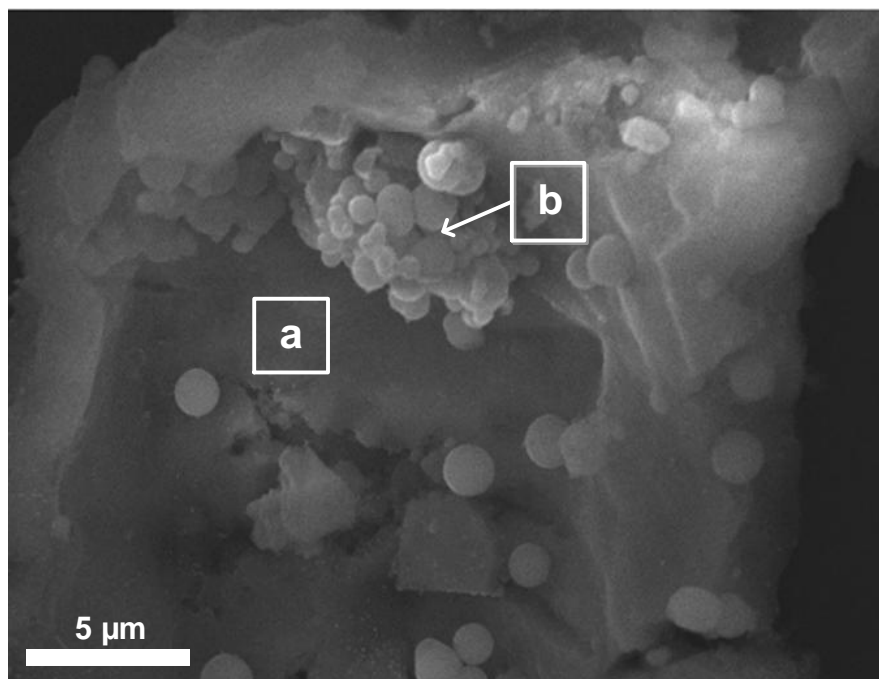
**Figure 4.5** XRD patterns of TiO<sub>2</sub>/MCM-41 nanoparticles synthesized by S method with different heating processes.

The comparison of the XRD patterns of TiO<sub>2</sub>, B-100W and S-100W is shown in Figure 4.6. It was observed that the XRD patterns of TiO<sub>2</sub> and B-100 samples display the characteristic of both anatase and rutile phases indexed at 2θ of 25.3° (101) and 27.5° (110), respectively. Although B-100W indicated anatase TiO<sub>2</sub> crystal, the diffraction peak of MCM-41 at 2θ of 2.4° (100) was not seen. Differently, S-100W exhibited both characteristic of MCM-41 (100) and anatase phase (101). It was explained that the formation of TiO<sub>2</sub> did not distort the formation of MCM-41. Moreover, S-100W method inhibited the transformation of anatase to rutile. Thus, S-100W method was recommended for TiO<sub>2</sub>/MCM-41 synthesis and prevented the crystallization of NaCl.



**Figure 4.6** XRD patterns of different photocatalysts prepared by microwave technique.

The morphological image by the SEM in Figure 4.7 shows the composite phases of the S sample. The chemical composition in % atomic of these phases was identified by EDX analysis as detailed in Table 4.1. The position (a) displays a plate-like particle which consists of O, C and Si as 43.53%, 28.24% and 24.74%, respectively. However, Ti atom was slightly found as only 1.39 %. Thus, it might be implied that the main structure at position (a) was SiO<sub>2</sub>, containing in MCM-41. Moreover, the agglomeration of small and sphere particles was also observed as seen at the position (b). The major atoms found in the sphere particles were O (65.62%), Si (10.72%) and Ti (10.68%). It was noticed that the percentage of Ti atom found in position (b) was increased while the percentage of Si was decreased. This indicates that the sphere particles were mainly formed by crystallization of TiO<sub>2</sub>. However, both positions confirm the coordination of Si, O, and Ti atoms in TiO<sub>2</sub>/MCM-41 prepared by sequence method.



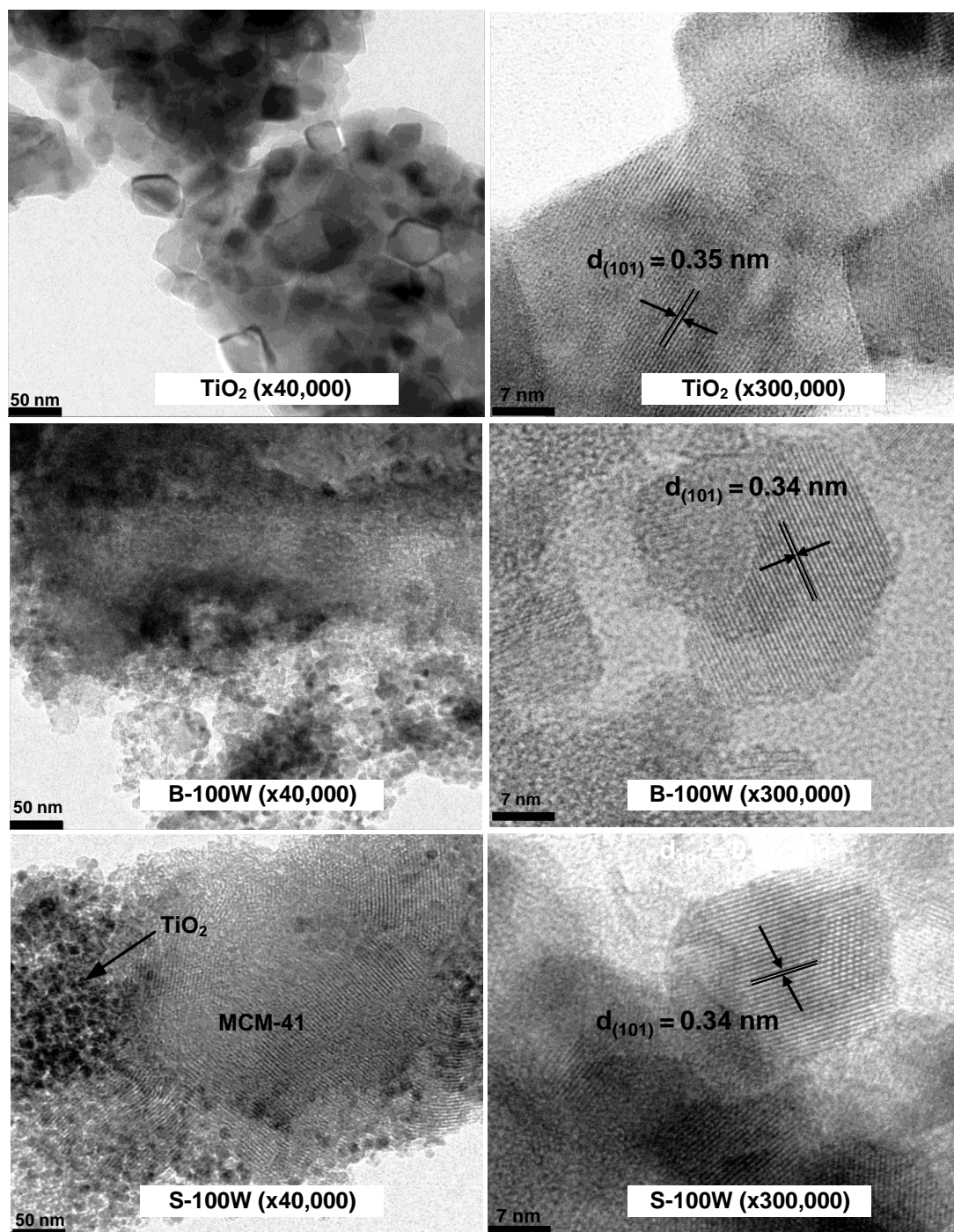
**Figure 4.7** SEM image of S-100W sample.

**Table 4.2** Chemical composition (% atom) of S-100W sample analyzed from EDX.

Position	C	O	Na	Si	S	Cl	Ti	Cu
a	28.24	43.53	1.03	24.74	0.06	1.01	1.39	0.00
b	9.51	65.62	1.89	10.72	0.26	1.22	10.68	0.10

Transmission electron micrographs (TEM) of TiO<sub>2</sub>, B and S samples are illustrated in Figure 4.8. The TEM image of pure TiO<sub>2</sub> nanoparticles with the magnification of 40,000 indicates the octahedral titanium (IV) oxide (TiO<sub>2</sub>) crystallites corresponding to anatase (*101*). The average size of anatase TiO<sub>2</sub> crystallites was in a range of 30 to 50 nm. TEM images of B-100W and S-100W indicated the decreasing of crystal size of TiO<sub>2</sub> particles when corporate with MCM-41. The composite formation of TiO<sub>2</sub> and MCM-41 crystals was obviously seen only from S-100W image. Another evidence is that B-100W did not exhibit the crystal phase of MCM-41. The average lattice distance of anatase (*d*<sub>101</sub>) phase of TiO<sub>2</sub> particle with magnification of 300,000 was 0.35 nm. While, the composite TiO<sub>2</sub>/MCM-41 samples show the decrease of lattice distance from 0.35 to 0.34 nm. This is because the growth of TiO<sub>2</sub> crystallite can suppress the formation of the hexagonal

structure of MCM-41. The effect was strong in the B-100W sample, which was in accordance with the previous XRD results.

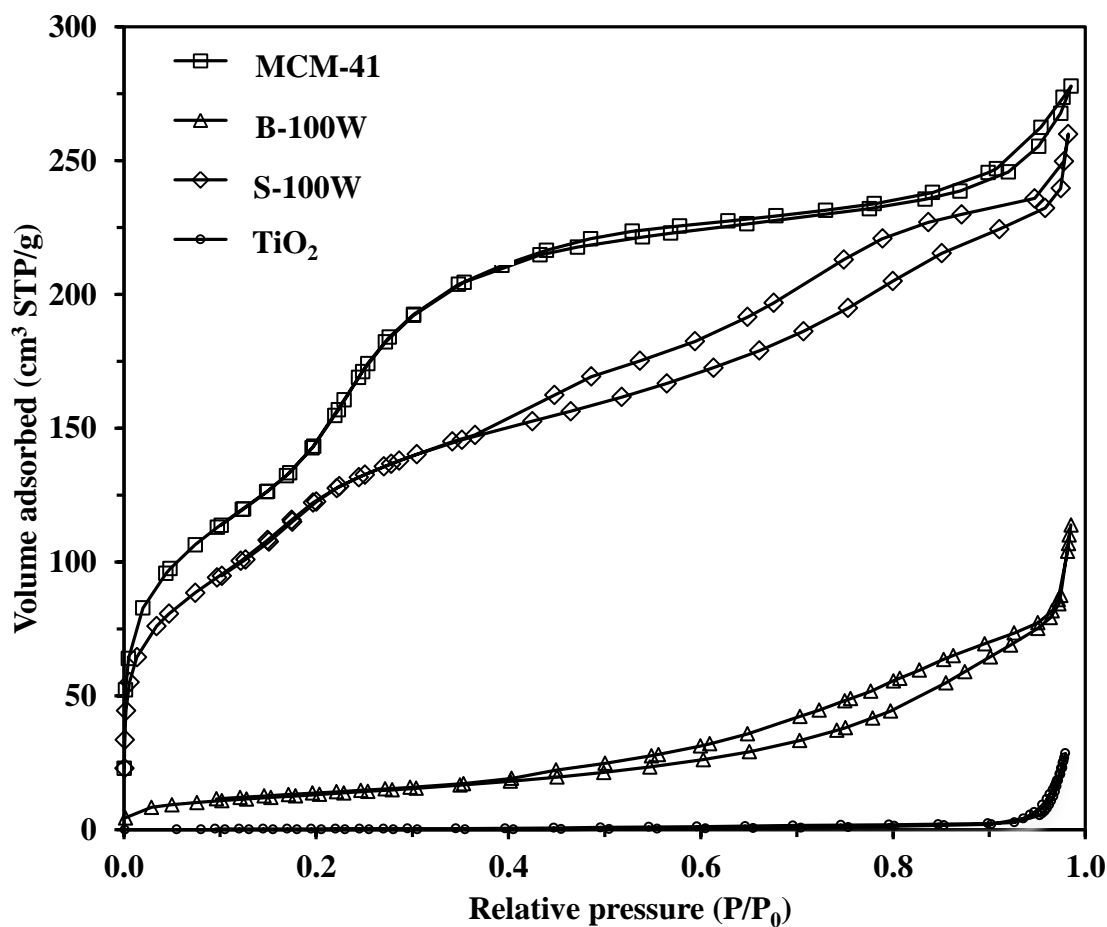


**Figure 4.8** TEM images of TiO<sub>2</sub>, B-100W and S-100W samples with magnification  $\times 40,000$  and  $\times 300,000$ .



The porosity analysis of TiO<sub>2</sub>, B, S and MCM-41 was studied by nitrogen adsorption-desorption isotherms (Figure 4.9). The isotherms of primary MCM-41 and S-100W exhibit type IV, according to IUPAC, with capillary condensation at  $P/P_0$  around 0.2-0.4, indicating the presence of mesopores. It can be seen that the isotherm of MCM-41 sample shows the hysteresis loop (H1 type) at a relative pressure range of 0.4-1.0, exhibiting a narrow distribution of relatively uniform. However, the adsorption isotherm of S-100W shifts downward and the hysteresis loop exhibits H2 type which is characteristic of bottleneck pores and of solids composted by small spherical particles [63]. This result was possibly related to the agglomeration of TiO<sub>2</sub> particle in the pores of MCM-41, which resulted in the decrease of specific surface areas and increase of average pore sizes comparing to MCM-41. The characteristic isotherms of B-100W is type II, indicated the lower adsorption of nitrogen molecule accommodated in a completely filled due to the monolayer capacity on the surface of particles [33, 51]. In addition, the shape of the hysteresis loop for B-100W becomes type H3, suggesting the slit-shaped pores associated with plate-like particles [64]. The nitrogen adsorption-desorption isotherm of TiO<sub>2</sub> particle shows characteristic type III indicated to the weak adsorbent-adsorbate interaction.

Table 4.2 summarizes the adsorbability results using BJH cumulative pore diameter, specific surface area and pore volume. The results indicate that MCM-41 has a high surface area (825 m<sup>2</sup> g<sup>-1</sup>) and a large pore volume (0.63 cm<sup>3</sup> g<sup>-1</sup>) that play an important role in improving the porosity of composite materials. It is observed that after incorporating MCM-41 to the nanocomposite titania powder, the specific surface area of the nanocomposite gradually increased. In comparison to B-100W, S-100W has greater porosity than B-100W. S-100W exhibits high specific surface area (479 m<sup>2</sup> g<sup>-1</sup>), high pore volume (0.40 cm<sup>3</sup> g<sup>-1</sup>) and low pore diameter (3.3 nm), determined as mesoporous materials. This result can be concluded that the incorporation of MCM-41 to TiO<sub>2</sub> cause the increase of surface area which might influence the adsorption mechanism during photocatalytic activity of TiO<sub>2</sub>/MCM-41.



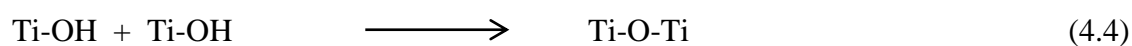
**Figure 4.9** Nitrogen adsorption-desorption isotherm of TiO<sub>2</sub>, B-100W, S-100W and MCM-41.

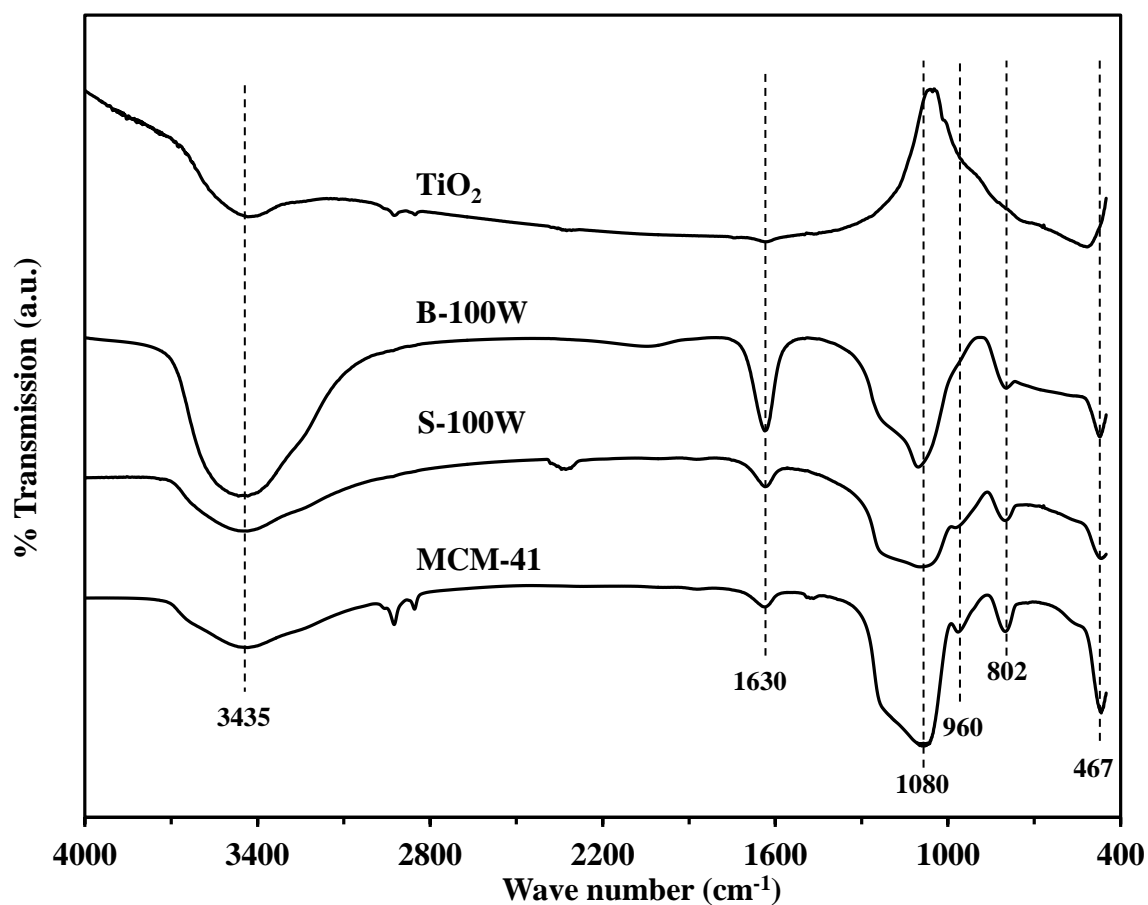
**Table 4.3** Porosity of TiO<sub>2</sub>, B, S and MCM-41 studied by BET analysis.

Samples	specific surface area (m <sup>2</sup> g <sup>-1</sup> )	Total pore volume (cm <sup>3</sup> g <sup>-1</sup> )	Pore size diameter (nm)
TiO <sub>2</sub>	7	0.06	34.0
B-100W	49	0.18	14.3
S-100W	479	0.40	3.3
MCM-41	825	0.63	2.7

The Fourier Transform Infrared (FTIR) analysis of the TiO<sub>2</sub>, B, S and MCM-41 samples is shown in Figure 4.10. The wide band position at 470 to 800 cm<sup>-1</sup> found in TiO<sub>2</sub>, corresponds to the stretching vibration of Ti-O bonding. The strong broad band at 1080

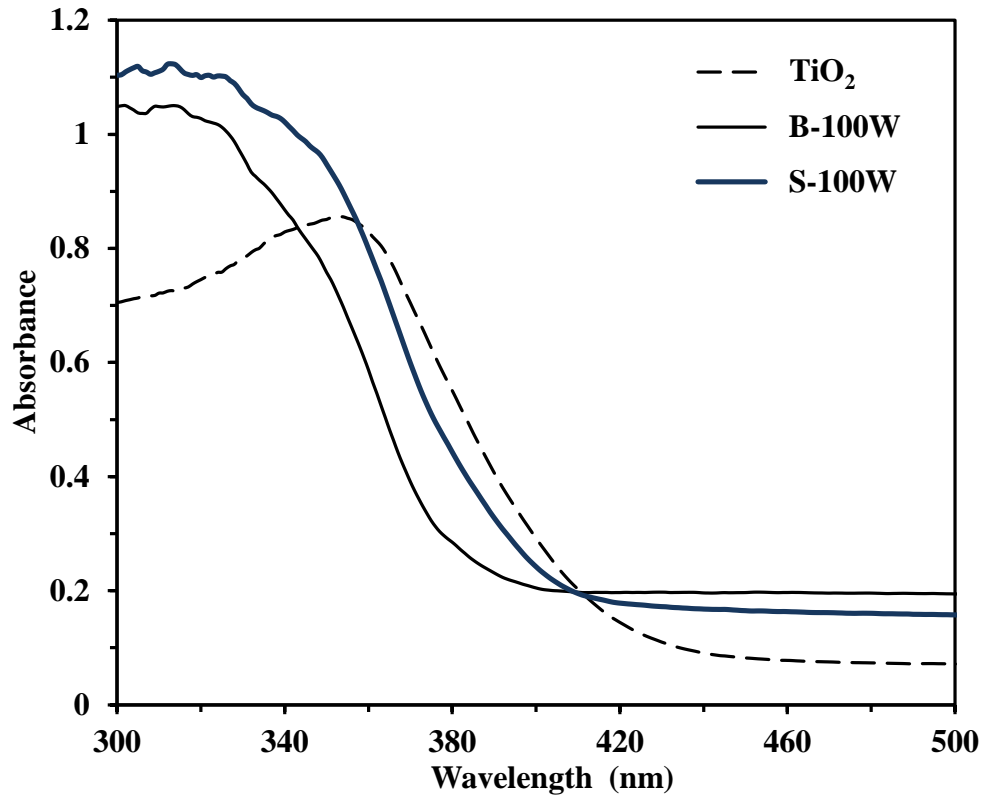
$\text{cm}^{-1}$  and  $802\text{ cm}^{-1}$ , assigned to Si-O-Si in asymmetric and symmetric stretching, respectively [70] and the band at  $467\text{ cm}^{-1}$  attributed to tetrahedral bending vibration of Si-O-Si bonds corresponds to the siloxane MCM-41 framework [71]. These spectra are found only in the MCM-41 and  $\text{TiO}_2/\text{MCM-41}$  samples. In addition, the small band at  $960\text{ cm}^{-1}$  indicating to the silanol groups (Si-OH) located mainly at the wall surface of MCM-41 was observed from MCM-41 and S-100W. This result confirmed that the incorporating  $\text{TiO}_2$  to MCM-41 by S method did not destroy the structure of MCM-41. On the contrary, the band spectra of silanol groups were not seen from B-100W. This result confirms that silanol group (Si-OH) in MCM-41 structure could not be formed via batch synthesis. The large broad band in the range of  $3600\text{-}3050\text{ cm}^{-1}$  is observed in all samples attributed to the hydroxyl (O-H) stretching vibration related to surface absorbed water. The O-H bond can be attributed from Si-OH and Ti-OH groups in the prepared solution. Moreover, it was reported that OH region, the vibration modes of the  $\text{Ti}^{4+}\text{-OH}$  and adsorbed  $\text{H}_2\text{O}$  on surface are found around  $3,435$  and  $1630\text{ cm}^{-1}$ , respectively [73]. However, the FTIR results indicated that the main chemical bonding of Si-O-Si and Ti-O-Ti appeared in the  $\text{TiO}_2/\text{MCM-41}$ . According to Figure 4.10, the formation of chemical bonding was proposed as the following equations:





**Figure 4.10** FTIR spectra of TiO<sub>2</sub>, B-100W, S-100W and MCM-41.

Optical properties of TiO<sub>2</sub> and TiO<sub>2</sub>/MCM-41 nanoparticles were measured by UV-visible spectroscopy using diffuse reflectance spectra. Figure 4.11 shows that the absorption spectra of TiO<sub>2</sub>/MCM-41 were shifted to lower wavelengths as compared to pure TiO<sub>2</sub>. Moreover, it was also seen that the absorption intensity of TiO<sub>2</sub>/MCM-41 composite increases in the UV region. This phenomenon is consistent with the results of Klankeaw *et al.* (2012), who synthesized TiO<sub>2</sub>/MCM-41 photocatalyst film. They reported a blue shift effect due to the incorporation of SiO<sub>2</sub> to the TiO<sub>2</sub> photocatalyst [33].



**Figure 4.11** UV-visible diffuse reflectance spectra of TiO<sub>2</sub>, B-100W and S-100W samples.

The band gap energy ( $E_g$ ) of the prepared photocatalysts can be determined from the onsets of absorption edges following the equation below:

$$E_g = \frac{hc}{e\lambda} \quad (4.7)$$

Where

$E_g$  is the band gap energy (eV)

$h$  is Planck's constant ( $6.626 \times 10^{-34}$  J·s)

$c$  is speed of light ( $3 \times 10^8$  m s<sup>-1</sup>)

$e$  is  $1.6 \times 10^{-19}$  J eV<sup>-1</sup> (conversion factor)

$\lambda$  is the cut off wavelength (m) determined from the intersection wavelength of the absorption spectra

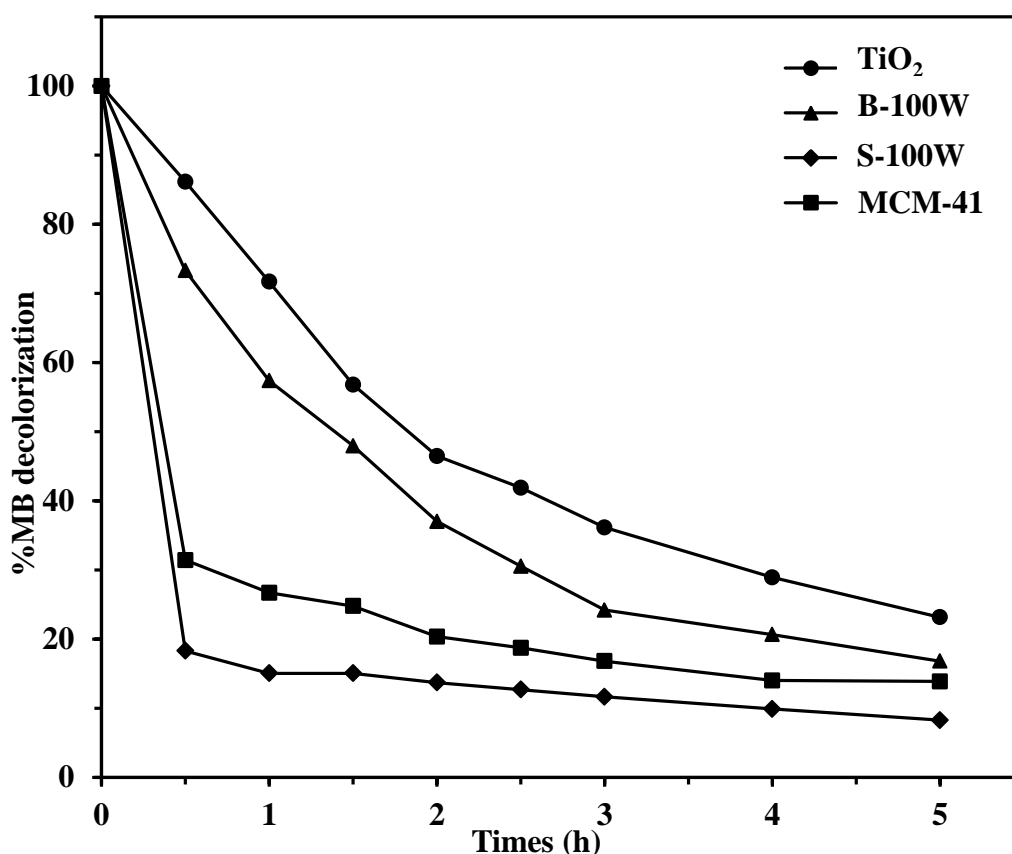
**Table 4.4** Band gap energy of photocatalysts.

Samples	$\lambda_{\text{cut-off}}$ (nm)	$E_g$ (eV)
TiO <sub>2</sub>	412	3.01
B-100W	381	3.26
S-100W	394	3.15

The band gap energy of the photocatalyst samples was calculated and is given in Table 4.3. The TiO<sub>2</sub> powder shows the absorption edge at 412 nm, and the band gap energy was 3.01 eV. TiO<sub>2</sub>/MCM-41 samples had larger band gap energy due to blue shift effect. The UV-vis adsorption edges of B-100W and S-100W show at 381 nm and 394 nm, correlated with the band gap energy as 3.26 eV and 3.15 eV, respectively. This result is in agreement with the UV-vis absorption spectra.

#### 4.4.2 Photocatalytic performance of TiO<sub>2</sub>/MCM-41

The photocatalytic decolorization of  $10^{-5}$  M MB dye with 100 mg of MCM-41, TiO<sub>2</sub>, B and S powder samples was tested under UV light irradiation. Figure 4.12 shows that the MB decolorization decreased dramatically when the irradiation time increased. The photodecolorization efficiencies of MB dye with 5 h was in order of S-100W (92%) > MCM-41 (86%) > B-100W (83%) > TiO<sub>2</sub> (77%). The result indicated that S-100W shows the highest efficiency in MB decolorization among all samples. This is because the surface area and high UV absorption as discussed previously. Therefore, the roles of MCM-41 introduced to TiO<sub>2</sub> which prepared by S method not only enhance the adsorbability of the photocatalyst, but also provide active hydroxyl species which can facilitate the photocatalytic reaction of TiO<sub>2</sub>.



**Figure 4.12** MB decolorization of MB dye by TiO<sub>2</sub>, B-100W, S-100W and MCM-41 under UV light irradiation

#### 4.5 Conclusions

In summary, this chapter studied the preparation of TiO<sub>2</sub>/MCM-41 powder by the batch (B) and sequence (S) methods, and by hydrothermal processes. The sample prepared by sequence method irradiated with microwave at 100W for 5 min exhibited the promising characteristics, comparable to the hydrothermal process. Results from XRD, BET, FTIR, UV-vis-DRS and morphological studied from TEM and SEM-EDX exhibits that porosity and UV absorption of TiO<sub>2</sub> can be enhanced by incorporating MCM-41 via S method. As a result, S-100W gave the highest efficiency (92%) of photocatalytic decolorization of MB dye testing under UV light irradiation among samples. However, the wavelength absorption of TiO<sub>2</sub>/MCM-41 sample was very low in visible light region. In order to improve the photocatalytic reactivity of TiO<sub>2</sub>/MCM-41 under visible light, next study will focus on doping Ag into TiO<sub>2</sub>/MCM-41. The sequence method and microwave assisted

sol-gel technique with microwave irradiation at 100 W will be used to prepare the Ag/TiO<sub>2</sub>/MCM-41 sample. The preparation procedure and the characterization results are explained in the next chapter.



## CHAPTER V

### PREPARATION OF Ag/TiO<sub>2</sub>/MCM-41 NANOCOMPOSITE POWDER AND FILM BY MICROWAVE ASSISTED SOL-GEL TECHNIQUE

#### 5.1 Introduction

According to the previous study, the TiO<sub>2</sub>/MCM-41 powder prepared by the sequence method is able to improve the adsorbability and photocatalytic reactivity of TiO<sub>2</sub> under UV irradiation. MCM-41 could not only enhance the specific surface area but it could also promote the active hydroxyl radicals ( $\cdot\text{OH}$ ) which behave as an oxidizing agent to destroy organic pollutants during photocatalytic reaction. However, the photocatalytic performance of the prepared TiO<sub>2</sub>/MCM-41 particle was still very low due to low visible light absorption of the material. Recently, doping silver into TiO<sub>2</sub> is widely used to enhance the photocatalytic reactivity of TiO<sub>2</sub> under visible light, because silver particles can reduce the band gap energy of TiO<sub>2</sub>, and prevent  $e^-h^+$  recombination. Yu *et al.* (2013) reported that Ag doped TiO<sub>2</sub> exhibited high photocatalytic reactivity in visible light [30]. This is a result of the surface plasmon resonance photolysis of Ag nanoparticles, in which the electrons migrate to the conduction band of TiO<sub>2</sub> and are further trapped by O<sub>2</sub>, producing oxidative species, which promote the oxidation of organic pollutants. Thus, this chapter focused on the improvement of photocatalytic reactivity of TiO<sub>2</sub>/MCM-41 under visible light irradiation. The influences of Ag and MCM-41 doping on TiO<sub>2</sub> in the forms of powder and film were investigated. The photocatalytic reactivity of the nanocomposite films was evaluated from the photocatalytic decolorization of methylene blue dye under UV and visible light. Eventually, the kinetic reaction model was determined and the reaction rate constants were then proposed.

#### 5.2 Research objectives

5.2.1 To prepare visible light responsive Ag/TiO<sub>2</sub>/MCM-41 nanocomposite powder and film by using a microwave-assisted sol-gel technique.

5.2.2 To investigate the effect of Ag and MCM-41 loading on the physical and chemical properties of Ag/TiO<sub>2</sub>/MCM-41 nanocomposite powder and film.

5.2.3 To study the photocatalytic reactivity of Ag/TiO<sub>2</sub>/MCM-41 nanocomposite film on decolorization of methylene blue dye under UV and visible light irradiation.

### 5.3 Experimental procedure

#### 5.3.1 Preparation of Ag/TiO<sub>2</sub>/MCM-41 nanocomposite films

The Ag/TiO<sub>2</sub>/MCM-41 sol-gel was prepared by microwave-assisted sol-gel processes using the sequence synthesis method. As-synthesized MCM-41 was prepared from rice husk silica according to Chiarakorn (2003). The extracted silica was dissolved in NaOH solution and mixed with CTAB to produce a gel with a molar ratio of SiO<sub>2</sub>: 1.1NaOH: 0.13CTAB: 12H<sub>2</sub>O. After an adjustment of the pH to 10, the gel was stirred under room temperature for 48 h. The MCM-41 slurry was filtered with a 0.45 μm membrane filters and washed with ethanol and deionized water. The obtained product was called as-synthesized MCM-41.

The Ag doped TiO<sub>2</sub> precursor solution was prepared by mixing titanium butoxide and AgNO<sub>3</sub> in ethanol solution with the molar composition of Ti(OC<sub>4</sub>H<sub>9</sub>)<sub>4</sub>: 18CH<sub>3</sub>CH<sub>2</sub>OH: 0.5C<sub>5</sub>H<sub>8</sub>O<sub>2</sub>: 2H<sub>2</sub>O: 0.2HNO<sub>3</sub>: xAgNO<sub>3</sub>, where (x = 0, 0.01, 0.1 and 0.2 mol Ag). The mixture was stirred homogeneously under room temperature. The as-synthesized MCM-41 was then loaded to Ag/TiO<sub>2</sub> precursor solution with different Si molar ratio as 0, 0.5, 1 and 2. The mixed gel was stirred under room temperature for 1 h. The microwave assisted sol-gel method was carried out by irradiating microwave at wattage of 100 W for 5 min (measured temperature as 75 °C). To obtain nanocomposite powder, the gel was dried overnight and calcined at 550 °C for 5 h with the heating rate of 9 °C min<sup>-1</sup> in a muffle furnace. The nanocomposite films were formed by dipping the gel on glass slides using an automatic coating machine with a drawing speed of 10 cm min<sup>-1</sup> for 5 cycles.

#### 5.3.2 Characterizations

The crystallinity of nanocomposites was examined by X-ray diffractometer (XRD: Rigaku TTRAX III, Japan) with Cu K<sub>α</sub> radiation at a voltage of 50 kV and 300 mA (λ = 0.1541 nm) with scanning speed of 3° min<sup>-1</sup>. The morphology and the thickness of the films were studied by a field emission scanning electron microscope (FESEM: S-4800, Hitachi). Atomic force microscope (AFM: SPI4000, SEIKO) was used for detecting nanoscale roughness of the films. The root mean square (RMS) roughness were estimated by spectral analysis on 1 μm<sup>2</sup> area and scanning speed of 0.50 Hz. Ultraviolet-visible absorbance

spectra were obtained from UV-visible diffuse reflectance spectrophotometer (UV 3100, Shimadzu) scanning in the range of 300 to 700 nm. X-ray photo-electron spectroscopy (XPS: AXIS Ultra DLD, Kratos Analytical Ltd.) was applied to analyze elemental composition and electronic state of the elements with the scanning spectrum of O 1s, Ti 2p, Si 2p and Ag 3d. The binding energy scale was calibrated with respect to the C 1s peak at 285.0 eV. The contact angle is commonly used to describe the relative hydrophobicity/hydrophilicity of a material surface, and was measured by dropping 1 mL of water onto the film contact surface. Optical images of water droplets were recorded with a camera, at various time intervals. The contact angle ( $\theta$ ) could be determined from the diameter ( $d$ ) and the height ( $h$ ) of the droplets as following equation (3.1).

### 5.3.3 Photocatalytic measurement

The decolorization of methylene blue (MB) dye solution was applied to determine the photocatalytic reactivity of the composite films. The method was modified from Japanese industrial standard (JIS R 1703-2). For each test, the film was placed into 25 mL of  $10^{-5}$  M MB dye solution under dark and wait until the adsorption of MB dye on the film reached the equilibrium. After that the film was transferred into new MB solution with the same concentration of  $10^{-5}$  M. The photocatalytic activity of the film under visible light and UV irradiation was studied by turning on a fluorescent lamp 15 W, Philips with the light intensity of 1,100 lux and an UV 15 W germicidal lamp ( $\lambda \sim 254$  nm), Philips with the light intensity of  $2.5 \text{ W m}^{-2}$ , respectively. The distance of light sources was set above the solution as 15 cm. Each 3 mL of MB solution was taken every hour to evaluate the absorbance by using UV-visible spectroscopy (Genesis10 UV) at the maximum wavelength of 663 nm and then returned to the container. The kinetic reaction model was studied by plotting the relationship between concentration of MB and irradiation time.

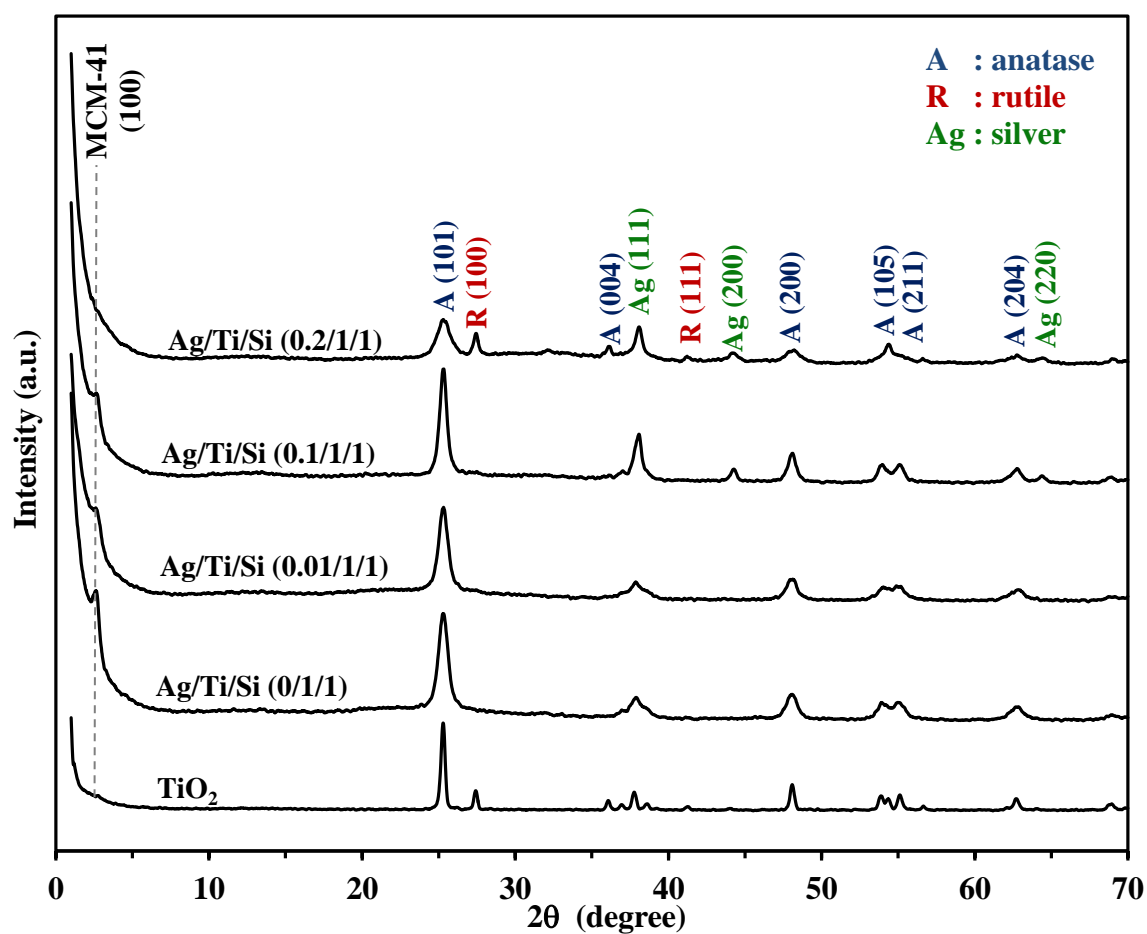
## 5.4 Results and discussion

### 5.4.1 Crystallinity

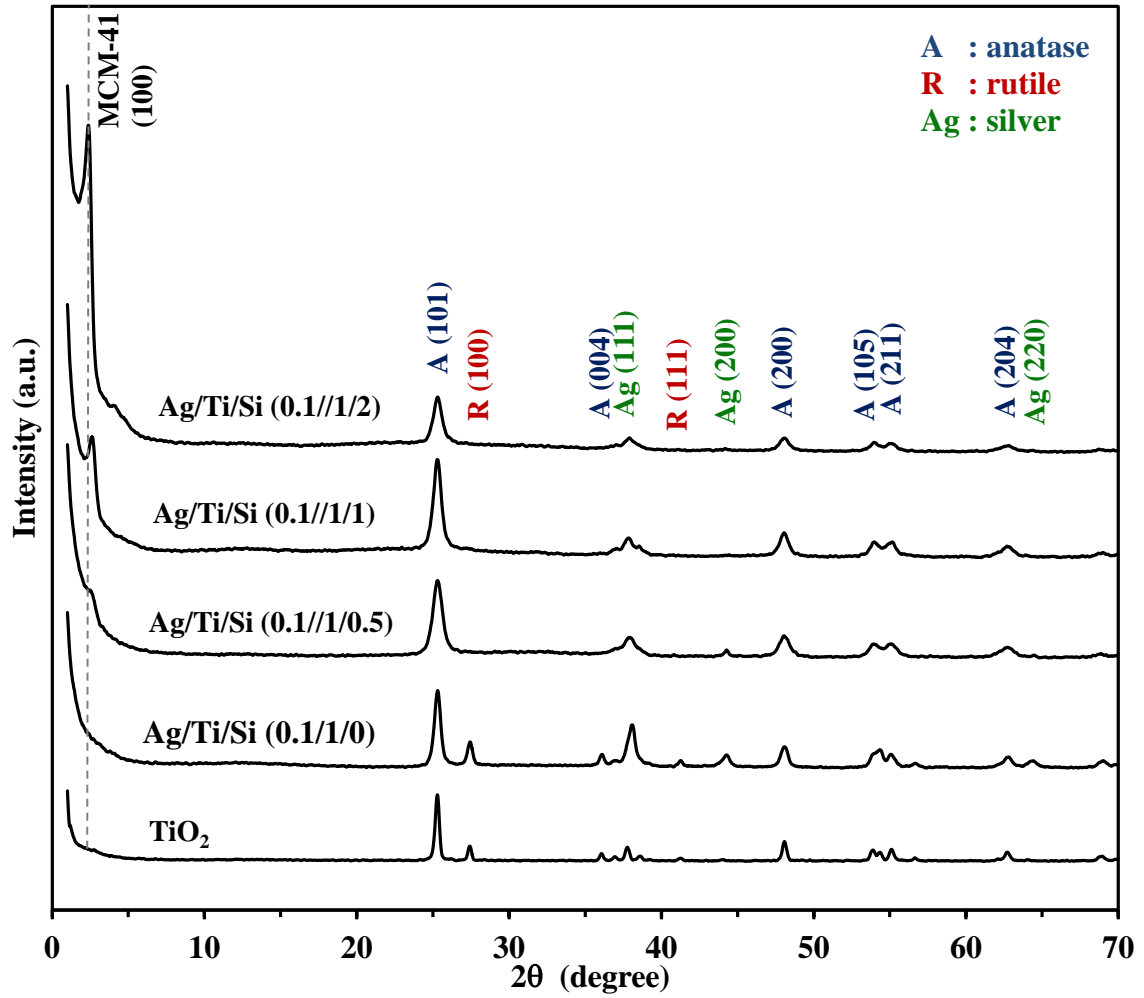
X-ray diffraction (XRD) was used to evaluate the crystalline structure of powder and film samples. Figure 5.1 shows the wide angle XRD patterns of Ag/Ti/MCM-41 powders with various Ag molar ratios of Ag/Ti/Si as 0/1/1, 0.01/1/1, 0.1/1/1 and 0.2/1/1. It was found that the diffraction peaks of nanocomposite powders exhibit the characteristics of MCM-41, anatase and silver nanoparticle. The diffraction peak of the MCM-41 hexagonal structure is found at  $2\theta$  of  $2.3^\circ$ , corresponding to  $hkl$  (100), as reported elsewhere. The characteristic peaks of anatase crystalline are found at  $2\theta$  of  $25.3^\circ$  (101),  $37.9^\circ$  (004),  $48.1^\circ$  (200),  $53.9^\circ$  (105),  $55.0^\circ$  (211) and  $62.7^\circ$  (204), according to JCPDS No. 21-1272. The peak intensity of XRD pattern of pure  $\text{TiO}_2$  consisted with the both phases of anatase (101) and rutile (110), appeared at  $2\theta$  of  $25.3^\circ$  and  $27.3^\circ$ , respectively. On the contrary, the XRD pattern of nanocomposite samples did not show rutile phase except Ag/Ti/Si (0.2/1/1). This result implied that the transformation of anatase to rutile phases could be inhibited by adding  $\text{SiO}_2$  structure, while the excess amount of silver might disturb the formation of MCM-41 arrangement [73]. Moreover, the crystal peaks of silver nanoparticles ( $\text{Ag}^0$ ) were obviously seen from Ag/Ti/Si (0.1/1/1) and Ag/Ti/Si (0.2/1/1) appeared at  $2\theta$  of  $38.1^\circ$ ,  $44.2^\circ$  and  $64.4^\circ$ , (JCPDS No. 89-3722), corresponding to  $hkl$  (111), (200) and (220), respectively. While, the characteristic peak of  $\text{Ag}^0$  was not found from Ag/Ti/Si (0.01/1/1) due to it has low Ag loading. In addition, the increase of  $\text{Ag}^0$  amount has an adverse effect on the crystallinity of MCM-41 and anatase structure. Accordingly, the optimal ratio of Ag/Ti/Si was suggested as 0.1/1/1.

In order to study the appropriate amount of MCM-41 on Ag/TiO<sub>2</sub>/MCM-41 nanocomposite samples, the molar ratio of Ag was fixed at 0.1 and the molar ratio of Si was then varied from 0, 0.5, 1 and 2. Figure 5.2 shows the XRD patterns of  $\text{TiO}_2$ , Ag/Ti/Si (0.1/1/0), Ag/Ti/Si (0.1/1/0.5), Ag/Ti/Si (0.1/1/1) and Ag/Ti/Si (0.1/1/2) nanocomposite powders. The diffractograms of Ag/Ti/Si (0.1/1/0) film exhibit distinctive diffraction peaks of anatase at  $2\theta$  equal to  $25.3^\circ$ , corresponding to  $hkl$  (101), and rutile at  $2\theta$  equal to  $27.4^\circ$  (JCPDS No. 21-1276), corresponding to  $hkl$  (110), respectively. The crystalline Ag nanoparticles appear at  $2\theta$  equal to  $38.1^\circ$  and  $44.2^\circ$  (JCPDS No. 89-3722), corresponding to  $hkl$  (111) and (200), respectively. After incorporating MCM-41 into the Ag/TiO<sub>2</sub> nanoparticles, the main characteristic diffraction peak of MCM-41 is observed at  $2\theta$  equal

to  $2.3^\circ$ , corresponding to  $hkl$  (100). However, the diffraction peaks of rutile crystals disappear, and the intensity of anatase peaks decreases. This can be explained in that the  $\text{Si}^{4+}$  ions can penetrate and replace  $\text{Ti}^{4+}$  in the framework of rutile crystals, resulting in the deformation of rutile as well as the anatase crystalline structure [73]. Additionally, incorporating MCM-41 into the Ag/Ti nanoparticles leads to the decrease of the peak intensity of the Ag nanoparticles. Two possible reasons are that an excess of  $\text{Si}^{4+}$  ions may disturb the formation of Ag nanoparticles, or some Ag ions disturb MCM-41.



**Figure 5.1** XRD patterns of  $\text{TiO}_2$  and  $\text{Ag/TiO}_2/\text{MCM-41}$  powder samples with various Ag content.



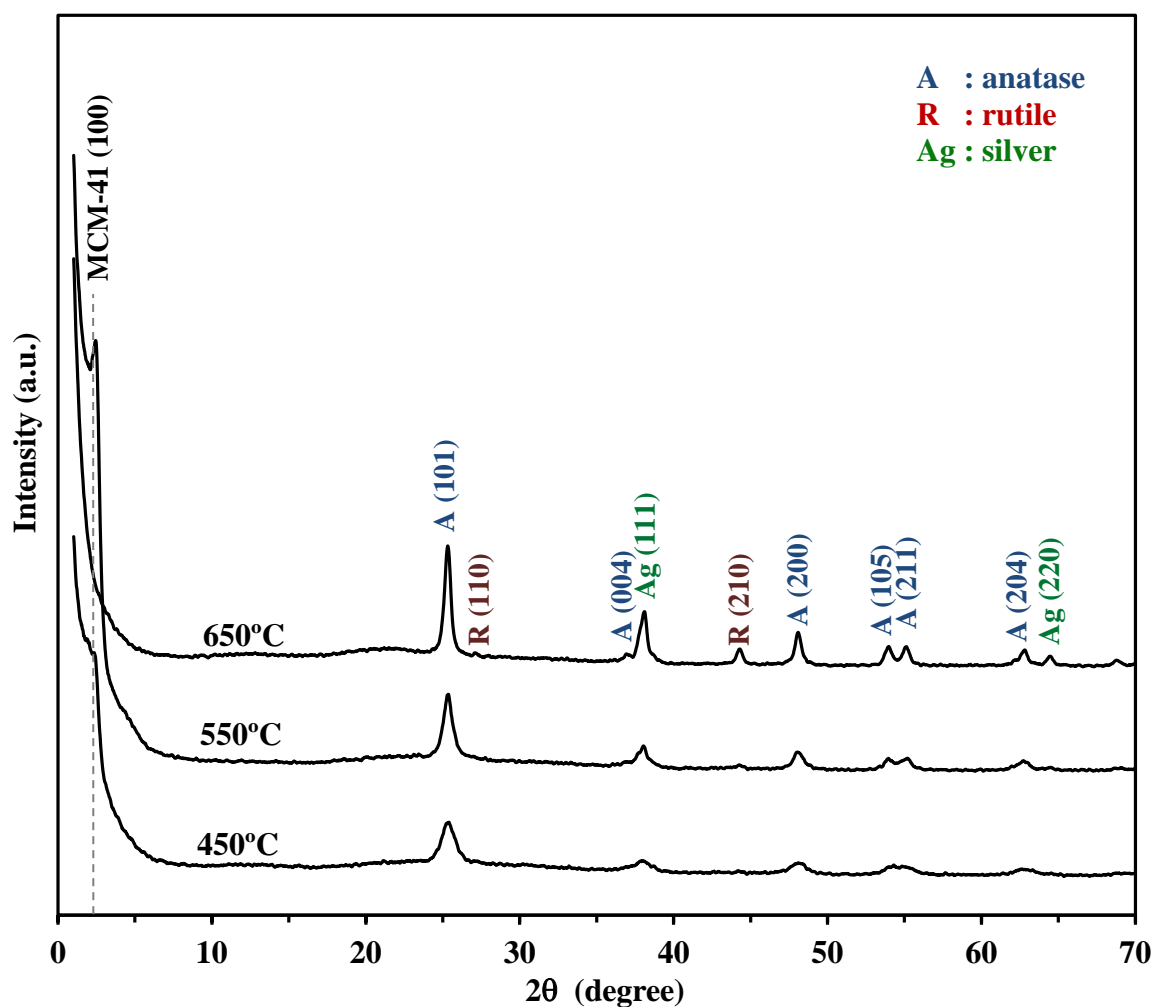
**Figure 5.2** XRD patterns of  $\text{TiO}_2$  and nanocomposite  $\text{Ag}/\text{TiO}_2/\text{MCM-41}$  powder samples with various Si content.

The crystallite size of nanocomposite powders was determined from the width of the peak anatase ( $101$ ) at  $2\theta$  equal to  $25.3^\circ$  using the Scherrer Equation:

$$L = \frac{k\lambda}{\beta \cos \theta} \quad (5.2)$$

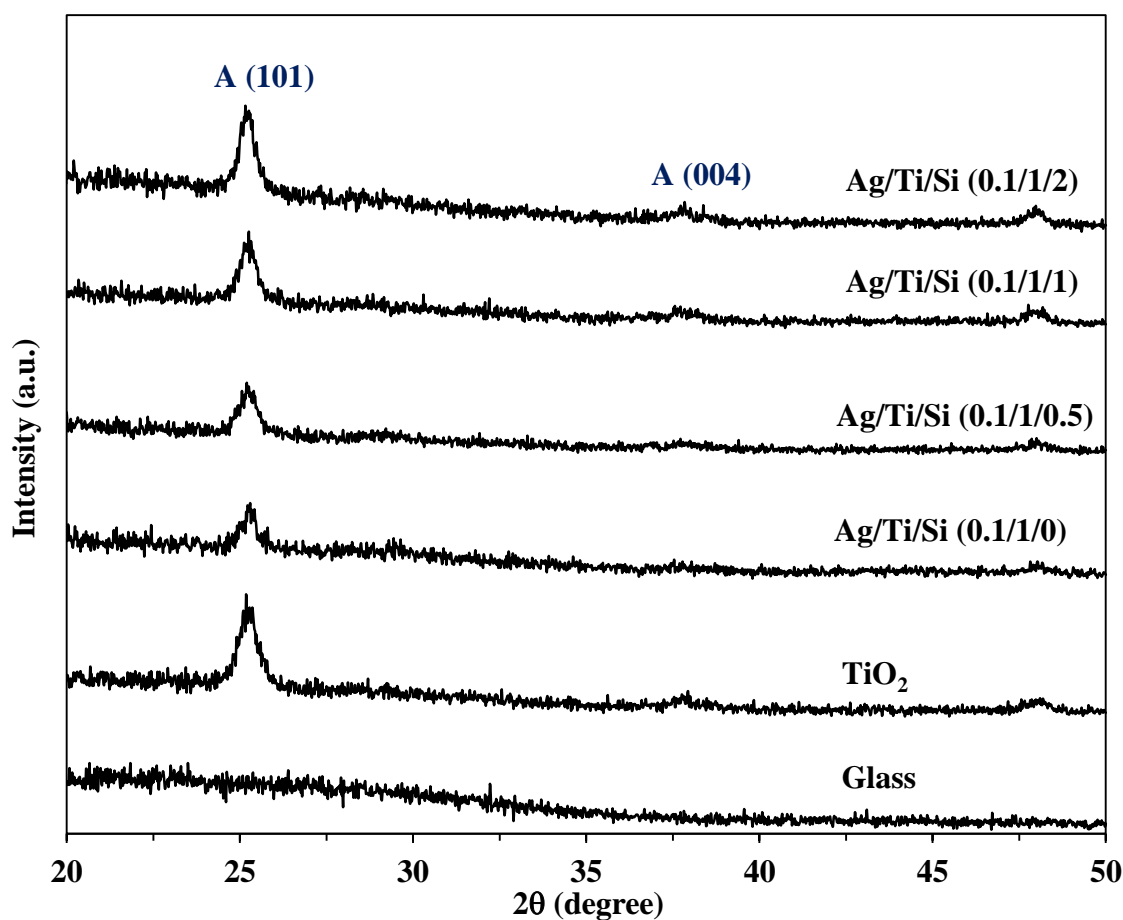
Where  $L$  is the crystallite size,  $k$  is a shape factor, which is typically 0.89,  $\lambda$  is the  $\text{Cu K}\alpha$  radiation wavelength,  $\beta$  is the full width at half-maximum of the peak at ( $101$ ), and  $\theta$  is the diffraction angle.

The crystallite sizes of  $\text{TiO}_2$ ,  $\text{Ag/Ti/Si}$  (0/1/1),  $\text{Ag/Ti/Si}$  (0.01/1/1),  $\text{Ag/Ti/Si}$  (0.1/1/1) and  $\text{Ag/Ti/Si}$  (0.2/1/1) nanocomposite powders were 23.9, 11.8, 13.6, 13.4 and 9.1 nm, respectively. While, the crystallite sizes of  $\text{Ag/Ti/Si}$  (0.1/1/0),  $\text{Ag/Ti/Si}$  (0.1/1/0.5),  $\text{Ag/Ti/Si}$  (0.1/1/1) and  $\text{Ag/Ti/Si}$  (0.1/1/2) nanocomposite powders were 16.8, 13.8, 13.4 and 12.7 nm, respectively. The results show that the crystallite sizes of anatase (101) on powder samples with various molar ratios of Ag and Si decrease with Ag and Si contents increase. It can be noticed that the crystallization of anatase crystals was inhibited when incorporating Ag and MCM-41 into the composite structure.



**Figure 5.3** Effect of calcination temperatures on the crystallinity of  $\text{Ag/Ti/Si}$  (0.1/1/2) powder.

Furthermore, the effect of calcination temperature was also studied on Ag/Ti/Si (0.1/1/2) nanocomposite powder calcined at 450 °C, 550 °C and 650 °C (in Figure 5.3). The results exhibited characteristics of MCM-41. Anatase  $\text{TiO}_2$  and  $\text{Ag}^0$  were obviously seen only from the sample calcined at 550 °C. The XRD pattern exhibits the intense peaks of MCM-41 crystal at  $2\theta$  of  $2.3^\circ$  ( $100$ ), anatase phase at  $2\theta$  of  $25.3^\circ$  ( $101$ ) and  $\text{Ag}^0$  peak at  $38.1^\circ$  ( $111$ ). It can be observed that the calcination at 650 °C could increase the crystalline of anatase and rutile but the structure of MCM-41 crystal was destroyed. This is because the formation of rutile phase at high temperature can disturb the hexagonal arrangement of MCM-41 arrangement. The result agrees with the other researchers. It was reported that a phase transition changed from anatase to rutile by calcination at temperature above 600 °C [73, 74]. Therefore, the calcination temperature for the preparation of nanocomposite samples in this study was chosen at 550 °C.



**Figure 5.4** XRD patterns of photocatalyst films.



The XRD diffractograms of  $\text{TiO}_2$  and  $\text{Ag/TiO}_2/\text{MCM-41}$  photocatalyst films are illustrated in Figure 5.4. All photocatalyst films exhibit diffraction peaks at  $2\theta$  equal to  $25.3^\circ$ ,  $37.8^\circ$  and  $48.1^\circ$ , assigned to anatase ( $101$ ), ( $004$ ) and ( $200$ ), respectively. However, no diffraction pattern of MCM-41 was found, due to the limitations of the XRD instrument for film analysis, as it is unable to scan at an angle below  $10^\circ$ . In addition, the diffraction peak of Ag could not be observed from the film samples due to low thickness of the films. The average nanocrystallite sizes of anatase ( $101$ ) on films are approximately 11 nm to 13 nm. Similar to the XRD patterns of nanocomposite powder, the anatase reflection slightly decreased after doping Ag and MCM-41 into the nanocomposite films.

#### 5.4.2 Porosity

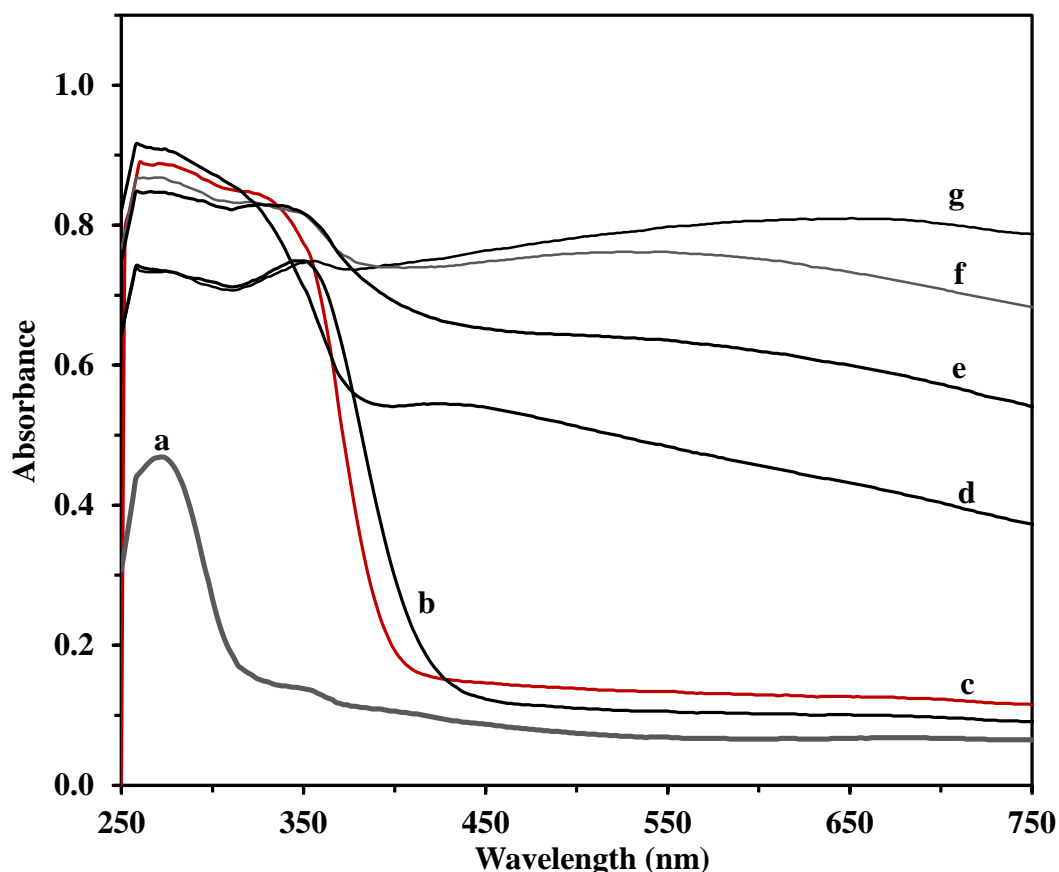
The porosity was studied by the nitrogen adsorption analyzer according to the Brunauer Emmett Teller (BET) technique, as seen in Table 1. The effect of MCM-41 on  $\text{TiO}_2$  was obviously seen in  $\text{Ag/Ti/Si}$  (0/1/1). After incorporating MCM-41 into  $\text{TiO}_2$ , the specific surface area and pore volume were increased. In addition, the pore diameter was decreased to 3 nm, defined as mesopore. However, when Ag was introduced to  $\text{TiO}_2/\text{MCM-41}$ , the surface area and pore volume of the composites were dramatically decreased. The specific surface area of the nanocomposite increases dramatically, from  $3 \text{ m}^2 \text{ g}^{-1}$  for  $\text{Ag/Ti/Si}$  (0.1/1/0) to  $267 \text{ m}^2 \text{ g}^{-1}$  for  $\text{Ag/Ti/Si}$  (0.1/1/2), respectively. In particular, it was found that  $\text{Ag/Ti/Si}$  (0.1/1/2) was the most promising molar ratio due to its high porosity, containing mesoporous structure of MCM-41 and anatase  $\text{TiO}_2$ . The results from XRD and BET analysis in this study were corresponded to the previous research. The incorporating of  $\text{SiO}_2$  (less than 30 mol%) into  $\text{TiO}_2$  has a suppressive effect on the transformation of anatase to rutile and on the crystal growth of anatase however, its surface area could be improved significantly [65]. Thus, it can be concluded that incorporating MCM-41 into  $\text{Ag/TiO}_2$  plays an important role in improving the porosity of  $\text{Ag/TiO}_2/\text{MCM-41}$  composite.

**Table 5.1** BET analysis of porosity of MCM-41, TiO<sub>2</sub> and Ag/TiO<sub>2</sub>/MCM-41 powders with various Ag and Si molar ratio.

Samples	specific surface area (m <sup>2</sup> g <sup>-1</sup> )	Total pore volume (cm <sup>3</sup> g <sup>-1</sup> )	Pore size diameter (nm)
TiO <sub>2</sub>	7	0.06	34
MCM-41	825	0.63	3
Ag/Ti/Si (0.1/1/0)	3	0.03	49
Ag/Ti/Si (0/1/1)	479	0.40	3
Ag/Ti/Si (0.01/1/1)	182	0.18	4
Ag/Ti/Si (0.1/1/0.5)	45	0.19	17
Ag/Ti/Si (0.1/1/1)	68	0.12	7
Ag/Ti/Si (0.1/1/2)	267	0.31	5

#### 5.4.3 UV/Vis/DR

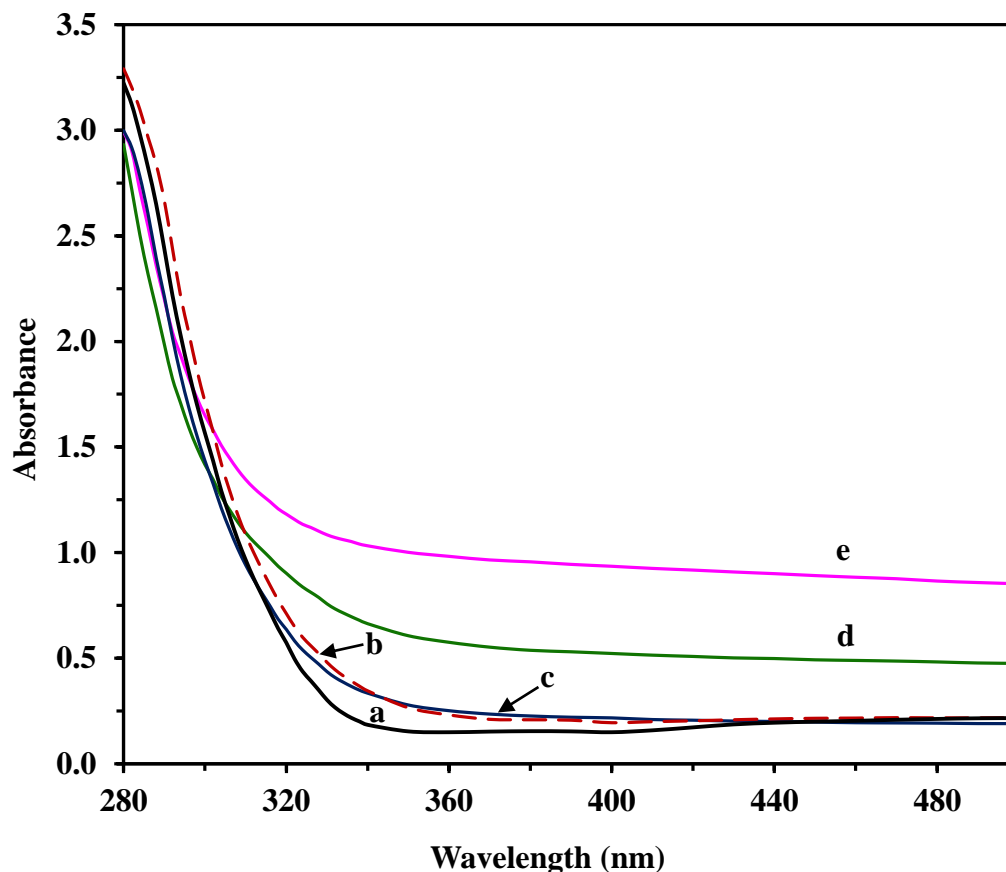
The UV-visible absorption spectra of TiO<sub>2</sub>, Ag/Ti/Si (0/1/1), Ag/Ti/Si (0.1/1/0), Ag/Ti/Si (0.1/1/0.5), Ag/Ti/Si (0.1/1/1) and Ag/Ti/Si (0.1/1/2) powder are presented in Figure 5.5. The absorption band at wavelengths higher than 420 nm of pure TiO<sub>2</sub> is lower than that of all nanocomposite samples. After doping Ag into TiO<sub>2</sub>, it was found that the wavelength absorption intensity in the range of visible light was significantly increased, as compared to pure TiO<sub>2</sub>. This phenomenon is theoretically called the “Red shift effect”. Similar to Yu *et al.* (2012) and Zhou *et al.* (2011), they repeated that Ag nanoparticles can absorb visible light, due to their surface plasmon resonance [17, 30]. However, when MCM-41 was introduced to Ag/TiO<sub>2</sub>, the intensity of visible light absorption was decreased but the intensity of UV absorption was increased, compared to Ag/TiO<sub>2</sub>. This is because the wavelength absorption of MCM-41 in both UV and visible light region was very low (lower than 400 nm). Similarly, this with Klankaw *et al.* (2012) has reported that a blue shift effect can occur when doping SiO<sub>2</sub> into TiO<sub>2</sub> photocatalyst [33]. Thus, the enhancement of visible light absorption of Ag/TiO<sub>2</sub>/MCM-41 is mainly caused by Ag nanoparticles. Red shift effect has an advantage on decreasing band gap energy of TiO<sub>2</sub> which promote electron transfer from valence band to conduction band under visible light.



**Figure 5.5** Diffuse reflectance UV-visible absorption spectra of (a) MCM-41, (b)  $\text{TiO}_2$ , (c)  $\text{Ag/Ti/Si}$  (0.1/1/1), (d)  $\text{Ag/Ti/Si}$  (0.1/1/2), (e)  $\text{Ag/Ti/Si}$  (0.1/1/1), (f)  $\text{Ag/Ti/Si}$  (0.1/1/0.5), and (g)  $\text{Ag/Ti/Si}$  (0.1/1/0) powder.

The wavelength absorption spectra of photocatalyst films are exhibited in Figure 5.6. The absorption spectra of  $\text{TiO}_2$  film in the visible light region can increase significantly by Ag doping as seen in the absorption band of  $\text{Ag/Ti/Si}$  (0.1/1/0). However, incorporating MCM-41 to  $\text{Ag/TiO}_2$ , observed from  $\text{Ag/Ti/Si}$  (0.1/1/0.5),  $\text{Ag/Ti/Si}$  (0.1/1/1) and  $\text{Ag/Ti/Si}$  (0.1/1/2) film, could exhibit the absorption edge shifted to UV region similar with the powder results. In addition, the intensity of wavelength absorption in visible light region was increased substantially when the incorporating MCM-41 into  $\text{Ag/TiO}_2$  film. This is because the large particle of MCM-41 obscured the transmission of light though the nanocomposite film. Hence, the wavelength absorption in the visible region of  $\text{Ag/Ti/Si}$  (0.1/1/2) film was higher than that of  $\text{TiO}_2$  and  $\text{Ag/Ti/Si}$  (0.1/1/0) films which performed more transparent. According to the absorption spectra results of the powder and the film samples, it can be seen that the coordination of Ag,  $\text{TiO}_2$  and MCM-41 leads to the

synergistic effect of promoting the absorption of both UV and visible light, which is an advantage for photocatalytic reaction.



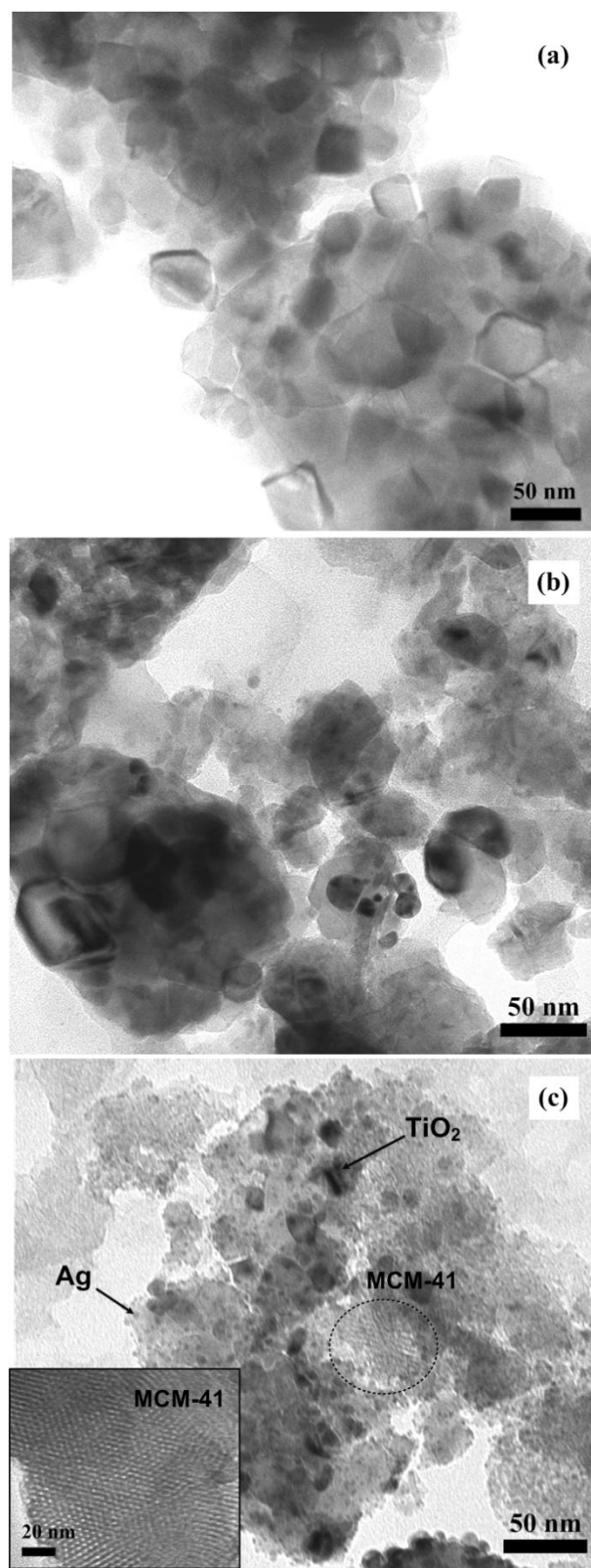
**Figure 5.6** Diffuse reflectance UV-visible absorption spectra of (a) TiO<sub>2</sub>, (b) Ag/Ti/Si (0.1/1/0), (c) Ag/Ti/Si (0.1/1/0.5), (d) Ag/Ti/Si (0.1/1/1) and (e) Ag/Ti/Si (0.1/1/2) films.

#### 5.4.4 Morphology and surface structure

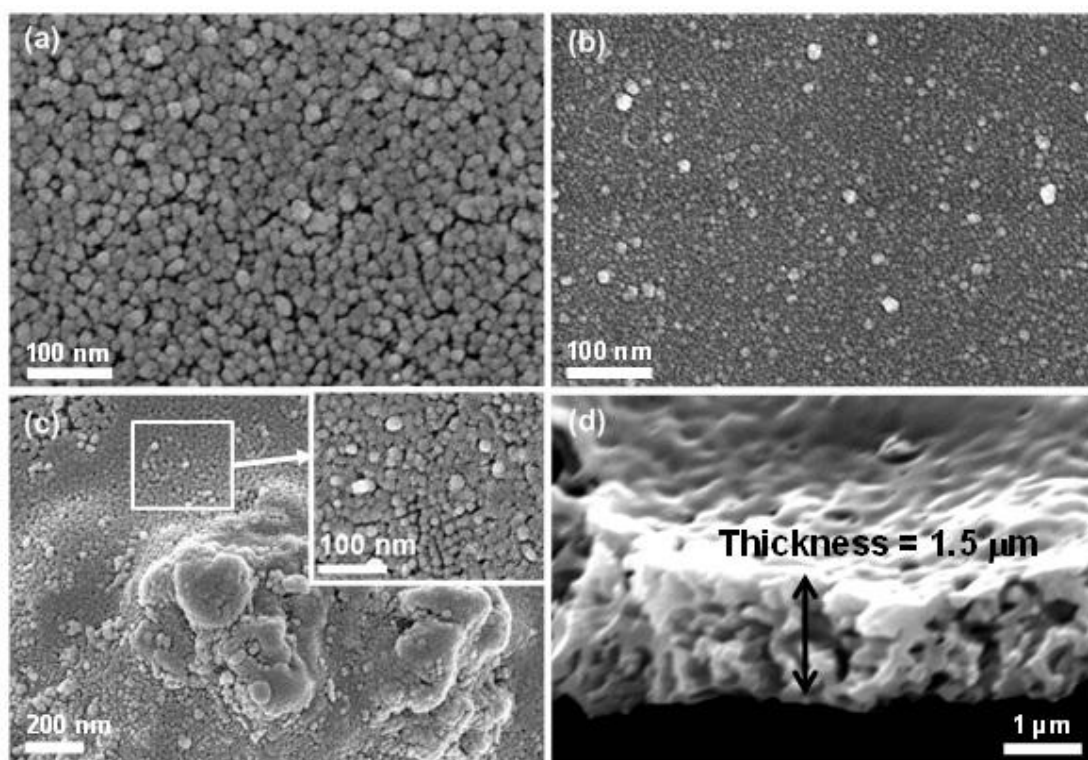
The TEM and FESEM images of TiO<sub>2</sub>, Ag/Ti/Si (0.1/1/0) and Ag/Ti/Si (0.1/1/2) were determined in the form of powder and film, respectively. Figure 5.7(a) shows the TEM image of the anatase phase in octahedral crystalline form with the average particle size of 30 to 50 nm. TEM image of Ag/Ti/Si (0.1/1/0) presents the TiO<sub>2</sub> crystals aggregate into clusters as seen from Figure 5.7(b). From the micrograph, the small Ag nanoparticles were found with the crystal sizes range of 2 to 5 nm. The nanocomposite phase of Ag/Ti/Si (0.1/1/2) according to Figure 5.7(c) shows the crystal phase of TiO<sub>2</sub> impregnated heterogeneously with pore channel of MCM-41. The average size of anatase TiO<sub>2</sub> distributed in MCM-41 was smaller than pure TiO<sub>2</sub> particle. Wang *et al.* (2012) revealed

that the particle size of  $\text{TiO}_2$  may be blocked by the MCM-41 structure [34]. Moreover, small particles of silver distributed in the  $\text{Ag/TiO}_2/\text{MCM-41}$  could be observed. However, the crystalline structure of  $\text{TiO}_2$  and the formation of MCM-41 were distorted with the silver loading, resulting in the decrease of surface area and pore volume of MCM-41.

High resolution surface images of  $\text{TiO}_2$ ,  $\text{Ag/Ti/Si}$  (0.1/1/0) and  $\text{Ag/Ti/Si}$  (0.1/1/2) nanocomposite films were observed by FESEM with the magnification of  $\times 100,000$ . Figure 5.8(a) displays the uniformly agglomerated nanotitania with a round shape. The particle size is approximately ranged from 10 to 15 nm. Figure 5.8(b) shows nanoparticle distributions on the surface of the  $\text{Ag/Ti/Si}$  (0.1/1/0) film. The average sizes of nanoparticles are 12 nm (large particles) to 3 nm (small particles). This result is in agreement with Sung-Suh *et al.* (2004) that the average particle size of Ag deposited on  $\text{TiO}_2$  was about 2 to 4 nm [51]. The heterogeneous nanoparticles of  $\text{Ag/Ti/Si}$  (0.1/1/2) composite film are presented in Figure 5.8(c). The particle dispersion is very poor due to the agglomeration of large MCM-41 particles. The FESEM images indicate that the growth of anatase titania is suppressed by incorporating Ag and MCM-41 into titania crystal structure. The cross section of  $\text{Ag/Ti/Si}$  (0.1/1/2) composite film with the magnification of 10,000 is illustrated in Figure 5.8(d). The average thickness is about 1.5  $\mu\text{m}$  for 5 coated film layers or 0.3  $\mu\text{m}$  for only one dip coated film layer. The surface roughness and porous surface caused by MCM-41 can be obviously seen from this image.



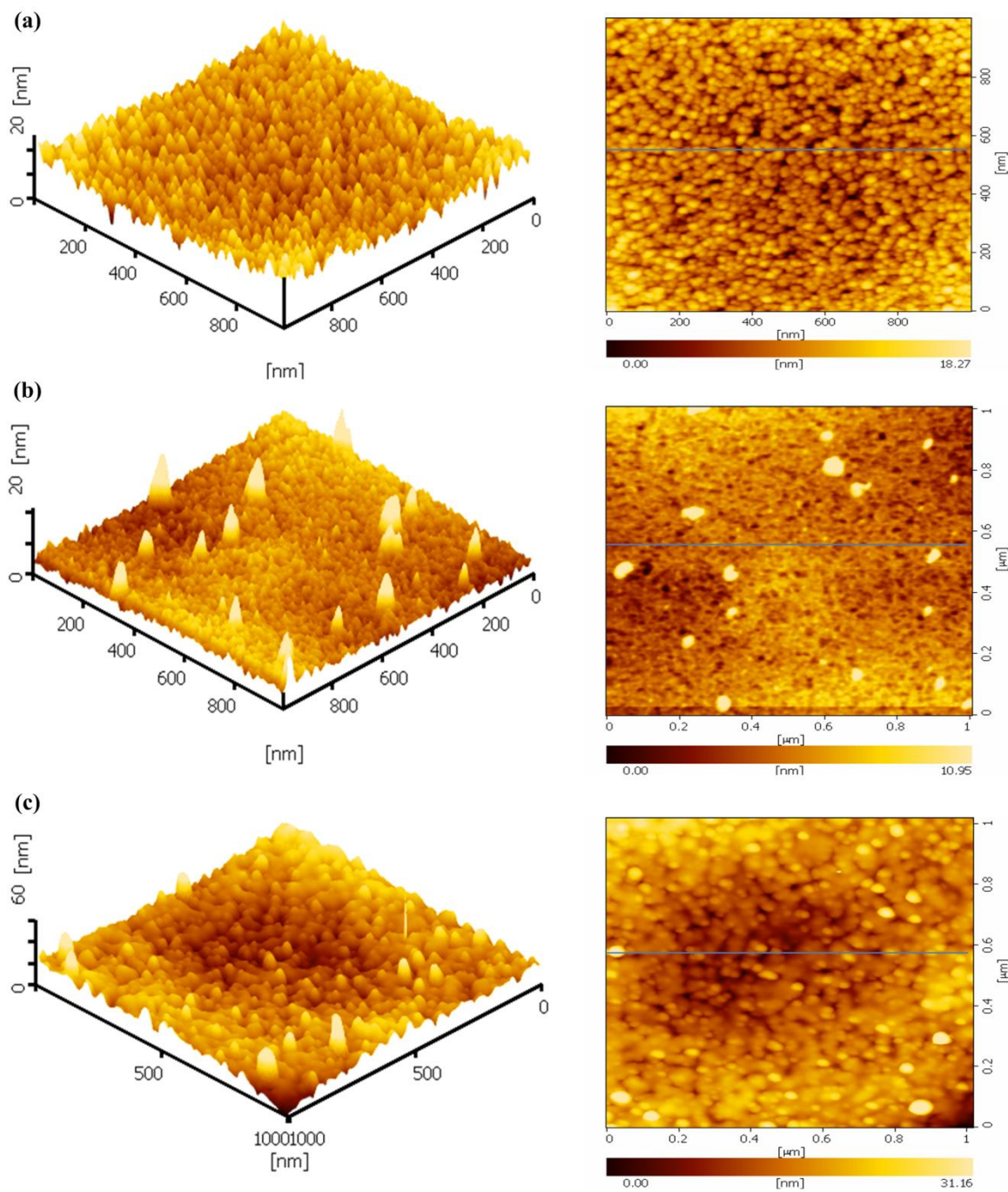
**Figure 5.7** TEM images of (a)  $\text{TiO}_2$ , (b)  $\text{Ag/Ti/Si}$  (0.1/1/0) and (c)  $\text{Ag/Ti/Si}$  (0.1/1/2) nanoparticles ( $40,000\times$  magnification).



**Figure 5.8** FESEM images of (a)  $\text{TiO}_2$ , (b)  $\text{Ag/Ti/Si}$  (0.1/1/0), (c)  $\text{Ag/Ti/Si}$  (0.1/1/2) films and (d) thickness of  $\text{Ag/Ti/Si}$  (0.1/1/2) films.

To study the surface roughness and surface composition of the composite films, AFM three-dimensional images of all nanocomposite films are illustrated in Figure 5.9. These images present significant differences between the surfaces of  $\text{TiO}_2$ ,  $\text{Ag/Ti/Si}$  (0.1/1/0) and  $\text{Ag/Ti/Si}$  (0.1/1/2) films. Similar to the FESEM results, the crystal phase of anatase titania film is orderly uniform and smooth. Figure 5.9(b) shows the distribution of silver nanoparticle deposited on  $\text{TiO}_2$  film. The distinctive bright spots are determined as nanoparticles of silver. It can be explained that during heat treatment, clusters of silver inserted in the matrix of  $\text{TiO}_2$  can migrate to the outer surface and coalesce, promoting the growth of silver crystals [18]. Figure 5.9(c) illustrates the heterogeneous particle sizes of  $\text{Ag/Ti/Si}$  (0.1/1/2) nanocomposite film. This result confirms that the loading of Ag and MCM-41 to  $\text{TiO}_2$  affects the crystallization of titania crystals, resulting in a disorderly arrangement of the nanoparticles on the composite film.





**Figure 5.9** AFM images of (a)  $\text{TiO}_2$ , (b)  $\text{Ag/Ti/Si}$  (0.1/1/0) and (c)  $\text{Ag/Ti/Si}$  (0.1/1/2) films.

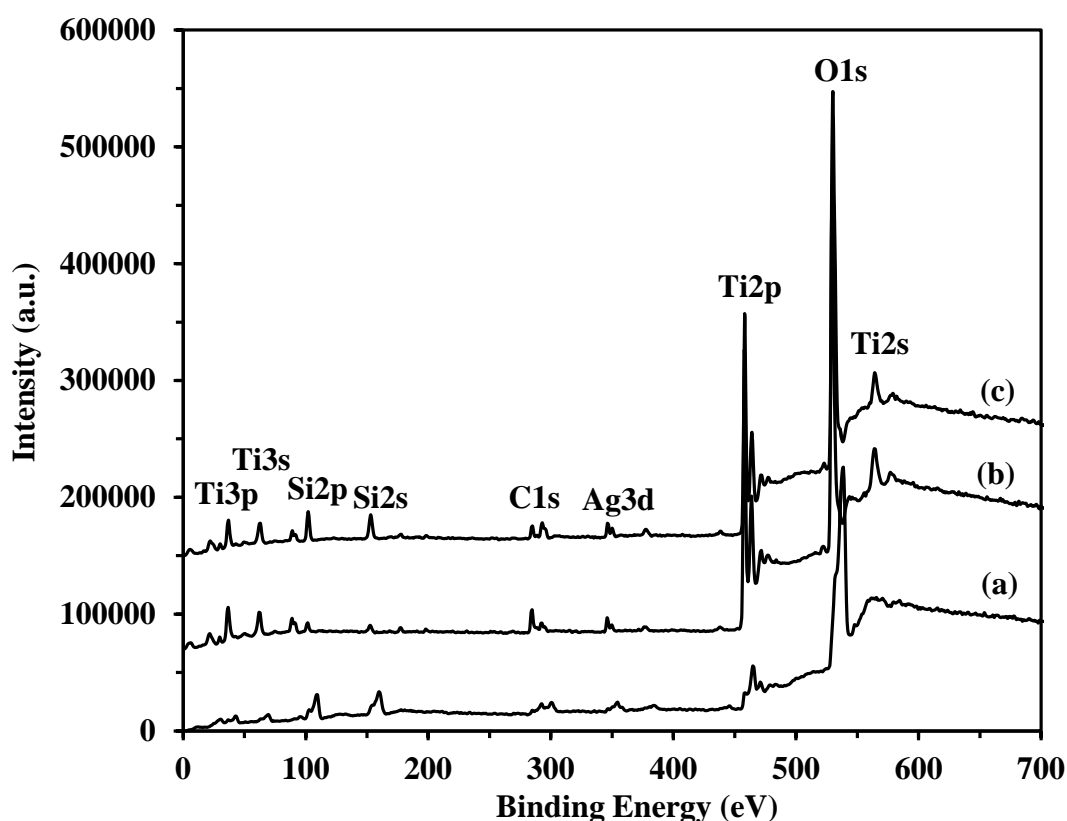
The roughness of the nanocomposite films was evaluated from Root Mean Square (RMS) roughness. The average RMS roughness was in the order of 4.75 nm for  $\text{Ag/Ti/Si}$  (0.1/1/2), followed by 2.75 nm for  $\text{TiO}_2$ , 1.64 nm for  $\text{Ag/Ti/Si}$  (0.1/1/0). The formation of silver nanoparticles was caused by the reduction of  $\text{Ag}^+$  and  $\text{Ag}^0$  during microwave



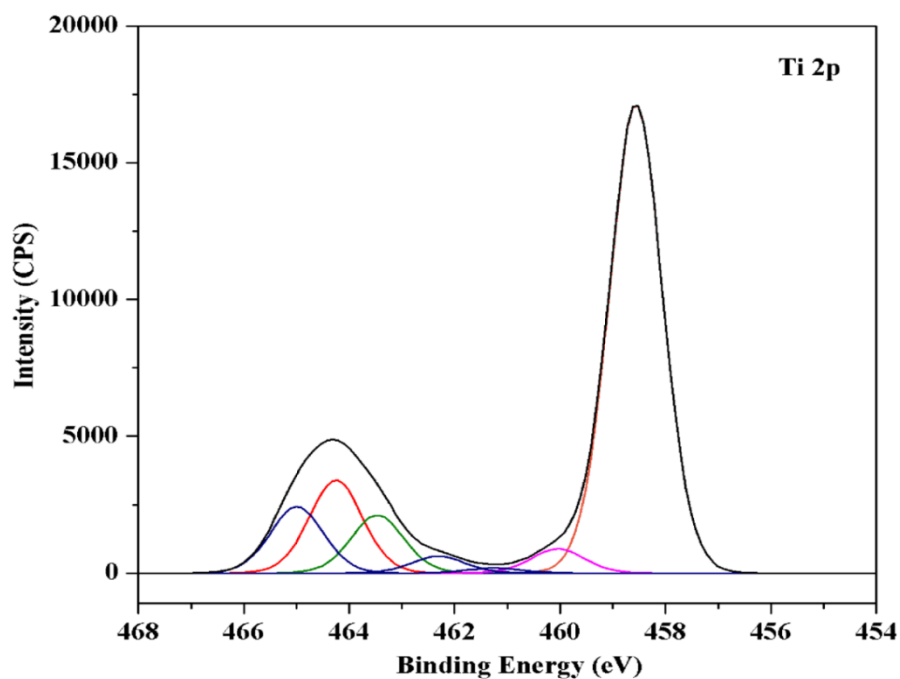
irradiation, as observed from the change of the sol-gel from yellow to dark brown. This result is similar to the study of Viana *et al.* (2013). They reported that Ag clusters grow continuously by heterogeneous nucleation, resulting in the retardation of anatase crystal growth [75]. The results from AFM are in accordance with the results from FESEM as discussed previously.

#### 5.4.5 Chemical composition and state

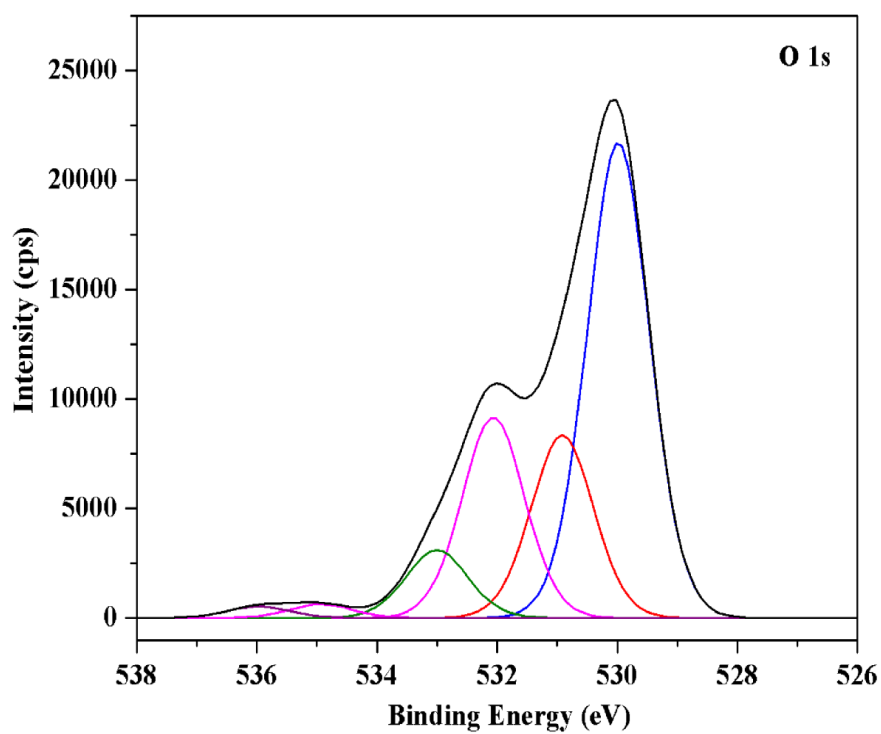
X-ray photoelectron spectroscopy (XPS) is conducted to elucidate the elements and the atomic configuration on the surface of Ag/Ti/Si (0.1/1/2) nanocomposite films. Figure 5.10 displays the typical survey spectra of Ti 2p, Si 2p, O 1s and Ag 3d. It is observed that the Ti and O elements show the strongest peaks, which are expected to be the Ti-O bonding found in crystal lattice of  $\text{TiO}_2$ . In order to determine the chemical state of Ag/Ti/Si (0.1/1/2) nanocomposite film, the high resolution XPS spectra of Ti, Si, O and Ag were analyzed separately as seen in Figure 5.11.



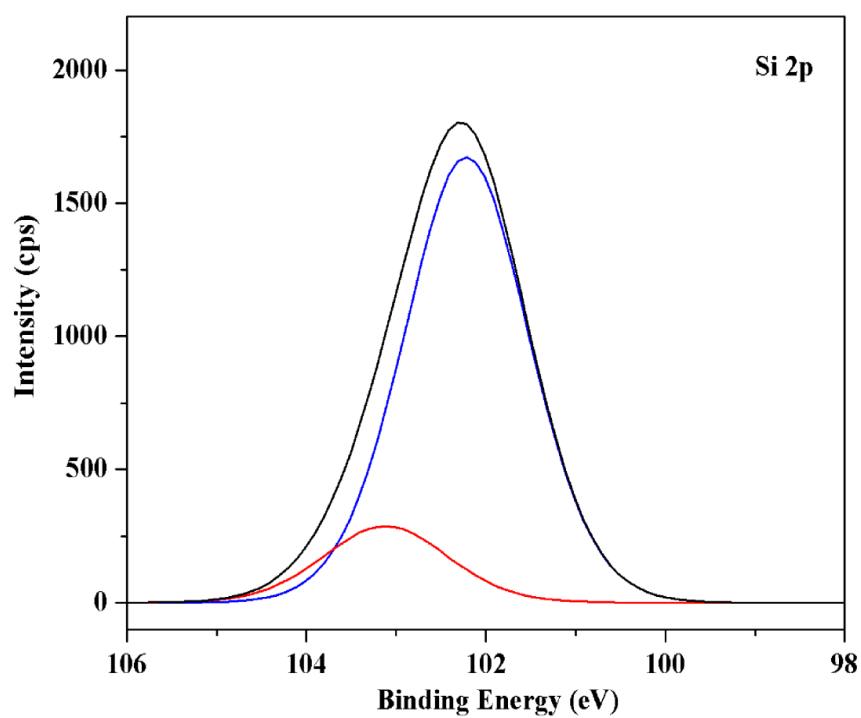
**Figure 5.10** XPS survey spectra of (a)  $\text{TiO}_2$ , (b) Ag/Ti/Si (0.1/1/0) and (c) Ag/Ti/Si (0.1/1/2) films.



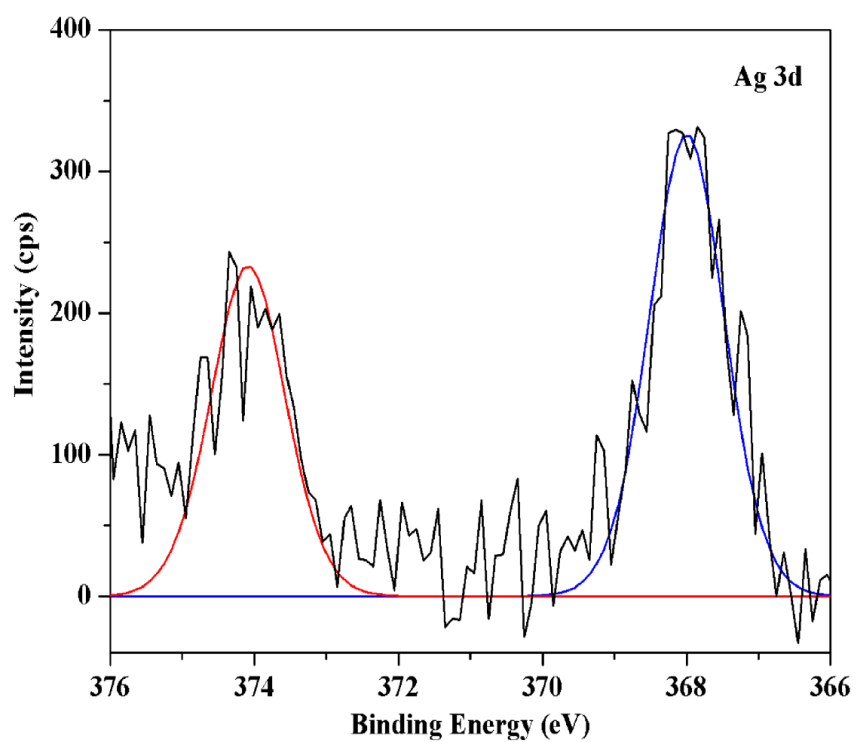
**Figure 5.11** High resolution XPS spectra of Ti 2p on Ag/Ti/Si (0.1/1/2) film.



**Figure 5.12** High resolution XPS spectra of O 1s on Ag/Ti/Si (0.1/1/2) film.



**Figure 5.13** High resolution XPS spectra of Si 2p on Ag/Ti/Si (0.1/1/2) film.



**Figure 5.14** High resolution XPS spectra of Ag 3d on Ag/Ti/Si (0.1/1/2) film.

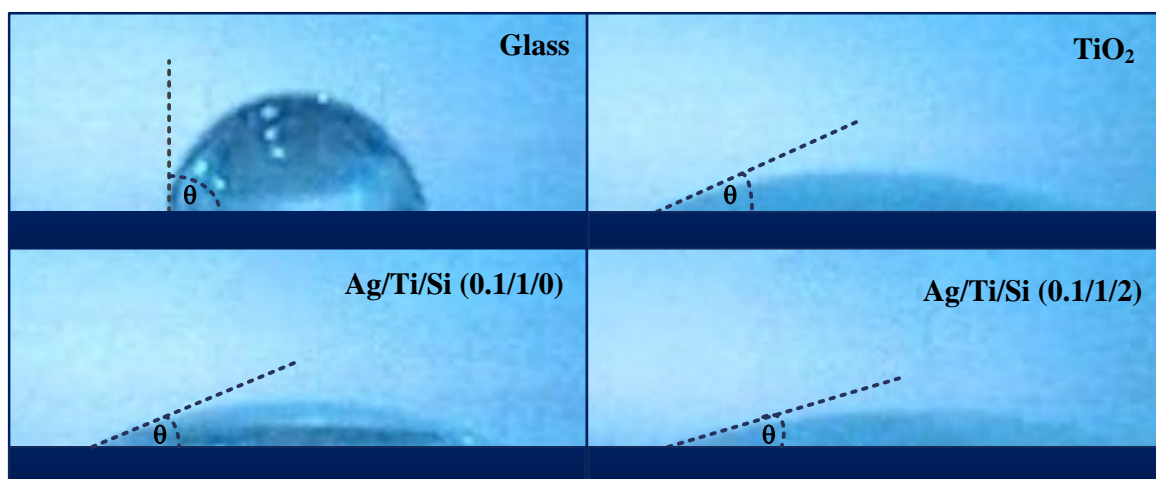
The XPS spectra of Ti 2p spin orbit component located at the bonding energy of 458.6 eV and 464.3 eV correspond to Ti 2p<sub>3/2</sub> and Ti 2p<sub>1/2</sub>, respectively. The strongest peak is Ti 2p<sub>3/2</sub> assigned to tetravalent Ti<sup>4+</sup>. These results are consistent with the literatures reported elsewhere [34, 76]. The XPS spectra of Si 2p comprise of two peaks located at 102.2 eV and 103.1 eV, attributed to siloxane of Ti-O-Si and Si-O-Si linkages and SiO<sub>2</sub>, respectively. This evidence confirms that Si<sup>4+</sup> can replace Ti<sup>4+</sup> in titania octahedral lattice, and vice versa [77]. The XPS spectra of O 1s spectra consist of several peaks in the region from 528 eV to 537 eV. The strong peaks of O 1s appears at 530.0 eV and 532.0 eV are attributed to oxygen in Ti-O-Ti linkage of TiO<sub>2</sub> and OH groups in Ti-OH and Si-OH bonding, respectively. The peak pointed at 531.0 eV is ascribed to Ti-O-Si bonds due to the coordination of Si and Ti atoms in the matrix surface. Another peak at 533.0 eV refers to the oxygen bonding of Si-O-Si linkages [22]. The XPS spectrum of Ag 3d shows the binding energy of Ag at 368.1 eV and 374.1 eV, corresponding to Ag 3d<sub>5/2</sub> and Ag 3d<sub>3/2</sub>, respectively. This is the characteristic of metallic silver (Ag<sup>0</sup>) [23]. The XPS peak of Ag<sup>+</sup> was not found. This result has been suggested by previous research that the Ag<sup>+</sup> specie can be reduced by thermal decomposition to form particles of metallic silver (Ag<sup>0</sup>) [28, 75]. The formation of Ag metal can be described in equation (5.3-5.5) as shown below.



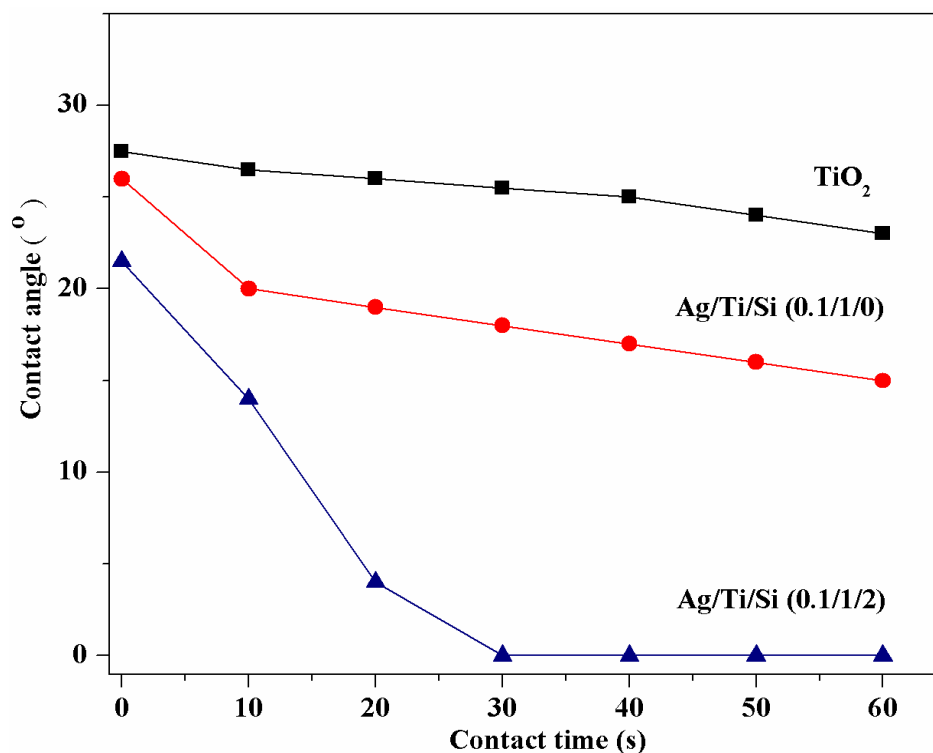
These equations show that after AgNO<sub>3</sub> was dissolved in the Ti precursor solution, Ag<sup>+</sup> ions reacted with the hydroxyl group (OH<sup>-</sup>) from the ethanol solution to form Ag-OH (yellow solution). After irradiation with microwave, Ag<sub>2</sub>O can be reduced with the free radicals, resulting in the change of yellow to brown solution. Finally, the metallic silver (Ag<sup>0</sup>) atoms are produced during calcination, providing a black color in powder sample. The OH radical in solution Ag sol-gel and reduce to Ag<sub>2</sub>O. It was reviewed that metallic Ag can facilitate the electron-hole separation which promotes photocatalytic oxidizing reactivity of TiO<sub>2</sub>. According to XPS results, the possible functional groups that found in the Ag/Ti/Si (0.1/1/2) nanocomposite film are Ti-O-Ti, Si-O-Si, Ti-OH, Si-OH, Ti-O-Si and metallic Ag.

#### 5.4.6 Hydrophilic property of the nanocomposite films

The hydrophilicity of the nanocomposite films was determined from the contact angles, as presented in Figure 5.15. The initial contact angles of glass substrate,  $\text{TiO}_2$ , Ag/Ti/Si (0.1/1/0) and Ag/Ti/Si (0.1/1/2) films were  $90^\circ$ ,  $28^\circ$ ,  $26^\circ$  and  $22^\circ$ , respectively. The contact angles of all films decreased gradually over times in the dark (as seen in Figure 5.15), indicating that the film surfaces are more favorable with water. This is a result of silanol groups (Si-OH) at surface of MCM-41 according to the FTIR result as shown in chapter 4. Interestingly, the contact angles of Ag/TiO<sub>2</sub>/MCM-41 films decreased dramatically from  $22^\circ$  to  $0^\circ$  within 30 s. A zero contact angle represents the complete wetting or called superhydrophilicity [17]. The superhydrophilicity of Ag/TiO<sub>2</sub>/MCM-41 films is mainly attributed from MCM-41. The presence of hydroxyl groups containing in silanol (Si-OH) could enhance the polarity of composite film, leading to a dramatic decrease in the contact angle. More water ( $\text{H}_2\text{O}$ ) can be absorbed on the film surface and more hydroxyl radical ( $\bullet\text{OH}$ ) can be produced and react with organic pollutant during photocatalytic reaction [78]. Additionally, the superhydrophilic film is able to prevent the formation of water droplet dispersed on the film, which is desirable for self-cleaning applications in glass windows and car mirrors.



**Figure 5.15** Contact angle of water droplet on glass substrate,  $\text{TiO}_2$ , Ag/Ti/Si (0.1/1/0) and Ag/Ti/Si (0.1/1/2) films.

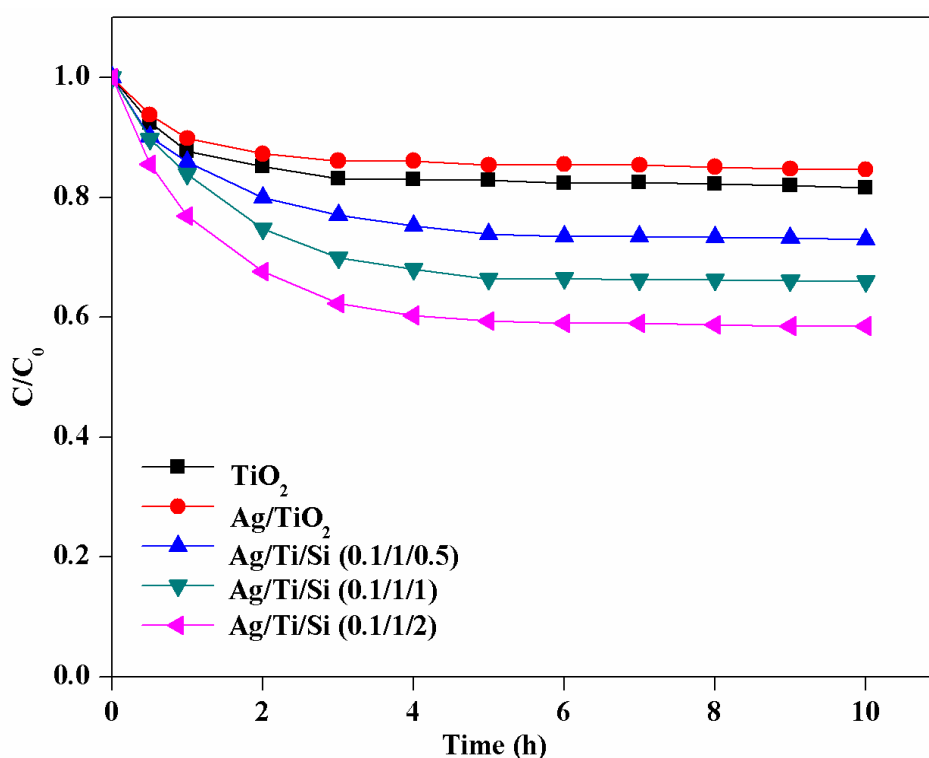


**Figure 5.16** Contact angles of TiO<sub>2</sub>, Ag/Ti/Si (0.1/1/0) and Ag/Ti/Si (0.1/1/2) films at different time intervals.

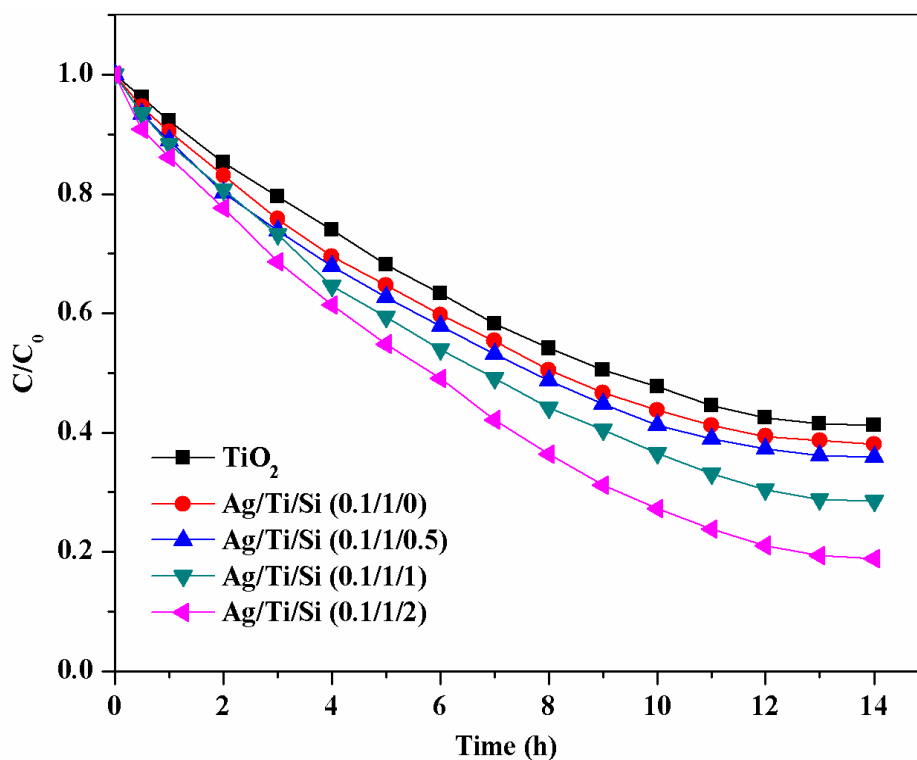
#### 5.4.7 Photocatalytic activity of the nanocomposite film on MB decolorization

The photocatalytic reactivity of the nanocomposite films is evaluated from the photocatalytic decolorization of MB dye under UV and visible light irradiation after adsorption until reaching equilibrium. Figure 5.17 shows the adsorption capacity of MB in the dark by using different photocatalyst films. The adsorption of MB dye reaches its equilibrium within 5 h. The adsorption capacities of the films increase as the MCM-41 loading increases. Among all films, the Ag/Ti/Si (0.1/1/2) film exhibits the highest adsorbability up to 42%. While the adsorbability of MB on pure TiO<sub>2</sub> and Ag/Si/Ti (0.1/1/0) films were only 18% and 15%, respectively. The adsorption results correlated with the surface area as reported from BET analysis. Figure 5.18 shows the photocatalytic decolorization of MB on various photocatalyst films under UV light irradiation. The decolorization efficiencies of films under UV light irradiation within 14 h were arranged in order of Ag/Ti/Si (0.1/1/2) > (0.1/1/1) > (0.1/1/0.5) > (0.1/1/0) > TiO<sub>2</sub> as 81%, 71%, 64%, 62% and 59%, respectively. The result was consistent with the photocatalytic decolorization of MB on films under visible light irradiation. It can be noted that the alone

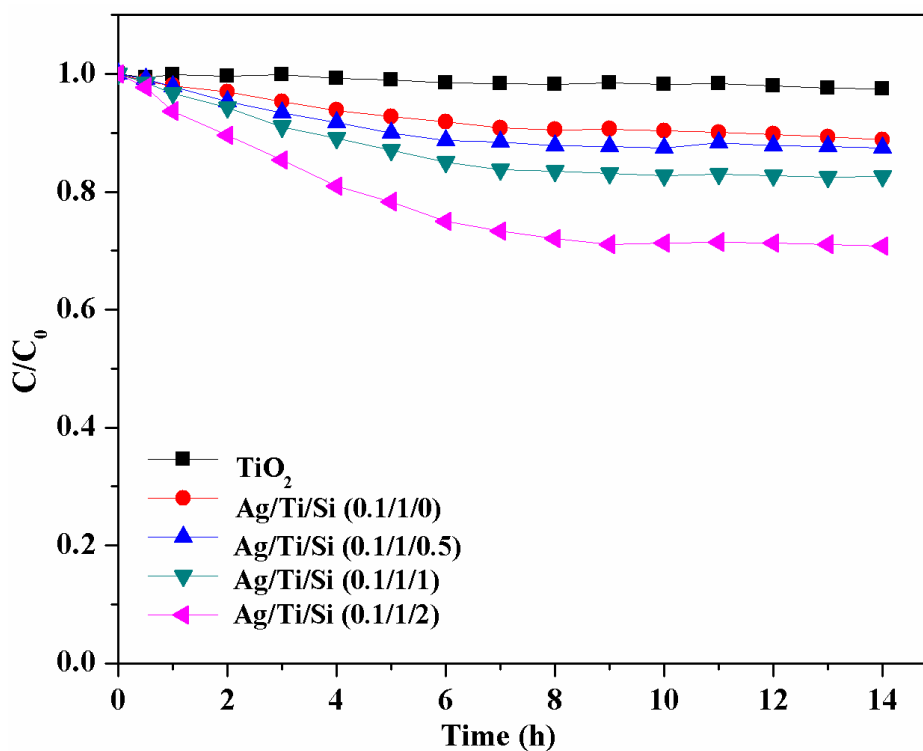
TiO<sub>2</sub> film was inactive under visible light. However, TiO<sub>2</sub> can be significantly improved by incorporating Ag and MCM-41 into its crystalline structure. The decolorization efficiencies of Ag/Ti/Si (0.1/1/0), (0.1/1/0.5), (0.1/1/1), (0.1/1/2) under visible light irradiation within 14 h were increased to 11%, 12%, 13%, 17% and 30%, respectively. Among all films, Ag/Ti/Si (0.1/1/2) gave the highest photocatalytic reactivity under both UV and visible light irradiation.



**Figure 5.17** Adsorption of MB dye on different photocatalyst films in the dark.



**Figure 5.18** Photocatalytic degradation of MB dye on different films with various MCM-41 content under UV light irradiation.



**Figure 5.19** Photocatalytic degradation of MB dye on different films with various MCM-41 content under visible light irradiation.



Additionally, the kinetic reactions of MB decolorization can be described by pseudo-first-order equation, as shown below:

$$\ln \frac{C_0}{C} = kt \quad (5.6)$$

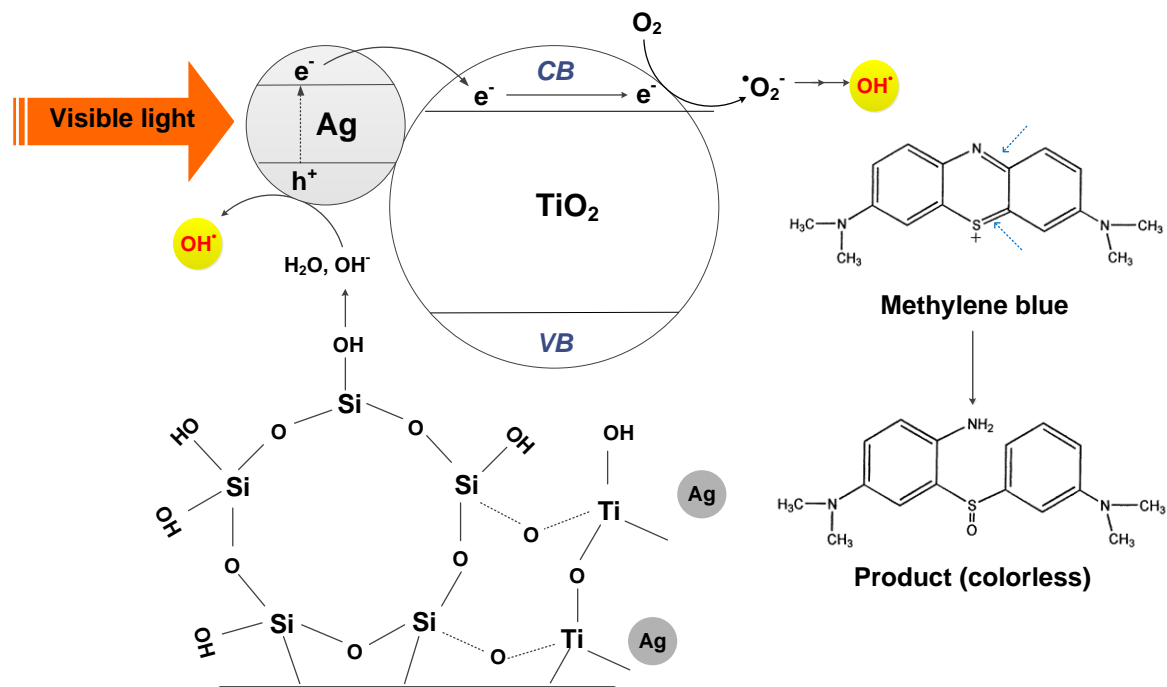
Where  $C_0$  and  $C$  are the initial concentration and the residue concentration after the irradiation of MB solution,  $t$  is a time for irradiation (h), and  $k$  is the kinetic rate constant obtained from the slope of the linear graph. The coefficient determination ( $R^2$ ) of all films was more than 0.9. The reaction rate constants ( $k$ ) and  $R^2$  of all photocatalyst films under UV and visible light are summarized in Table 5.2.

**Table 5.2** Reaction rate constants ( $k$ ) and the coefficient of determination ( $R^2$ ) of all photocatalyst films under UV and visible light irradiation.

Samples	UV light		Visible light	
	$k$ (h <sup>-1</sup> )	$R^2$	$k$ (h <sup>-1</sup> )	$R^2$
TiO <sub>2</sub>	0.076	0.999	0.002	0.953
Ag/Ti/Si (0.1/1/0)	0.088	0.997	0.015	0.987
Ag/Ti/Si (0.1/1/0.5)	0.095	0.990	0.021	0.991
Ag/Ti/Si (0.1/1/1)	0.105	0.998	0.028	0.992
Ag/Ti/Si (0.1/1/2)	0.121	0.994	0.050	0.989

In comparison to UV irradiation, the reaction rate constants ( $k$ ) of MB decolorization by the composite films under visible light are lower. Among all films, the reaction rate constant of pure TiO<sub>2</sub> is the lowest value, only 0.002 h<sup>-1</sup> under visible light and 0.076 h<sup>-1</sup> under UV luminance. When Ag nanoparticle is introduced as a dopant on TiO<sub>2</sub>, the reaction rate constant of the TiO<sub>2</sub> film is improved significantly. The synergistic effect of Ag and MCM-41 on the photocatalytic reactivity of TiO<sub>2</sub> can be determined from the reaction rate constants. The photocatalytic reaction rate constant of the composite film was markedly increased when MCM-41 loading is increased. The Ag/Ti/Si (0.1/1/2) composite film exhibits the highest rate constant of 0.121 h<sup>-1</sup> and 0.050 h<sup>-1</sup> under UV and visible light illuminating, respectively. The mechanisms of MB decolorization under

visible light irradiation by Ag/TiO<sub>2</sub>/MCM-41 nanocomposite films are proposed in Figure 5.20 and equation (5.7-5.15).



**Figure 5.20** Mechanisms of Ag/TiO<sub>2</sub>/MCM-41 nanocomposite on MB degradation irradiated under visible light.

**At conduction band of Ag:**



**At valence band of TiO<sub>2</sub>**



Under visible light irradiation, the electrons of silver nanoparticles jump from the valence band to the conduction band of silver and then migrate to the conduction band of  $\text{TiO}_2$ . The migrated electrons can react with the adsorbed  $\text{O}_2$  to produce highly reactive  $\text{OH}^\bullet$  radicals. The hole ( $h^+$ ) of Ag nanoparticles react with the absorbed  $\text{H}_2\text{O}$  and hydroxyl ions generated from the hydrolysis of some silanols in MCM-41 molecules to produce highly reactive  $\text{OH}^\bullet$  radicals which have the ability to destroy the molecules of MB [17]. It is suggested that  $\text{OH}^\bullet$  radicals attack the  $\text{C}-\text{S}^+=\text{C}$  and  $\text{C}-\text{N}=\text{C}$  groups, and split the  $\text{S}^+=\text{C}$  and  $\text{N}=\text{C}$  double bonds in MB. Thus induces the opening of the central aromatic ring, consequently leading to the colorless product [79]. It is clearly that the roles of MCM-41 are not only enhancing the adsorbability of the film but also providing active hydroxyl species which can facilitate the photocatalytic reaction of  $\text{TiO}_2$ .

## 5.5 Conclusions

This study focused on improving the responsiveness of  $\text{TiO}_2$  to visible light by doping Ag and MCM-41 in the form of nanocomposite powder and film. The main advantages of Ag are reducing band gap energy of  $\text{TiO}_2$  and preventing charge recombination, while MCM-41 enhances the adsorbability of the nanocomposite film and supplies active hydroxyl radicals during photocatalysis. The kinetic rate constant of MB dye on the composite films followed pseudo first-order reaction law ( $R^2 > 0.9$ ), arranged in the order of  $\text{Ag/Ti/Si (0.1/1/2)} > \text{Ag/Ti/Si (0.1/1/1)} > \text{Ag/Ti/Si (0.1/1/0.5)} > \text{Ag/Ti/Si (0.1/1/0)} > \text{TiO}_2$ . The  $\text{Ag/Ti/Si (0.1/1/2)}$  exhibited the highest photocatalytic decolorization of methylene blue, with an efficiency of 81% under UV, and 30% under visible light irradiation. Due to its highest visible light responsive property, the  $\text{Ag/Ti/Si (0.1/1/2)}$  nanocomposite film was be utilized as a photocatalyst film for environmental applications. The experimental procedure and the detailed result of indoor air treatment and antibacterial property will be discussed in next chapter.

## CHAPTER VI

### PHOTOCATALYTIC ACTIVITY OF Ag/TiO<sub>2</sub>/MCM-41 NANOCOMPOSITE FILMS TO INDOOR AIR TREATMENT

#### 6.1 Introduction

According to Chapter 5, the performances of the Ag/TiO<sub>2</sub>/MCM-41 nanocomposite films exhibited high responsiveness to visible light. The photocatalytic activity of nanocomposite films was successfully tested with organic compound in an aqueous solution. In particular, the Ag/Ti/Si (0.1/1/2) film gave the highest photocatalytic decolorization of methylene blue dye under both UV and visible light irradiation. In this chapter, the application of Ag/TiO<sub>2</sub>/MCM-41 nanocomposite films on the photocatalytic reactivity for indoor air treatment was studied. The removal of gaseous benzene, an indoor air pollutant, was tested by the photocatalytic reaction using Ag/TiO<sub>2</sub>/MCM-41 nanocomposite films in a batch and a simulated indoor air system. In addition, the antibacterial activity of a gram-negative *Escherichia coli* (*E. coli*) was examined using the Ag/Ti/Si (0.1/1/2) nanocomposite film under visible light irradiation.

#### 6.2 Research objectives

This study aims to investigate the photocatalytic activities of Ag/TiO<sub>2</sub>/MCM-41 nanocomposite films applied for benzene gas treatment and antibacterial activity under visible light irradiation.

#### 6.3 Experimental procedure

The photocatalyst film was tested for the photodegradation of benzene gas in the batch system and simulated indoor air system under UV and visible light irradiation. The optimal photocatalyst film was tested for antibacterial activity testing with *Escherichia coli* ATCC 8739 under visible light irradiation.

##### 6.3.1 Benzene gas treatment in batch system

In a preliminary, the batch system was studied in order to screen the most promising for benzene gas treatment in a simulated indoor air system. The photoreactor

was constructed in a rectangular solid with a volume of 10 L (23.0 cm × 32.5 cm × 13.5 cm) and equipped with two fluorescence lamps (8W Philips, cool white 4100K,  $\lambda = 435$  nm). The diagram of batch photoreactor was shown in Figure 3.2. The photocatalyst films were arranged in the photoreactor (total surface area as 0.19 m<sup>2</sup>) with a distance of 10 cm to the light sources. 3.6  $\mu$ L of benzene reagent (99.7%) was injected into the batch reactor and volatilized to the concentration of 100 ppm. The photocatalytic degradation rate of gaseous benzene on the various photocatalyst films was firstly determined by turning on the fluorescence lamps at the beginning. The concentration change of benzene gas was measured every 30 min. After that, the promising nanocomposite films was studied for the adsorption and photocatalysis mechanisms of benzene gas by tuning off and turning on the fluorescence lamps.

### 6.3.2 Photocatalytic measurement of benzene gas in simulated indoor air system

The simulated indoor air system consists of the rectangular photoreactor constructed by acrylic sheets with a thickness of 0.5 cm. An axial fan was used to circulate gas in the simulated indoor air system. Either 4 UV lamps (8 W Philips,  $\lambda = 254$  nm, light intensity = 2.17 W m<sup>-2</sup>) or 4 fluorescent lamps (8 W Philips, cool white 4100 K,  $\lambda = 435$  nm, light intensity = 15,400 Lux) were used as UV and visible light sources, respectively. The two lamps were fixed at above and other two lamps were fixed at bottom of the photoreactor. The six photocatalyst films of TiO<sub>2</sub>, Ag/TiO<sub>2</sub> or Ag/TiO<sub>2</sub>/MCM-41 with the size of 10 × 15 cm were placed vertically in the left, middle and right sides of the photoreactor (total active area = 0.12 m<sup>2</sup>). The distance between the films and the light source lamps was 1.0 cm. The schematic diagram of the simulated indoor air system was shown as following Figure 3.3. The benzene gaseous in the chamber was circulated through the rectangular photoreactor by axial fan which set at outlet of the photoreactor for air flowing after stand for 1 h in the dark. The initial concentration of benzene gas without lightening condition was firstly measured. Then, UV or fluorescence lamps were turned on. The photocatalytic degradation rate of benzene was studied. The kinetic rate constant and the reaction rates in the unit of (h<sup>-1</sup>) and (g L<sup>-1</sup> h<sup>-1</sup>) were then calculated.

### 6.3.3 Antiantibacterial activity measurement

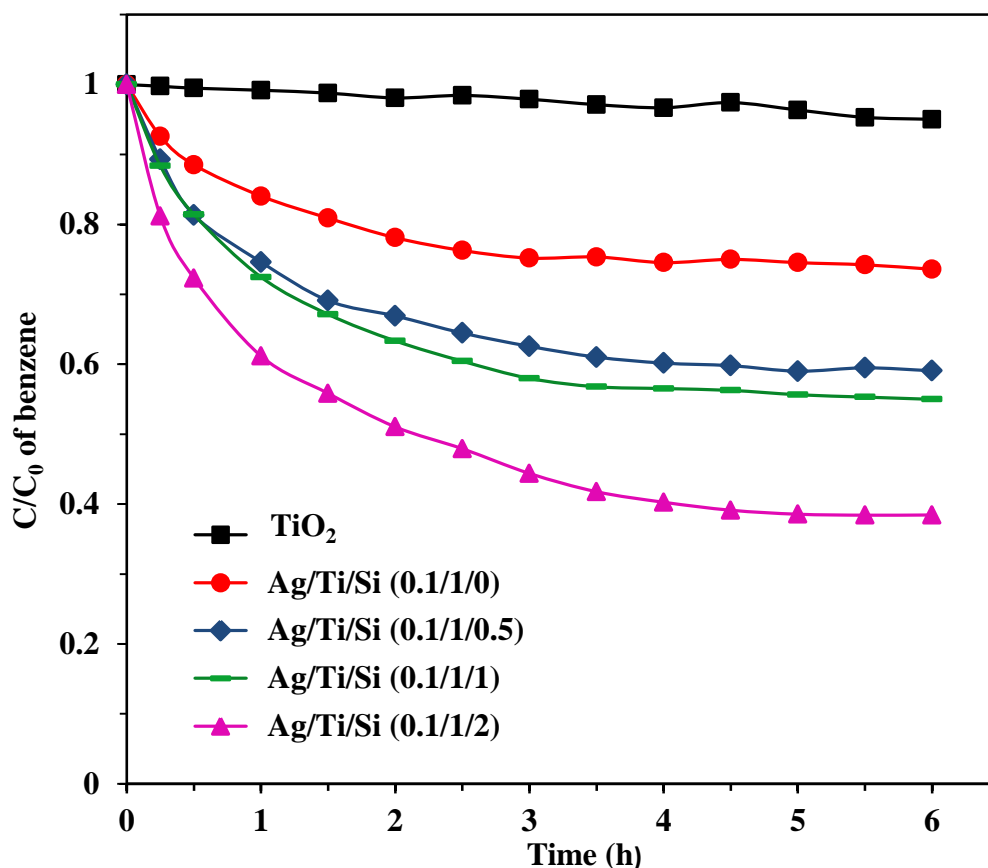
The antibacterial activity of TiO<sub>2</sub> and Ag/TiO<sub>2</sub>/MCM-41 photocatalyst films was examined by *Escherichia coli* (*E. coli*, ATCC 8739) obtained from Thailand Institute of Scientific and Technological Research. The method was modified from the Japanese Industrial Standard JIS Z 2801:2000 method compared to a glass blank [68]. The diagram

of antimicrobial testing was described and exhibited in Figure 3.4. The  $1 \times 10^6$  CFU mL<sup>-1</sup> of *E. coli* was prepared in 1/500 Luria broth medium. Four hundred microliters of aliquot was dropped onto the test films and the glass blank which the size of test films was  $25 \times 25$  mm and covered with parafilm (size as  $20 \times 20$  mm). Next, all samples were incubated under fluorescent light (15 W) at  $25 \pm 5$  °C for 2 h. After incubation, these films were separated from the surface and transferred to individual containers containing an aliquot (10 mL) of a neutraliser validated for the biocide in each film. The numbers of colony forming units within the resulting suspensions were enumerated. This testing was replicated in another two pieces per each sample films. The glass blank was also processed in this manner prior to incubation to provide base-line data.

## 6.4 Results and discussion

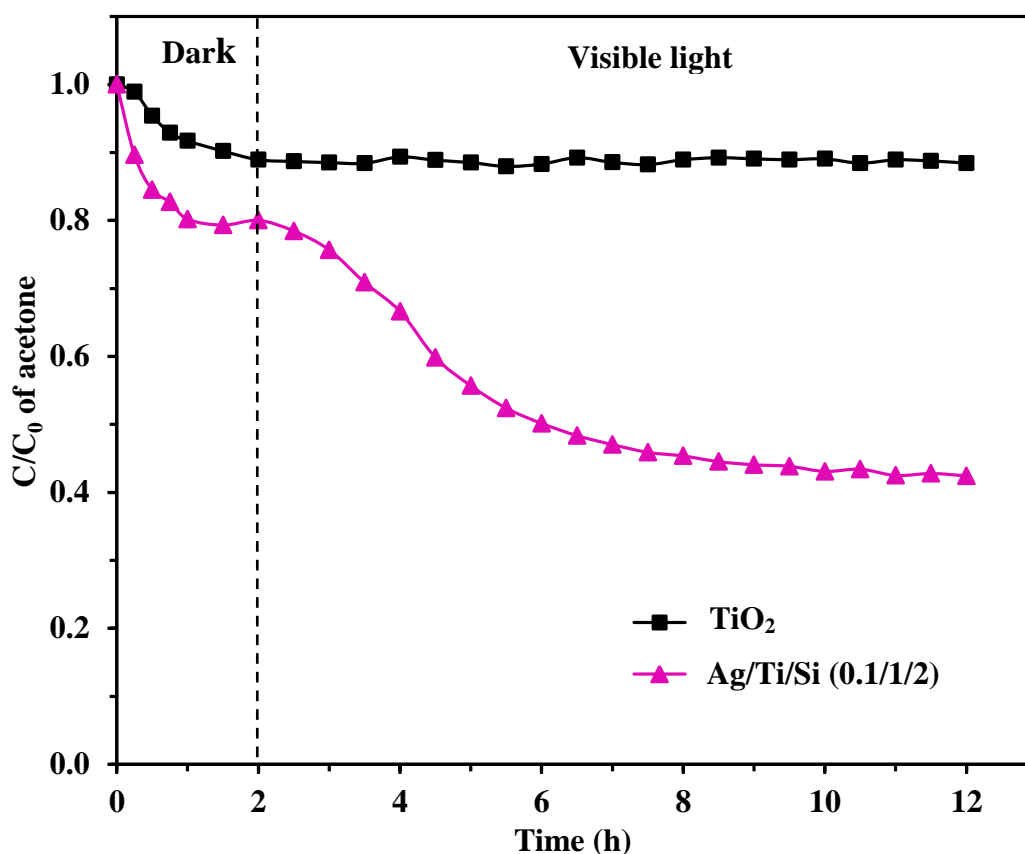
### 6.4.1 Photodegradation of benzene in batch system

The photodegradation of benzene with initial concentration of 100 ppm on photocatalyst films with total active area as  $0.19 \text{ m}^2$  in a batch reactor are represented in Figure 6.1. The photocatalytic activity of all films was compared under visible light irradiation until 6 h. The result was when increasing the amount of MCM-41 on Ag/TiO<sub>2</sub>/MCM-41 film, the photocatalytic activity also increased. However, the photolysis of benzene gas was not occurred under visible light irradiation. The photodegradation efficiencies of benzene on the photocatalyst films was arranged in order to Ag/Ti/Si (0.1/1/2) > Ag/Ti/Si (0.1/1/1) > Ag/Ti/Si (0.1/1/0.5) > Ag/Ti/Si (0.1/1/0) > TiO<sub>2</sub> as 62%, 45%, 41%, 27% and 5%, respectively. The highest amount of MCM-41 on the nanocomposite film, Ag/Ti/Si (0.1/1/2), gave the highest efficiency on benzene degradation.



**Figure 6.1** Photocatalytic degradation rates of gaseous benzene on different films under visible light irradiation for 6 h in a batch system.

In order to investigate the adsorption and the photocatalysis mechanisms of benzene gas treatment by Ag/Ti/Si (0.1/1/2), the experiment was conducted by turning the fluorescence lamps off and on, respectively. The results are given in Figure 6.2. The adsorption mechanism of benzene gas on TiO<sub>2</sub> and Ag/Ti/Si (0.1/1/2) films was reached to the equilibrium for 2 h in the dark. The reduction of benzene gas by adsorption on photocatalyst films was 22% for Ag/Ti/Si (0.1/1/2) films and 11% for TiO<sub>2</sub> films. After adsorption, the photodegradation of benzene on photocatalyst films was examined under visible light irradiation until 10 h. The results showed that the photodegradation efficiency of benzene on Ag/Ti/Si (0.1/1/2) films was up to 40% within 10 h. This indicated that the photocatalysis occurs even under visible light irradiation. On the other hand, the degradation of benzene gas was not changed after visible light irradiation, indicating that pure TiO<sub>2</sub> films was inactive under visible light.



**Figure 6.2** Degradation rate of gaseous benzene on TiO<sub>2</sub> and Ag/Ti/Si (0.1/1/2) films under dark and visible light irradiation in a batch system.

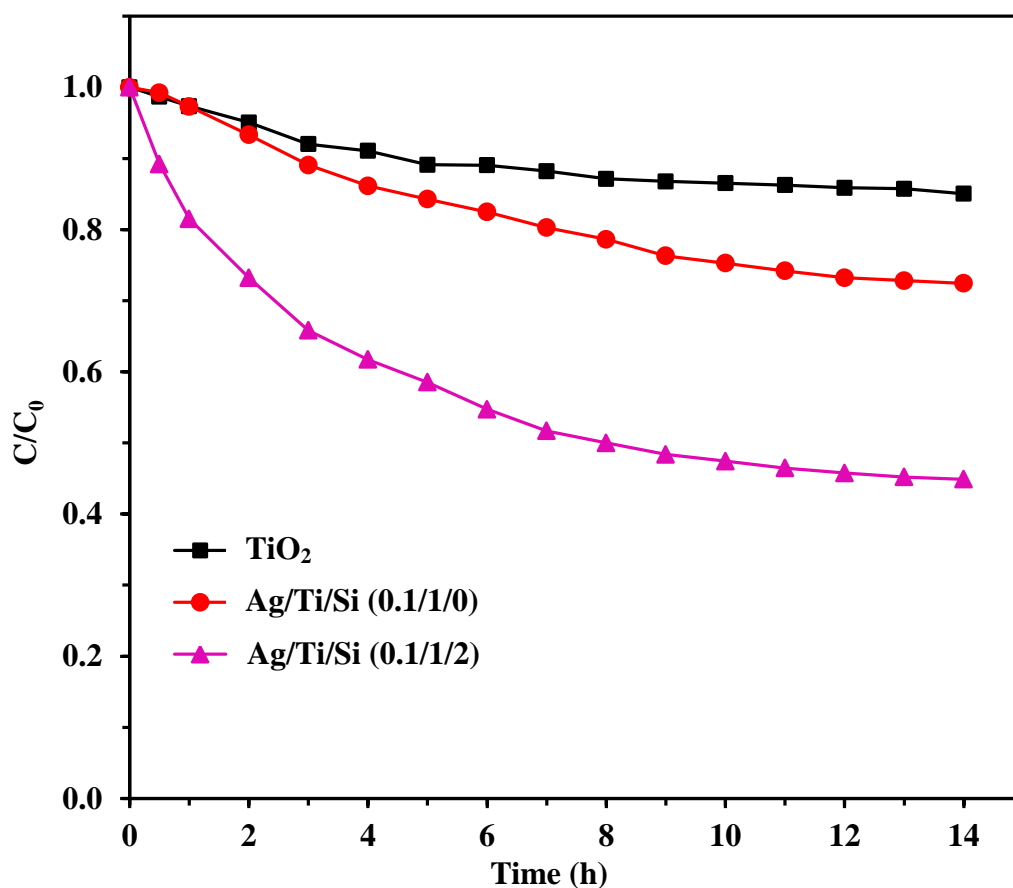
#### 6.4.2 Photodegradation of benzene in simulated indoor air process

##### 6.4.2.1 Effect of Ag and MCM-41 on the photocatalytic reactivity of TiO<sub>2</sub>

The photocatalytic activity of TiO<sub>2</sub>, Ag/Ti/Si (0.1/1/0) and Ag/Ti/Si (0.1/1/2) films on gaseous benzene degradation under visible light irradiation in the simulated indoor air system is shown in Figure 6.3. The photodegradation efficiencies were arranged in order of Ag/Ti/Si (0.1/1/2) (55%) > Ag/Ti/Si (0.1/1/0) (28%) > TiO<sub>2</sub> (15%). This result is consistent with their UV-Vis absorbances as mentioned earlier. The absorbance intensity under the visible light region of the photocatalyst film was increased substantially by incorporating the Ag and MCM-41 to TiO<sub>2</sub>. The photocatalytic reactivity of TiO<sub>2</sub> was increased 2.7 times by incorporating Ag and MCM-41 into TiO<sub>2</sub>. The photodegradation of gaseous benzene by Ag/Ti/Si (0.1/1/2) nanocomposite film under visible light irradiation can be explained as follows. Gaseous benzene adsorbs on the film surface due to its partial pressure gradient. The nanocomposite film simultaneously absorbs energy from visible



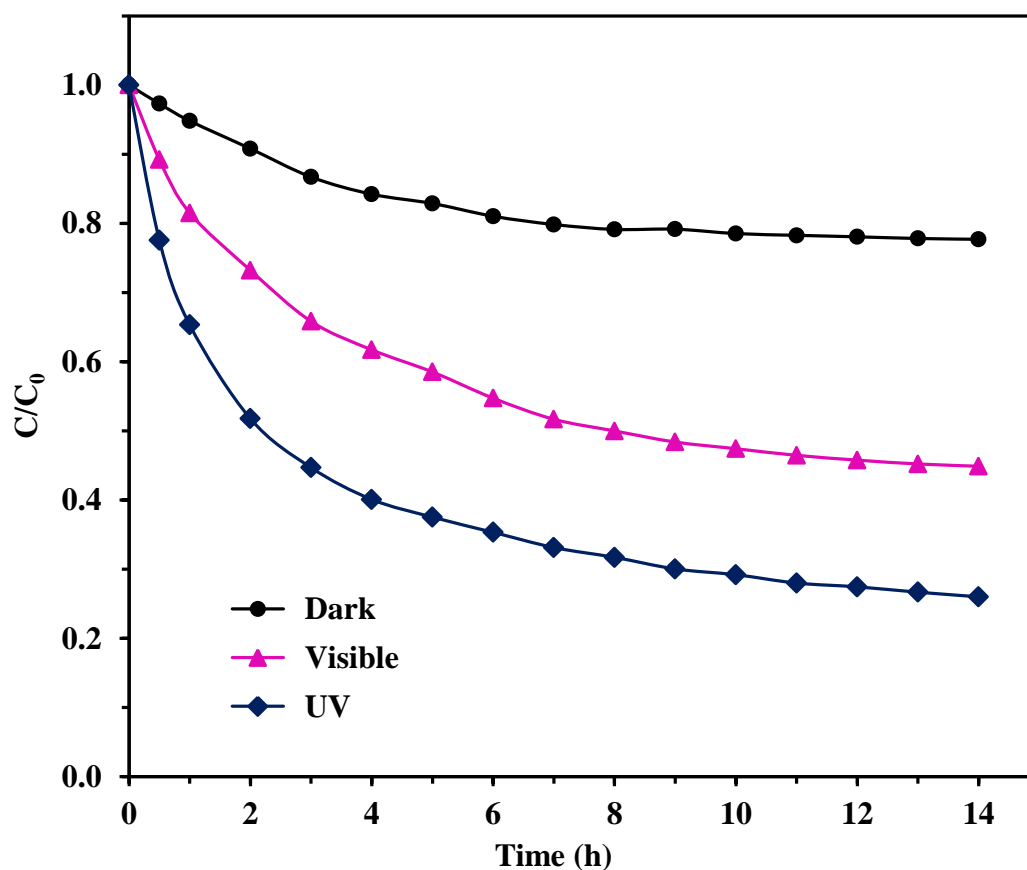
light. After that, the electrons of Ag nanoparticles are excited to its conduction band and then migrate to the conduction band of  $\text{TiO}_2$ . This phenomenon occurs due to the surface plasmon resonance of Ag. The excited electrons at  $\text{TiO}_2$  conduction band react with oxygen radicals to produce super oxide radicals. Meanwhile, Ag holes ( $h^+$ ) react with the adsorbed  $\text{H}_2\text{O}$  providing hydroxyl ions. Both superoxides and hydroxyl ions can further oxidize benzene to phenol, 1,4-benzoquinone and hydroquinone [80]. The role of Ag is not only reducing band gap energy for photocatalysis but also preventing the  $e^-/h^+$  pair recombination [29]. While MCM-41 promotes the adsorbability of benzene on the film and its silanol groups ( $\text{Si-OH}$ ) can provide highly reactive hydroxyl radicals supporting the photocatalytic reaction [32].



**Figure 6.3** Photocatalytic degradation rates of gaseous benzene by different films under visible light irradiation.

#### 6.4.2.2 Effect of light sources on the Ag/Ti/Si (0.1/1/2) films

The performances of benzene photodegradation by Ag/Ti/Si (0.1/1/2) films under different light sources are shown in Figure 6.4. The adsorption capacity of Ag/Ti/Si (0.1/1/2) films was carried out in the dark. While, the overall benzene photodegradation efficiency of Ag/Ti/Si (0.1/1/2) films was investigated under UV and visible light irradiation. In the dark, the benzene adsorption reached its equilibrium within 8 h. The benzene removal caused by adsorption mechanism was approximately 23%. Under UV and visible light irradiation, the photodegradation efficiencies of benzene increased to 74% and 55%, respectively. This result is caused by a strong UV and visible light absorption of Ag/Ti/Si (0.1/1/2) film, which promote the photocatalytic reaction of the film.



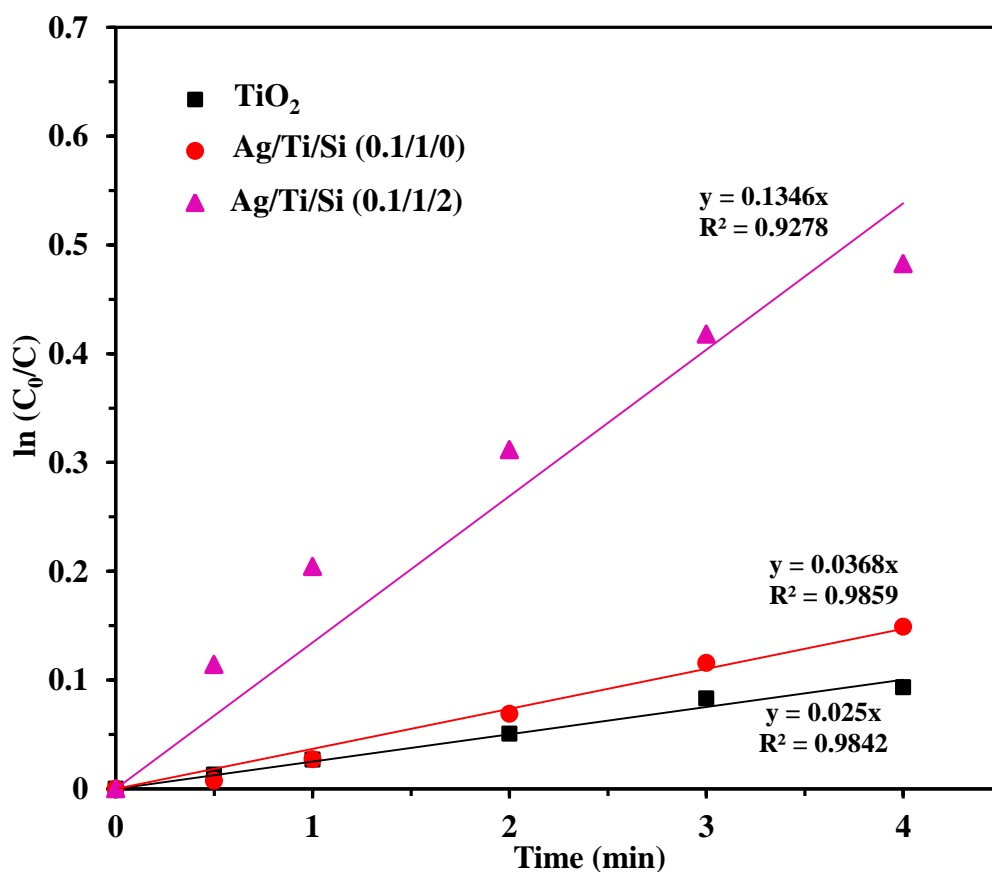
**Figure 6.4** Removal of gaseous benzene by adsorption (in the dark) and photocatalytic activity of Ag/Ti/Si (0.1/1/2) films under UV and visible light irradiation.

The kinetic reactions of benzene degradation using the nanocomposite films were described by the pseudo-first-order equation and the reaction rates ( $r$ ) were determined as follows:

$$\ln\left(\frac{C_0}{C_t}\right) = k_a t \quad (6.1)$$

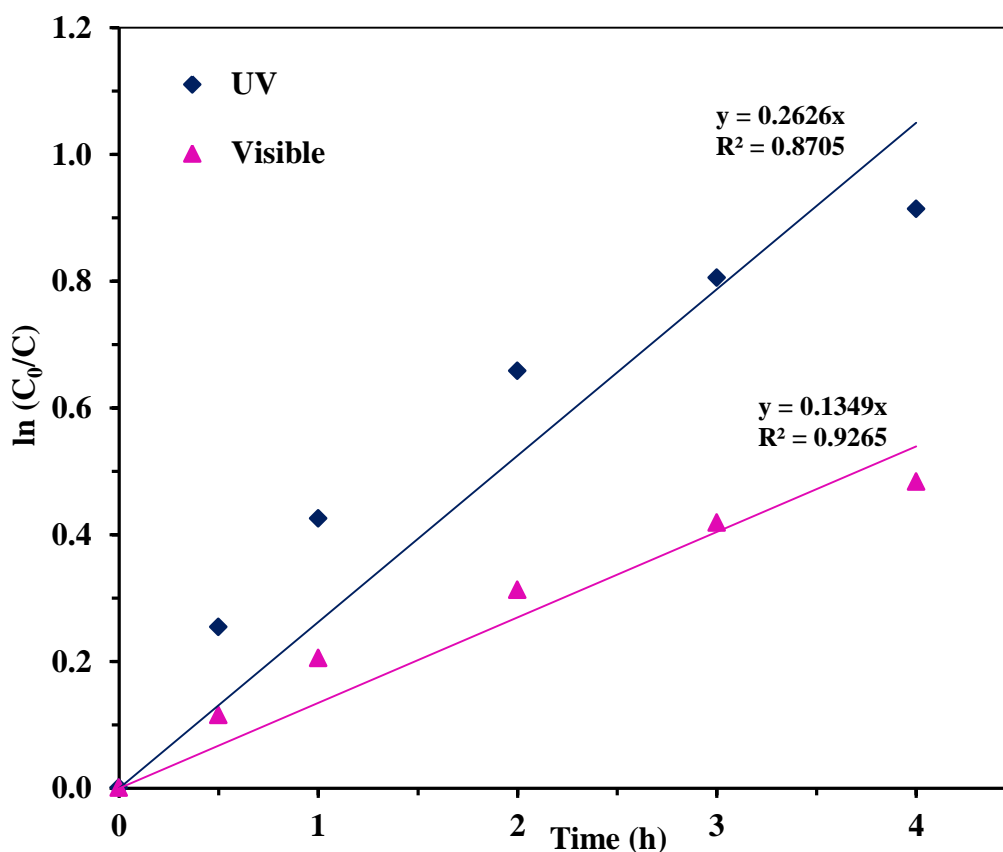
$$r = k_a C_t^n \quad (6.2)$$

Where  $C_0$  is the initial concentration of benzene,  $C_t$  is the residue concentration of benzene,  $k_a$  is the apparent kinetic constant ( $\text{h}^{-1}$ ),  $t$  is the irradiation time (h),  $r$  is the reaction rate ( $\text{g L}^{-1} \text{h}^{-1}$ ) and  $n$  is the reaction order ( $n = 1$  for the first-order equation).



**Figure 6.5** Kinetic pseudo-first-order models of gaseous benzene photodegradation by different photocatalyst films under visible light irradiation.

The kinetic models for the photocatalytic degradation of gaseous benzene on different photocatalyst films under visible light irradiation are shown in Figure 6.5. All linear graphs were fit with the pseudo-first-order reaction ( $R^2 > 0.90$ ). From Table 6.1, the kinetic rate constants ( $k_a$ ) of  $\text{TiO}_2$ ,  $\text{Ag/Ti/Si}$  (0.1/1/0) and  $\text{Ag/Ti/Si}$  (0.1/1/2) films irradiated under visible light were 0.015, 0.025 and 0.135  $\text{h}^{-1}$  and their degradation rates ( $r$ ) were 0.273, 0.609 and 6.321  $\text{g L}^{-1} \text{h}^{-1}$ , respectively. It is noticed that the reaction rate of  $\text{TiO}_2$  films under visible light was increased up to 23 times when incorporating Ag and MCM-41 in the  $\text{TiO}_2$  films. Figure 6.6 shows the comparative kinetic models of  $\text{Ag/Ti/Si}$  (0.1/1/2) films irradiated under UV and visible light irradiation. The kinetic rate constants and the degradation rates were summarized in Table 6.1. Under UV light, the kinetic rate constant ( $k_a$ ) and the degradation rate ( $r$ ) of  $\text{Ag/Ti/Si}$  (0.1/1/2) films were 0.263  $\text{h}^{-1}$  and 12.314  $\text{g L}^{-1} \text{h}^{-1}$ , respectively. These values were slightly more than two times as high under visible light irradiation.



**Figure 6.6** Kinetic pseudo-first-order models of gaseous benzene photodegradation on  $\text{Ag/Ti/Si}$  (0.1/1/2) films under UV and visible light irradiation.

**Table 6.1** Kinetic parameters determined from the pseudo-first-order models of gaseous benzene photodegradation by different photocatalyst films under UV and visible light irradiation.

Samples	Light sources	Kinetic parameters		
		$k_a$ (h <sup>-1</sup> )	$r$ (g L <sup>-1</sup> h <sup>-1</sup> )	$R^2$
TiO <sub>2</sub>	Visible	0.015	0.273	0.982
Ag/Ti/Si (0.1/1/0)	Visible	0.025	0.609	0.984
Ag/Ti/Si (0.1/1/2)	Visible	0.135	6.321	0.928
Ag/Ti/Si (0.1/1/2)	UV	0.263	12.314	0.871

#### 6.4.3 Antimicrobial activity

The antimicrobial activities of Ag/Ti/Si (0.1/1/2) nanocomposite film against gram-negative of *E. coli* was evaluated at room temperature (25 °C) under fluorescence light for 2 h. The number of colony forming units (CFU) was counted and compared with untreated film (glass substrate). The antimicrobial activity and the relative reduction of viable *E. coli* on TiO<sub>2</sub> and Ag/Ti/Si (0.1/1/2) films were calculated from the difference between the number of colony forming units (CFU) on the surface of the photocatalyst films and that on the glass blank using Equations (6.3-6.4).

$$R = \log \left( \frac{A}{B} \right) \quad (6.3)$$

$$\%R = \left( \frac{A - B}{A} \right) \times 100\% \quad (6.4)$$

Where  $R$  is the value of antimicrobial activity,  $A$  is the average of the number of viable cells of bacteria on the glass blank after irradiated under visible light irradiation for 2 h,  $B$  is the average of the number of viable cells of bacteria on the photocatalyst films after irradiation under visible light for 2 h and  $\%R$  is the percentage reduction of viable *E. coli* (%).

Table 6.2 presents the percentage reduction ( $\%R$ ) of viable *E. coli* using TiO<sub>2</sub> and Ag/Ti/Si (0.1/1/2) nanocomposite film. In comparison to the glass blank, the Ag/Ti/Si

(0.1/1/2) nanocomposite film exhibited the highest relative reduction (%R) of *E. coli* (98.2%). While the TiO<sub>2</sub> film had a 54.5% relative reduction (%R) of *E. coli*. The relative antibacterial activity of Ag/Ti/Si (0.1/1/2) nanocomposite film was 1.7 greater than that of alone TiO<sub>2</sub> film about 6 times. These results indicate that the Ag/Ti/Si (0.1/1/2) film had a stronger antimicrobial activity under visible light than the pure TiO<sub>2</sub>. Normally, the disinfection of *E. coli* can be merely performed by TiO<sub>2</sub> film. Ashkaran *et al.* (2011) reported that the alone TiO<sub>2</sub> particle showed a weak antibacterial activity under visible light irradiation. However, when introducing silver to TiO<sub>2</sub>, the number of viable bacteria was decreased significantly [16]. However, the removal efficiency of *E. coli* can be increased twice when incorporating Ag and MCM-41 into TiO<sub>2</sub> film. This effect is attributed to the role of Ag metal (Ag<sup>0</sup>), which can be oxidized to Ag<sup>+</sup> by hydroxyl ions during photocatalytic reaction [81]. Silver ions (Ag<sup>+</sup>) can penetrate inside the cell membrane of *E. coli* and react with phosphorous and sulphur compounds in DNA and enzyme, leading to the inhibition of bacteria growth [20, 51]. MCM-41 also plays an important role in the disinfection process. Hydroxyl groups generated from silanol bonds (Si-OH) in the MCM-41 structure can facilitate the redox conversion of Ag<sup>0</sup> to Ag<sup>+</sup>, resulting in the increase of antibacterial activity of TiO<sub>2</sub> film.

**Table 6.2** Results of antibacterial testing for *E. coli* reduction by different photocatalytic films after incubation under fluorescent light for 2 h.

Test types	Glass blank	TiO <sub>2</sub>	Ag/Ti/Si (0.1/1/2)
Number of viable cells (CFU)	5.50E+05	2.50E+05	0.1E+05
Antibacterial activity (relative)	0	0.3	1.7
%R	0	54.5	98.2

## 6.5 Conclusions

A Ag/TiO<sub>2</sub>/MCM-41 nanocomposite film with a molar ratio of Ag/Ti/Si (0.1/1/2) was successfully applied for benzene gas treatment in both batch and simulated indoor air systems and for antibacterial testing. The photodegradation of gaseous benzene and antibacterial activity were investigated under visible light irradiation. The Ag/Ti/Si

(0.1/1/2) films provide the best performance in the photodegradation of benzene gas under both UV and visible light irradiation due to the synergistic effect of Ag, MCM-41 on the photocatalytic reactivity of  $\text{TiO}_2$ . The degradation efficiency of gaseous benzene under visible irradiation was enhanced 55% by incorporating Ag and MCM-41 into  $\text{TiO}_2$ . The rate reactions of all films fit well with kinetic pseudo first-order model. The kinetic rate constants ( $k_a$ ) and rate reaction ( $r$ ) on photodegradation of gaseous benzene by Ag/Ti/Si (0.1/1/2) films was  $0.135 \text{ h}^{-1}$  and  $6.321 \text{ g L}^{-1} \text{ h}^{-1}$ , respectively. The reaction efficiency of gaseous benzene on Ag/Ti/Si (0.1/1/2) films under visible light irradiation could increase up to 9 times when compared with alone  $\text{TiO}_2$  films.

The roles of Ag were to reduce the band gap energy of  $\text{TiO}_2$  and to prevent charge recombination, while MCM-41 enhances the adsorbability of the nanocomposite films, and supplies active hydroxyl radicals during photocatalysis. The percentage reduction (%R) of viable *E. coli* under visible light irradiation of Ag/Ti/Si (0.1/1/2) film was increased up to 98.2% due to the acceleration of Ag transformation to  $\text{Ag}^+$  by photocatalytic reaction. Thus, the Ag/ $\text{TiO}_2$ /MCM-41 nanocomposite film performs as a smart film for indoor air treatment due to its applications on VOCs gas treatment and antibacterial activity under visible light irradiation.

## CHAPTER VII

### CONCLUSIONS AND RECOMMENDATIONS FOR FUTURE WORKS

#### 7.1 Conclusions

This research can be concluded make the following:

##### 7.1.1 Visible-light responsive Ag/TiO<sub>2</sub>/MCM-41 nanocomposite films

Ag/TiO<sub>2</sub>/MCM-41 nanocomposite films can be successfully prepared by two sequence method via a microwave-assisted sol-gel technique to active under visible light irradiation. The characterization results indicated the synergistic effect of Ag, TiO<sub>2</sub> and MCM-41 on the photocatalytic reactivity of the Ag/TiO<sub>2</sub>/MCM-41 nanocomposite film. The porosity and photocatalytic reactivity of TiO<sub>2</sub> under visible light can be improved by incorporating Ag and MCM-41 into the TiO<sub>2</sub> lattice. The main advantages of Ag are to reduce the band gap energy of TiO<sub>2</sub> and to prevent charge recombination, while MCM-41 enhances the adsorbability of the nanocomposite films, and supplies active hydroxyl radicals during photocatalysis. The photocatalytic reactivity of nanocomposite films was tested with the methylene blue decolorization under UV and visible light irradiation. The synergistic effect of Ag and MCM-41 on the photocatalytic reactivity of TiO<sub>2</sub> was determined from the reaction rate constant, which increases markedly when MCM-41 loading increases. The Ag/Ti/Si (0.1/1/2) composite film exhibits the highest rate constants under both UV and visible light illuminating (0.121 h<sup>-1</sup> and 0.050 h<sup>-1</sup>, respectively). Due to its visible light responsive property and high adsorptive capacity, the Ag/TiO<sub>2</sub>/MCM-41 nanocomposite film can be utilized as a photocatalyst for various environmental applications, especially for indoor air treatment.

##### 7.1.2 Environmental applications of Ag/TiO<sub>2</sub>/MCM-41 nanocomposite films

The applications of the Ag/TiO<sub>2</sub>/MCM-41 nanocomposite films for indoor air treatment from gaseous benzene removal and antibacterial activity were investigated. The degradation efficiency of gaseous benzene under visible light irradiation was carried out in the batch and the simulated indoor air systems. Ag/Ti/Si (0.1/1/2) nanocomposite film exhibited the highest benzene photodegradation efficiency under visible light irradiation due to the synergistic effect of Ag/TiO<sub>2</sub>/MCM-41 nanocomposite films on the photocatalytic reactivity. The photodegradation efficiency of gaseous benzene under visible irradiation was 55% by incorporating Ag and MCM-41 into TiO<sub>2</sub>. In the simulated



indoor air system, the rate reactions of all films fit well with the kinetic pseudo-first-order model. The kinetic rate constants ( $k_a$ ) and rate reaction ( $r$ ) on a photodegradation of gaseous benzene by Ag/Ti/Si (0.1/1/2) films was  $0.135 \text{ h}^{-1}$  and  $6.321 \text{ g L}^{-1} \text{ h}^{-1}$ , respectively. The photodegradation efficiency of gaseous benzene on Ag/Ti/Si (0.1/1/2) films under visible light irradiation could be increased up to 9 times when compared with alone  $\text{TiO}_2$  films. The antimicrobial activity of the Ag/ $\text{TiO}_2$ /MCM-41 nanocomposite film against *E. coli* was evaluated under visible light irradiation for 2 h. The percentage reduction of viable *E. coli* (%R) under visible light irradiation of Ag/Ti/Si (0.1/1/2) film was increased up to 98.2% due to the acceleration of Ag transformation to  $\text{Ag}^+$  by photocatalytic reaction. Thus, the Ag/ $\text{TiO}_2$ /MCM-41 nanocomposite film prepared in this study has been proved as a new promising smart film for indoor air treatment.

## 7.2 Recommendations

Recommendations for the further study can be made:

7.2.1 The kinetic reaction of gaseous benzene on the photocatalyst films in this study were plotted with the pseudo-first-order model. This model did not fit well at low benzene concentration, due to the fact that the photocatalytic reactivity of gaseous benzene on the nanocomposite films occurred simultaneously with the adsorption mechanism. Therefore, a more appropriate kinetic reaction model should be investigated.

7.2.2 Derivative products of benzene gas from the photocatalytic reactivity of films should be investigated in order to understand its photocatalytic degradation mechanism.

7.2.3 The photocatalyst films in this study were tested in a simulated indoor air system or on a lab scale. The applications for industrial scales should be further explored.

7.2.4 The treatment of other indoor air pollutants by the prepared nanocomposite films should be studied further.

## REFERENCES

- [1] Nischk, M., Mazierski, P., Gazda, M., Zalesk, A. (2014), "Ordered TiO<sub>2</sub> nanotubes: The effect of preparation parameters on the photocatalytic activity in air purification process", *Applied Catalysis B: Environmental*, **144**, pp. 674-85.
- [2] González, E.I.C., Riccò, R., Montorsi, M., Montorsi, M., Falcaro, P., Siligardi, C. (2014), "Self-cleaning glass prepared from a commercial TiO<sub>2</sub> nano-dispersion and its photocatalytic performance under common anthropogenic and atmospheric factors", *Building and Environment*, **71**, pp. 7-14.
- [3] Rtimi, S., Baghriche, O., Sanjines, R., Pulgarin, C., Bensimon, M., Kiwi, J. (2013), "TiON and TiON-Ag sputtered surfaces leading to bacterial inactivation under indoor actinic light", *Journal of Photochemistry and Photobiology A: Chemistry*, **256**, pp. 52-63.
- [4] Chen, J., Li, G., He, Z., An, T. (2011), "Adsorption and degradation of model volatile organic compounds by a combined titania–montmorillonite–silica photocatalyst", *Journal of Hazardous Materials*, **190**, pp. 416-423.
- [5] Thevenet, F., Guillard, C., Rousseau, A. (2014), "Acetylene photocatalytic oxidation using continuous flow reactor: Gas phase and adsorbed phase investigation, assessment of the photocatalyst deactivation", *Chemical Engineering Journal*, **244**, pp. 50-58.
- [6] United States Environmental Protection Agency (2013). "An introduction to indoor air quality (IAQ)". Available online: <http://www.epa.gov/iaq/ia-intro.html>.
- [7] Xiao, G., Huang, A., Su, H., Tan, T. (2013), "The activity of acrylic-silicon/nano-TiO<sub>2</sub> films for the visible-light degradation of formaldehyde and NO<sub>2</sub>", *Building and Environment*, **65**, pp. 215-221.

- [8] World Health Organization (2010), *WHO Guidelines for Indoor Air Quality: Selected Pollutants*, vol. 1. 15-54, Copenhagen.
- [9] United States Environmental Protection Agency (2006). "Benzene teach chemical summary". Available online: [http://www.epa.gov/teach/chem\\_summ/BENZ\\_summary.pdf](http://www.epa.gov/teach/chem_summ/BENZ_summary.pdf).
- [10] Sangrajang, S. (2008), "Toxicological review of benzene: cancer aspect", *Thai Cancer Journal*, **28**, pp. 93-100.
- [11] Klinmalee, A., Srimongkol, K., Oanh, N.T.K. (2009), "Indoor air pollution levels in public buildings in Thailand and exposure assessment", *Environmental Monitoring and Assessment*, **156**, pp. 581-594.
- [12] Pollution Control Department (2004), Air Quality and Noise Standards, Available online: [http://www.pcd.go.th/info\\_serv/en\\_reg\\_std\\_airsnd01.html](http://www.pcd.go.th/info_serv/en_reg_std_airsnd01.html).
- [13] The Better Air Company (2012), Industrial Odour Control, Available online: <http://www.betteraircompany.com/solutions/industrial-odour-control/>.
- [14] Chen, J., Poon, C.S. (2009), "Photocatalytic construction and building materials: From fundamentals to applications". *Building and Environment*, **44**, pp. 1899-1906.
- [15] Auvinen, J., Wirtanen, L. (2008), "The influence of photocatalytic interior paints on indoor air quality", *Atmospheric Environment*, **42**, pp. 4101-4112.
- [16] Ashkarran, A.A., Aghigh, S.M., Kavianipour, M., Farahani, N.J. (2011), "Visible light photo-and bioactivity of Ag/TiO<sub>2</sub> nanocomposite with various silver contents", *Current Applied Physics*, **11**, pp. 1048-1055.

- [17] Zhou, J., Cheng, Y., Yu, J. (2011), "Preparation and characterization of visible-light-driven plasmonic photocatalyst Ag/AgCl/TiO<sub>2</sub> nanocomposite thin films", *Journal of Photochemistry and Photobiology A: Chemistry*, **223**, pp. 82-87.
- [18] Peerakiathajohn, P., Onreabroy, W., Chawengkijwanich, C., Chiarakorn, S. (2011), "Preparation of visible-light-responsive TiO<sub>2</sub> doped Ag thin film on PET plastic for BTEX treatment", *Journal of Sustainable Energy & Environment*, **2**, pp. 121-125.
- [19] Mo, A., Liao, J., Xu, W., Xian, S., Li, Y., Bai, S. (2008), "Preparation and antibacterial effect of silver-hydroxyapatite/titania nanocomposite thin film on titanium", *Applied Surface Science*, **255**, 2, pp. 435-438.
- [20] Raffi, M., Hussain, F., Bhatti, T.M., Akhter, J.I., Hameed, A., Hasan, M.M. (2008), "Antibacterial characterization of silver nanoparticles against *E. coli* ATCC-15224", *Journal of Materials Science and Technology*, **24**, pp. 192-196.
- [21] Yu, B., Leung, K.M., Guo, Q., Lau, W.M., Yang, J. (2011), "Synthesis of Ag–TiO<sub>2</sub> composite nano thin film for antimicrobial application", *Nanotechnology*, **22**, pp. 1-9.
- [22] Zhao, W., Feng, L., Yang, R., Zheng, J., Li, X. (2011), "Synthesis, characterization, and photocatalytic properties of Ag modified hollow SiO<sub>2</sub>/TiO<sub>2</sub> hybrid microspheres", *Applied Catalysis B: Environmental*, **103**, pp. 181-189.
- [23] Hou, X.G., Huang, M.D., Wu, X.L., Liu, A.D. (2009), "Preparation and studies of photocatalytic silver-loaded TiO<sub>2</sub> films by hybrid sol-gel method", *Chemical Engineering Journal*, **146**, 1, pp. 42-48.

- [24] Lin, K., Pescarmona, P.P., Houthoofd, K., Liang, D., Tendeloo, G.V., Jacobs, P.A. (2009), "Direct room-temperature synthesis of methyl-functionalized Ti-MCM-41 nanoparticles and their catalytic performance in epoxidation", *Journal of Catalysis*, **263**, pp. 75-82.
- [25] Kolinko, P.A., Smirniotis, P.G., Kozlov, D.V., Vorontsov, A.V. (2012), "Direct room-temperature synthesis of methyl-functionalized Ti-MCM-41 nanoparticles and their catalytic performance in epoxidation", *Journal of Photochemistry and Photobiology A: Chemistry*, **232**, pp. 1-7.
- [26] Li, B., Liu, X., Meng, F., Chang, J., Ding, C. (2009), "Preparation and antibacterial properties of plasma sprayed nano-titania/silver coatings", *Materials Chemistry and Physics*, **118**, 1, pp. 99-104.
- [27] Zhang, P., Yin, S., Sato, T. (2009), "Synthesis of high-activity TiO<sub>2</sub> photocatalyst via environmentally friendly and novel microwave assisted hydrothermal process", *Applied Catalysis B: Environmental*, **89**, (1-2), pp. 118-122.
- [28] Chen, F., Liu, Z., Liu, Y., Fang, P., Dai, Y. (2013), "Enhanced adsorption and photocatalytic degradation of high-concentration methylene blue on Ag<sub>2</sub>O-modified TiO<sub>2</sub>-based nanosheet", *Chemical Engineering Journal*, **221**, pp. 283-291.
- [29] Suwarnkar, M.B., Dhabbe, R.S., Kadam, A.N., Garadkar, K.M. (2014), "Enhanced photocatalytic activity of Ag doped TiO<sub>2</sub> nanoparticles synthesized by a microwave assisted method", *Ceramics International*, **40**, pp. 5489-5496.
- [30] Yu, C., Wei, L., Li, X., Chen, J., Fan, Q., Yu, J.C. (2013), "Synthesis and characterization of Ag/TiO<sub>2</sub>-B nanosquares with high photocatalytic activity under visible light irradiation", *Materials Science and Engineering: B*, **178**, 6, pp. 344-348.

- [31] Chen, Q., Shi, W., Xu, Y., Wu, D., Sun, Y. (2011), "Visible-light-responsive Ag–Si codoped anatase TiO<sub>2</sub> photocatalyst with enhanced thermal stability", *Materials Chemistry and Physics*, **125**, pp. 825-832.
- [32] Yasushiro, S., Takayuki, H. (2008), "Selective organic transformations on titanium oxide-based photocatalysts", *Journal of photochemistry and Photobiology C: Photochemistry Reviews*, **9**, pp. 157-170.
- [33] Klankaw, P., Chawengkijwanich, C., Grisdanurak, N., Chiarakorn, S. (2012), "The hybrid photocatalyst of TiO<sub>2</sub>–SiO<sub>2</sub> thin film prepared from rice husk silica" *Superlattices and Microstructure*, **12**, 51, pp. 343-352.
- [34] Wang, S., Shi, Y., Ma, X. (2012), "Microwave synthesis, characterization and transesterification activities of Ti-MCM-41", *Microporous and Mesoporous Materials*, **156**, pp. 22-28.
- [35] Dunnill C.W., *et al.* (2011), "Nanoparticulate silver coated-titania thin films-Photo-oxidative destruction of stearic acid under different light sources and antimicrobial effects under hospital lighting conditions", *Journal of Photchemistry and Photobiology A: Chemistry*, **220**, pp. 113–123.
- [36] Guieysse, B., Hort, C., Platel, V., Munoz, R., Ondarts, M., Revah, S. (2008), "Biological treatment of indoor air for VOC removal: Potential and challenges", *Biotechnology Advances*, **26**, pp. 398-410.
- [37] Ongwandee, M. (2011), "Indoor air pollution: volatile organic compounds in non-industrial microenvironments in Thailand", *Journal of Environmental Research*, **34**, 2, pp. 1-19.
- [38] Sekulska, M.S., Pajak, A.P., Szyszka, A., Nowicki, M., Filipiak, M. (2007), "Microbiological Quality of Indoor Air in University Rooms", *Polish Journal of Environmental Studies*, **4**, pp. 623-632.

- [39] Chan, P.L., Yu, P.H.F., Cheng, Y.W., Chan, C.Y., Wong, P.K. (2009), "Comprehensive characterization of indoor airborne bacterial profile", *Journal of Environmental Sciences*, **21**, pp. 1148-1152.
- [40] Morse, R., Acker, D. (2009). "Indoor air quality and mold prevention of the building envelope", Whole Building Design Guild. Available online: [http://www.wbdg.org/resources/env\\_iaq.php](http://www.wbdg.org/resources/env_iaq.php).
- [41] European Concerted Action (1991), *Effects of Indoor Air Pollution on Human Health*. Commission of the European Communities, Luxembourg.
- [42] Zhong, L., Haghighat, F., Blondeau, P., Kozinski, J. (2010), "Modelling and Physical interpretation of photocatalytic oxidation efficiency in indoor air applications", *Building and Environment*, **45**, pp. 2689-2697.
- [43] Diebold, U. (2003), "The surface science of titanium dioxide", *Surface Science Reports*, **48**, pp. 53-229.
- [44] Hiram, D.C., Agrios, A.G., Gray, K.A., Rajh, T., Thurnauer, M.C. (2003), "Explaining the Enhanced Photocatalytic Activity of Degussa P25 Mixed-Phase TiO<sub>2</sub> Using EPR", *The Journal of Physical Chemistry B*, **107**, pp. 4545-4549.
- [45] Ismail, A.A., Bahnemann, D.W. (2012), "Pt colloidal accommodated into mesoporous TiO<sub>2</sub> films for photooxidation of acetaldehyde in gas phase", *Chemical Engineering Journal*, **203**, pp. 174-181.
- [46] Thomas, J., Yoon, M. (2012), "Facile synthesis of pure TiO<sub>2</sub>(B) nanofibers doped with gold nanoparticles and solar photocatalytic activities", *Applied Catalysis B: Environmental*, **111**, pp. 502-508.

- [47] Heciak, A., Morawski, A.W., Grzmil, B., Mozia, S. (2013), "Cu-modified TiO<sub>2</sub> photocatalysts for decomposition of acetic acid with simultaneous formation of C<sub>1</sub>–C<sub>3</sub> hydrocarbons and hydrogen", *Applied Catalysis B: Environmental*, **140-141**, pp. 108-114.
- [48] Jeyalakshmi, V., Mahalakshmy, R., Krishnamurthy, K.R., Viswanathan, B. (2012), "Titania based catalysts for photoreduction of carbon dioxide: Role of Modifiers", *Indian Journal of Chemistry*, **51**, pp. 1263-1283.
- [49] Chai, L.Y., Wei, S.W., Peng, B., Li, Z.Y. (2008), "Effect of thermal treating temperature on characteristics of silver-doped titania", *Transactions of Nonferrous Metals Society of China*, **18**, 4, pp. 980-985.
- [50] Jeyalakshmi, V., Mahalakshmy, R., Krishnamurthy, K.R., Viswanathan, B. (2012), "Titania based catalysts for photoreduction of carbon dioxide: Role of modifiers", *Indian Journal of Chemistry*, **51**, pp. 1263-1283.
- [51] Sung-Suh, H.M., Choi, J.R., Hah, H.J., Koo, S.M., Bae, Y.C. (2004), "Comparison of Ag deposition effects on the photocatalytic activity of nanoparticulate TiO<sub>2</sub> under visible and UV light irradiation", *Journal of Photochemistry and Photobiology A: Chemistry*, **163**, pp. 37-44.
- [52] Liu, Y., Wang, X., Yang, F., Yang, X. (2009), "Excellent antimicrobial properties of mesoporous anatase TiO<sub>2</sub> and Ag/TiO<sub>2</sub> composite films", *Microporous and Mesoporous Materials*, **114**, pp. 431-439.
- [53] Montgomery, S., Kenney, D., Dowd, N.O. (2010), PVD and CVD coatings for the metal forming industry, paper presented in the, *Mechanical Engineering Commons*, pp. 1-13. MATRIB 2010, Croatia.
- [54] Deyanira, A.B., Guillermo, N.S., Leticia, L.R., Martín, A.I.A., Francisco, J.C. (2008), "Titanium-modified MCM-41 prepared by ultrasound and by hydrothermal



- treatment, catalysts for acetylation reactions”, *Journal of the Mexican Chemical Society*, **52**, pp. 175-180.
- [55] Kiraz, N., Esin, B., Ömer, K., Hasan, E.C., Meltem, A., Zerin, Y., Ertuğrul, A. (2011), “Preparation of Sn doped nanometric TiO<sub>2</sub> powders by reflux and hydrothermal syntheses and their characterization”, *Journal of Sol-Gel Science and Technology*, **59**, pp. 381-386.
- [56] Gaur, A.M., Joshi, R., Kumar, M. (2011), “Deposition of Doped TiO<sub>2</sub> Thin Film by Sol Gel Technique and its Characterization”, paper presented in the, *Proceedings of the World Congress on Engineering*, WCE 2011, London.
- [57] Froschl, T., *et al.* (2012), “High surface area crystalline titanium dioxide: potential and limits in electrochemical energy storage and catalysis”, *Chemical Society Reviews*, **41**, pp. 5313–5360.
- [58] Miki, I., Akira, N., Kai, K., Naoya, E., Junichi, H. (2008), “Microwave-assisted sol–gel process for production of spherical mesoporous silica materials”, *Journal of Material Science*, **43**, pp. 2362–2366.
- [59] Kresge, C.T., *et al.* (1992), “Ordered mesoporous molecular sieves synthesized by a liquid-crystal template mechanism”, *Letters to Nature*, **359**, pp. 710-712.
- [60] Shen, J.L., Lee, Y.C., Lui, Y.L., Cheng, P.W., Cheng, C.F. (2003), “Blue-green photoluminescence in MCM-41 mesoporous nanotubes”, *Journal of Physics: Condensed Matter*, **15**, pp. 297-304.
- [61] Areerob, T. (2006), “Surface modification of RH-MCM-41 by silylation t for volatile organic compounds adsorption”, Thesis for Master Degree in Environmental Technology, Master of Science, King Mongkut's University of Technology Thonburi.

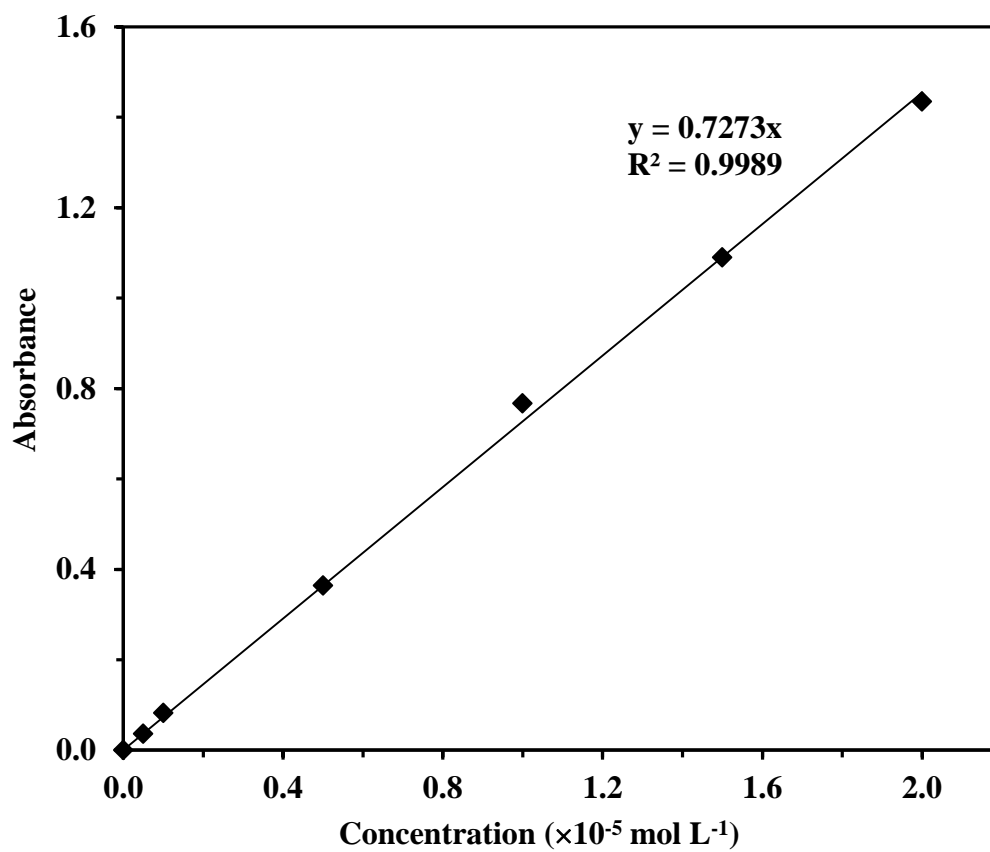
- [62] Chiarakorn, S. (2003), "Utilization of rice husk silica for synthesis of mesoporous molecular sieve MCM-41 applied for catalytic hydrodechlorination of chlorinated volatile organic compounds" Environmental Management Doctor of Philosophy Chulalongkorn University.
- [63] Storck, S., Bretinger, H., Maier, W.F. (1998), "Characterization of micro- and mesoporous solids by physisorption methods and pore-size analysis", *Applied Catalysis A: General*, **174**, 1-2, pp. 137-146.
- [64] Wang, W., Liu, P., Zhang, M., J. Hu, Xing, F. (2012), "The pore structure of phosphoaluminate cement", *Open Journal of Composite Materials*, **2**, pp. 104-112.
- [65] Machida, M., Norimoto, K., Watanabe, T. (1999), "The effect of SiO<sub>2</sub> addition in super-hydrophilic property of TiO<sub>2</sub> photocatalyst", *Journal of Materials Science*, **34**, pp. 2569–2574.
- [66] Yuan, Y. and Lee, T.R., Bracco, G., Holst, B. (2013), *Contact angle and wetting properties*, 51, pp. 3-34. Surface Science Techniques (Eds.), Springer Series in Surface Sciences.
- [67] Hou, Y. D., *et al.* (2008), "N-doped SiO<sub>2</sub>/TiO<sub>2</sub> mesoporous nanoparticles with enhanced photocatalytic activity under visible-light irradiation", *Chemosphere*, **72**, 3, pp. 414-421.
- [68] Japanese Industrial Standard (2001), *JIS Z 2801:2000 Antimicrobial products-Test for antimicrobial activity and efficacy*, Japanese Standards Association, Tokyo.
- [69] Xue, B., *et al.* (2013), "Acid–base properties of TiO<sub>2</sub>-modified MCM-41 mesoporous silica and its catalytic performance for ortho-selective ethylation of phenol with diethyl carbonate", *Journal of Molecular Catalysis A Chemical*, **357**, pp. 50-58.

- [70] Artkla, S., Wantala, K., Srinameb, B., Grisdanurak, N., Klysubun, W., Wittayakun, J.(2009), “Characteristics and photocatalytic degradation of methyl orange on Ti-RH-MCM-41 and TiO<sub>2</sub>/RH-MCM-41”, *Korean Journal of Chemical Engineering*, **26**, pp. 1556-1562.
- [71] Shi, Y., Wang, S., Ma, X. (2011), “Microwave preparation of Ti-containing mesoporous materials. Application as catalysts for transesterification”, *Chemical Engineering Journal*, **166**, pp. 744-750.
- [72] Kiel, S., Grinberg, O., Perkas, N., Charmet, J., Kepner, H., Gedanken, A. (2012), “Forming nanoparticles of water-soluble ionic molecules and embedding them into polymer and glass substrates”, *The Beilstein Journal of Nanotechnology*, **3**, pp. 267-276.
- [73] Braconnier, B., Paez, C.A., Lambert, S., Alie, C., Henrist, C., Poelman, D. (2009), “Ag- and SiO<sub>2</sub>-doped porous TiO<sub>2</sub> with enhanced thermal stability”, *Microporous and Mesoporous Materials*, **122**, 1-3, pp. 247-254.
- [74] Chen, Y.F., Lee, C.Y., Yeng, M.Y., Chiu, H.T. (2003), “The effect of calcination temperature on the crystallinity of TiO<sub>2</sub> nanopowders”, *Journal of Crystal Growth*, **247**, pp. 363-370.
- [75] Viana, M.M., Mohallem, N.D.S., Miquita, D.R., Balzuweit, K., Pinto, E.S. (2013), “Preparation of amorphous and crystalline Ag/TiO<sub>2</sub> nanocomposite thin films”, *Applied Surface Science*, **265**, pp. 130-136.
- [76] Bianchi, C.L., Gatto, S., Pirola, C., Naldoni, A., Michele, A.D., Cerrato, G. (2014), “Photocatalytic degradation of acetone, acetaldehyde and toluene in gas-phase: Comparison between nano and micro-sized TiO<sub>2</sub>”, *Applied Catalysis B: Environmental*, **146**, pp. 123–30.

- [77] Balachandran, K., Vnckatesh, R., Sivaraj, R. (2010), "Synthesis of nano  $\text{TiO}_2\text{-SiO}_2$  composite using sol-gel method: effect on size, surface morphology and thermal stability", *International Journal of Engineering Science and Technology*, **2**, 8, pp. 3695-3700.
- [78] Xing, M., Zhang, J., Chen, F. (2009), "Effect of chromium migration from metallic supports on the activity of diesel exhaust catalysts", *Applied Catalysis B: Environmental*, **89**, pp. 563-569.
- [79] Houas, A., Lachheb, H., Ksibi, M., Elaloui, E., Guillard, C., Herrmann, J.M., (2001), "Photocatalytic degradation pathway of methylene blue in water", *Applied Catalysis B: Environmental*, **31**, pp. 145-157.
- [80] Hennezel, O., Pichat, P., Ollis, D.F. (1998), "Benzene and toluene gas-phase photocatalytic degradation over  $\text{H}_2\text{O}$  and  $\text{HCl}$  pretreated  $\text{TiO}_2$ : by-products and mechanisms", *Journal of Photochemistry and Photobiology A: Chemistry*, **118**, pp. 197-204.
- [81] Mcevoy, J.G., Zhang, Z. (2014), "Antimicrobial and photocatalytic disinfection mechanisms in silver-modified photocatalysts under dark and light conditions", *Journal of Photochemistry and Photobiology C: Photochemistry Reviews*, **19**, pp. 62-75.

## **APPENDIXES**

**APPENDIX A**  
**CALIBRATION CURVE OF METHYLENE BLUE DYE**



**Figure A-1** Linear calibration curve of methylene blue dye.

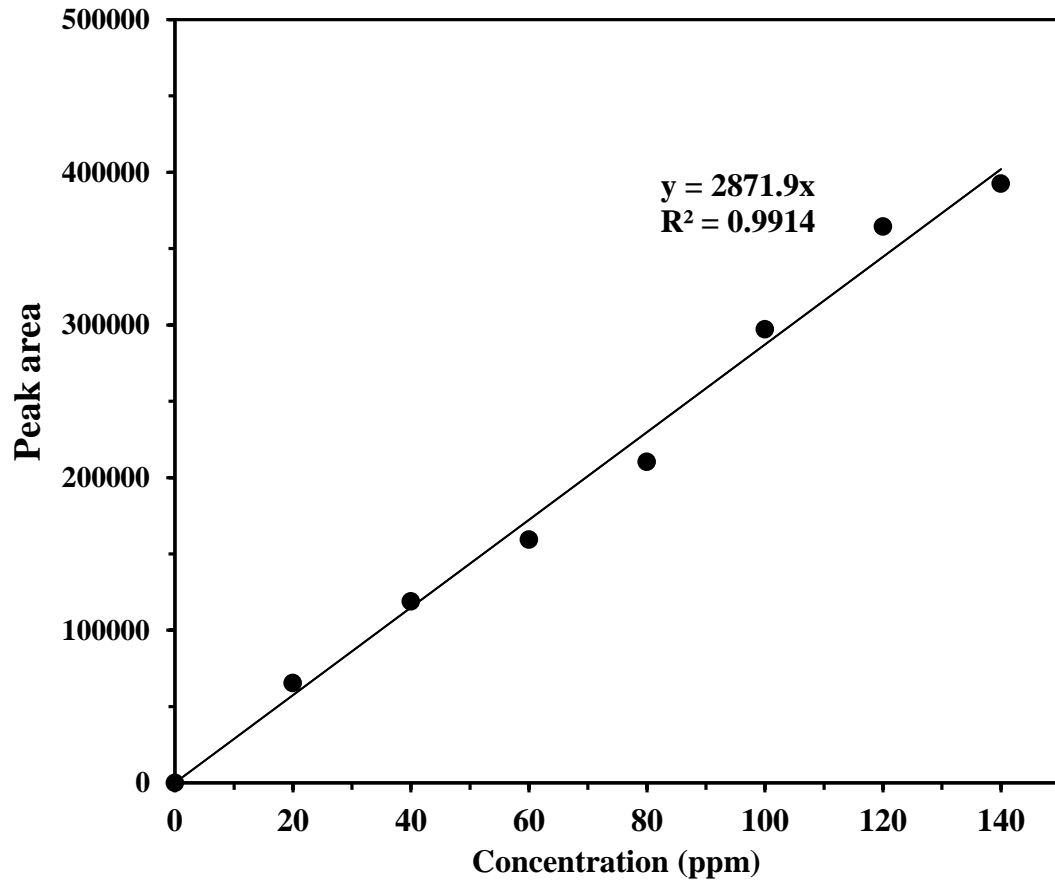
## APPENDIX B

### CONTACT ANGLE MEASUREMENT

**Table B-1** Summary of the contact angle measurement on TiO<sub>2</sub>, Ag/Ti/Si (0.1/1/0) and Ag/Ti/Si (0.1/1/2) photocatalyst films.

Time (s)	Contact angle (°)		
	TiO <sub>2</sub>	Ag/Ti/Si (0.1/1/0)	Ag/Ti/Si (0.1/1/2)
0	28	26	21
10	27	20	14
20	26	19	4
30	25	18	0
40	25	17	0
50	24	16	0
60	23	15	0

**APPENDIX C**  
**CALIBRATION CURVE OF BENZENE**



**Figure C-1** Linear calibration curve of gaseous benzene.



## BIOGRAPHY

Name	Miss Waraporn Tongon
Date of Birth	December 11, 1983
Education Record	
High School	Islamic College of Thailand, 2000
Bachelor's Degree	Bachelor of Science, Chemistry Science, King Mongkut's University of Technology Thonburi, 2004
Master's Degree	Master of Science (Environmental Technology), School of Energy, Environment and Materials, King Mongkut's University of Technology Thonburi, 2008
Research Grants	<ul style="list-style-type: none"> <li>- The Petchra Pra Jom Klao Scholarship of King Mongkut's University of Technology Thonburi (KMUTT), Thailand.</li> <li>- Thailand Graduate Institute of Science and Technology Scholarship (TGIST) from the National Science and Technology Development Agency (NSTDA), Thailand (Scholarship No. TGIST 01-53-019)</li> </ul>
International Conference	<ul style="list-style-type: none"> <li>- AMN-5: Fifth International Conference on Advanced Materials and Nanotechnology, 7-11 February 2011, Wellington, New Zealand.</li> </ul>
Publication	<ul style="list-style-type: none"> <li>- W. Tongon, C. Chawengkijwanich and S. Chiarakorn (2014), "Visible light responsive Ag/TiO<sub>2</sub>/MCM-41 nanocomposite films synthesized by a microwave assisted sol-gel technique", Superlattices and Microstructures, Vol. 69, pp. 108-121.</li> </ul>